Design and Implementation of a Superconducting Phase-Shifter

N.E. Beschoor Plug

Master of Science Thesis

Delft University of Technology

Telecommunications & Sensing Systems

Design and Implementation of a Superconducting Phase-Shifter

Master of Science Thesis

For the degree of Master of Science in Telecommunications & Sensing Systems at Delft University of Technology.

To be defended on Friday May 7, 2021 at 01:00 PM.

Thesis committee:
Prof. dr. ir. J. J. A. Baselmans, TU Delft, supervisor
A. Pascual Laguna, TU Delft, daily supervisor
Prof. dr. C. Vaucher, TU Delft

N.E. Beschoor Plug
April 29, 2021

Faculty of Electrical Engineering, Mathematics and Computer Science · Delft University of Technology

TUDelft
Delft
University of
Technology

Abstract

Superconducting detectors such as Microwave Kinetic Inductance Detectors (MKIDs) have lead to the designs of THz on-chip spectrometers such as DESHIMA. With DESHIMA a wideband THz signal is fully sampled by several hundreds of channels of which the frequency is defined by an array of band-pass filters. Each band-pass filter which is connected to a separate MKID which can be read-out simultaneously by a microwave read-out signal. This single-pixel system can be expanded through the implementation of steerable antennas. Especially when several spectrometers are used to create a multi-pixel spectrometer, the process of measuring the Universe's background radiation could be sped up and also be used to calibrate the instrument.

In this thesis an on-chip platform is designed which is able to quantify the achievable phase-shifting capabilities of a superconducting microstrip line at terahertz frequencies. This is done by exploiting the non-linear behavior of a superconductor's kinetic inductance to a dc current. DC-biased superconducting Fabry-Pérot (FP) resonators, replacing the role of the filter-bank mentioned above, have been investigated and designed to quantify the phase-shifting capabilities by probing the shift in the resonance frequency. The injection/extraction of DC biasing currents on the Fabry-Pérot resonator need to be transparent to the THz frequencies. To do so, low-pass stepped-impedance filters have been designed.

A Chebyshev filter has been implemented with a stepped-impedance filter which has a minimal rejection of 45 dB between 300 and 400 GHz. This is necessary to prevent leakage of the THz signal into the bias feeds. The two filters reactively load the FP and have an effect on the Q-factors. This change, without any bias current applied, is small enough to be neglected. The tuning of the FP with a dc bias current is limited by the critical current the superconductor can support. This is determined by the geometry and material characteristics of the superconductor. The sensitivity of the superconductor to a dc current is limited by its kinetic sheet inductance. The larger this value is, the larger the tuning range. The results of the simulations shown that with this design it is possible to obtain a phase shift of roughly 0.7% which coincides with phase shift values found in other studies. It is therefore possible to implement this design to create beam-steerable superconducting antennas. The design is being fabricated as this is written and will be measured in the coming months.

Acknowledgements

Many people have helped me in different ways during my thesis and I would like to acknowledge some in particular.

First and foremost my daily supervisor Alejandro. Even though I sometimes got lost in the world of superconductivity you always kept me on the right track. Even in this crazy year of working from home you have always been available for help. You have been very patient with me, even if you had to repeat your explanations more than once. Your scrutiny of my work and thesis have significantly contributed to what it is now.

Then of course Jochem. You completely surprised me when you asked me if I was interested in doing my thesis with your group. From the moment you asked I was extremely excited about it. Thank you for this opportunity! I've learned a lot from you along the way and am happy to have contributed to your research goals.

I would also like to thank Kevin Kouwenhoven, Sebastian Hänle, Kenichi Karatsu and David Thoen for supplying me with data, models and pictures and in general always answering my steady flow of questions.

Last but not least I want to thank two others: my fiancé and my mother. Vincent thank you for being my debug-duck. Be it for Matlab, Python or writer's block. Sometimes just walking up to you was enough for me to realize what I had to do. To my mother, credit is due where credit is due. Your notes and edits have shown me that you are as home in English-French judicial translation as you are in electrical engineering jargon.

Thank you all!

Nina Beschoor Plug
28 April, 2021

Table of Contents

Chapter 1

Introduction

The study of the Universe is fueled by information from the background radiation. Countless processes and phenomena occur within the Universe, each emitting signals at different frequencies and together forming the background radiation. For a full understanding of the Universe, it is therefore imperative to measure the background radiation at all frequencies. An example using the Andromeda galaxy is shown in Figure 1-1. Each image is created from data measured between radio frequencies (< 100 GHz) to x-ray (between roughly 10^8 and 10^{12} GHz). These snapshots give insight into chemical compositions, redshifts, and many more events.

Since each process can be identified from a specific frequency range, the background radiation can be subdivided into groups based on the source. The three largest sources are shown in Figure 1-2. They are the Cosmic Microwave Background (CMB), Cosmic Infrared Background (CIB) and Cosmic Optical Background (COB). The CMB is the radiation remnant from the Big Bang and is the brightest of the three. Half of the remaining radiation originates from stars and other processes which emit radiation in the visible frequency range (COB), the other half emanates from dust clouds heated by stars (CIB). These dust clouds absorb the radiation from stars and re-emit it at frequencies within the terahertz (THz), or sub-millimeter (submm), band. The widest definition for this band is $0.1 - 10$ THz, with corresponding wavelengths of $\lambda = 30$ μm to 3 mm [1].

The THz band has only recently been studied and has already shown to be extremely informative. In this band, it is possible to localize and identify galaxies shielded by dust clouds which are invisible when using optical surveys. These dust-engulfed galaxies reveal information on the formation of stars from the interstellar medium (ISM) which gives insight into the evolution of galaxies. Stars form from dense dust clouds which absorb the radiation from the newly forming stars and re-emit this radiation in the THz range. Another virtue of the ability to observe this frequency range is the measurement and identification of atomic and molecular emission lines. These lines give information on the composition of the dust clouds. Since each atom and molecule emit at very specific frequencies, any shift of these emission lines can be used to calculate the redshift of the galaxy. THz observations have been especially good at locating luminous high-redshift galaxies which give great insights into the early Universe [2] [3].

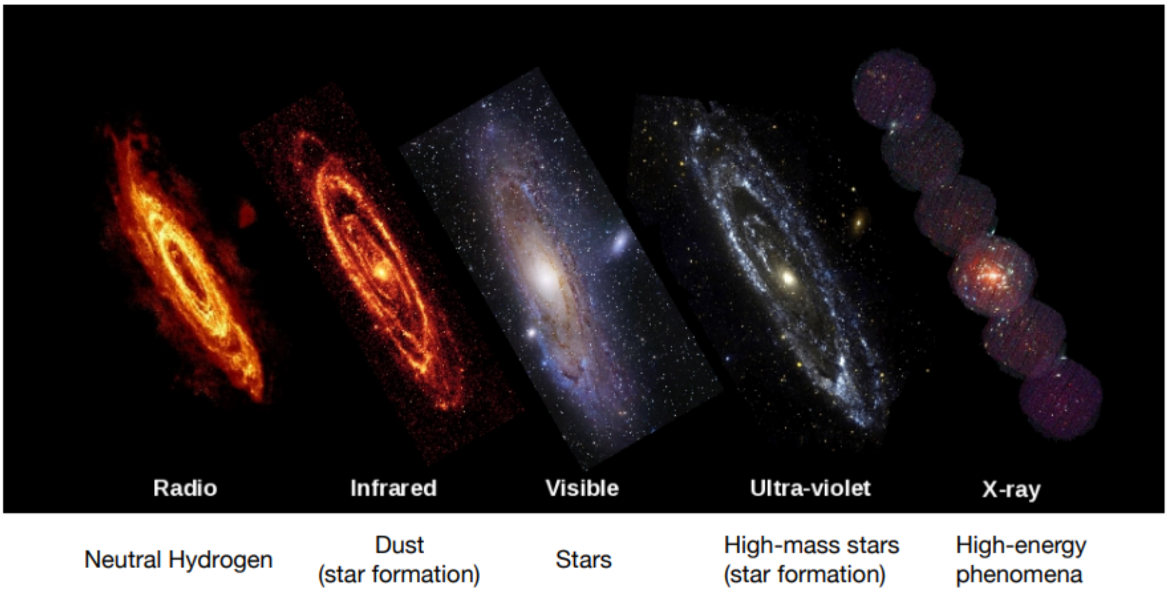

Figure 1-1: The Andromeda galaxy observed at different frequencies demonstrates the importance of observing at different frequencies [1].

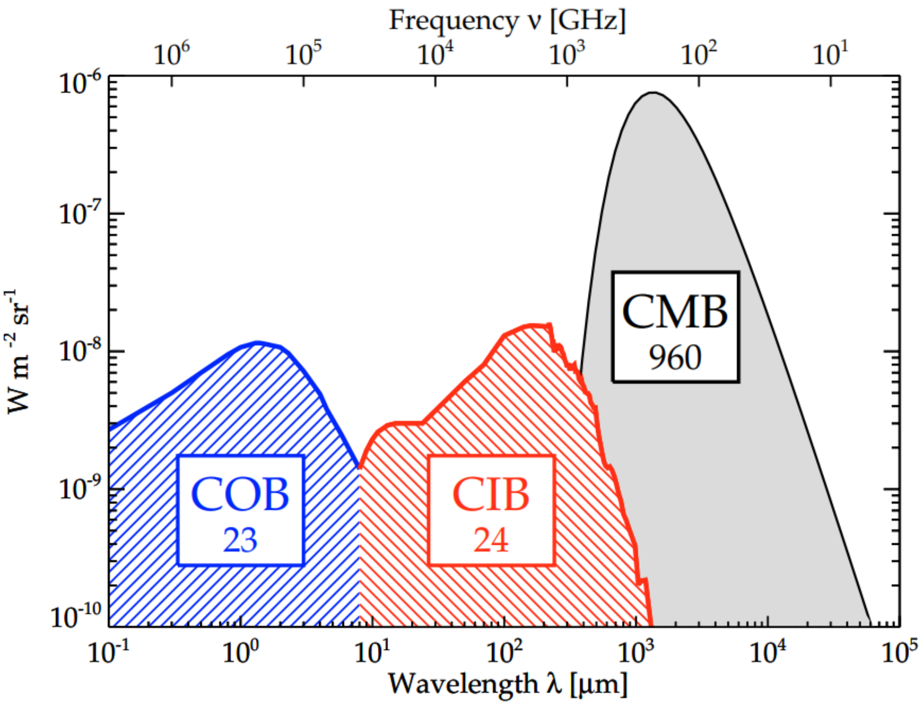

Figure 1-2: Radiation power in the universe. The CMB contains by far the largest amount of power but can be neglected due to nearly isotropic distribution. Apart form that, most of the radiated power emanates from stars (COB) and heated dust (CIB) [3].

1-1 THz astronomical instrumentation

The THz band is sandwiched between the frequency range which can be measured resorting to the combination of microwave and optical techniques. It is extremely difficult to read-out THz frequencies with electronics and, while wide Field-of-View (FoV) cameras can be used in this range, they are unable to perform blind spectral surveys which are crucial in this band. It is through blind spectral surveys that sources whose continuum radiation is too low to be measured can be located. The most viable option is therefore the design of multi-pixel THz spectrometers. The design of THz spectrometers has been boosted by the creation of superconducting detectors such as Microwave Kinetic Inductance Detectors (MKID) [4]. These are very advantageous to use due to their extreme sensitivity and the fact that their output can be multiplexed and read-out at microwave frequencies.

THz spectrometers can divided into two categories, namely Multi-Object Spectrometers (MOS) and Integral Field Units (IFU). The difference between the two is the sampling of the FoV: IFUs implement a dense sampling of the FoV while MOSs have a sparse FoV. The benefit of MOSs however is that they have steerable pixels. To be able to explore the THz sky fast and effectively, broadband MOSs with steerable pixels are key. Their design requires two things. The first is a broadband on-chip spectrometer such as DESHIMA [5], SuperSpec [6], CAMELS [7] and μSpec [8]. The second is a steerable broadband antenna such as the connected array of [9]. These superconducting phased array antennas rely on electronically superconducting phase shifters.

1-2 Problem statement

In DESHIMA the wideband (measured) signal is fully sampled by 350 channels as shown in Figure 1-3. The frequency of each channel is defined by the band-pass filters in the filter-bank. Each filter is connected to a separate MKID which are all read-out simultaneously by a microwave read-out signal. To speed up the process, instead of a single-pixel spectrometer, multi-pixel steerable antennas could be used to rapidly scan the sky and calibrate the instrument.

In [10] a Fabry-Pérot resonator was implemented between the antenna and an MKID to characterize the losses of dielectric materials. The resonator only transmits a signal if it is an integer multiple of its resonant frequency f_0 and therefore defines the input signal of the MKID. If the resonant frequency can be shifted, the input signal of the MKID is shifted and can effectively scan a wideband signal. This is demonstrated in Figure 1-4 where the output of an un-biased and biased Fabry-Pérot resonator is given. Without any biasing, for this particular geometry the resonance peak is located at f_0. After a certain level of biasing is applied, the resonance peak has shifted by δf, scanning all frequencies in between.

An inherent property of superconductors is their kinetic inductance. The kinetic inductance varies non-linearly with the magnetic field and the current. By biasing a superconducting resonator its response can be shifted in frequency. The aim of this thesis is to provide an on-chip platform to quantify the achievable phase-shifting capabilities at terahertz frequencies by exploiting the kinetic inductance variation. This will be designed for the Fabry-Pérot resonator as a proof of concept. The system has the following requirements:

1. The shift in resonant frequency should be more than the Full Width Half Magnitude (FWHM) bandwidth of the unbiased peaks.

2. The biasing system cannot alter the shape of the peaks and their original location (f_0) by more than 10%.

3. The frequency range in which it must be able to scan is 300 - 400 GHz.

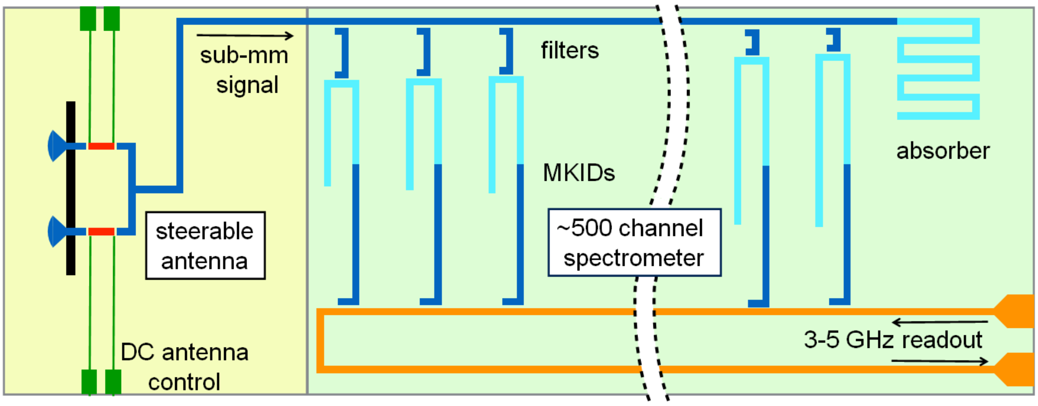

Figure 1-3: Schematic of a superconducting spectrometer with steerable antennas. There are about 500 filters, each connected to an MKID, which constitute the filter-bank. Each filter is called a channel. The MKIDs are read-out by a microwave signal.

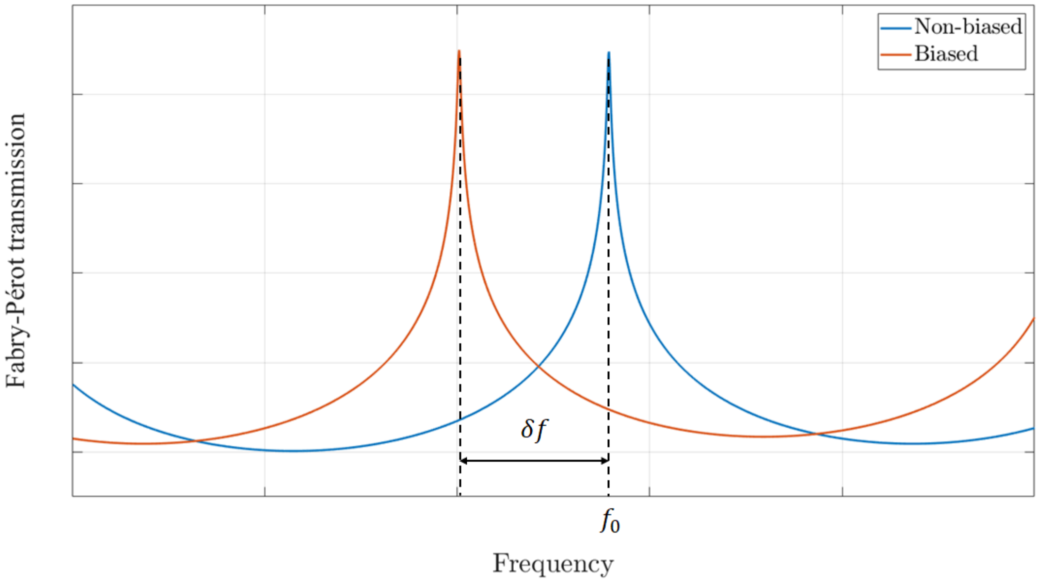

Figure 1-4: Example output of a Fabry-Pérot resonator and the desired shift in frequency δf from the original resonant frequency f_0 after biasing.

1-3 Proposed solution

The nonlinear dependence of the kinetic inductance of a superconductor on a bias current or magnetic field is exploited in a variety of applications such as parametric amplifiers, quantum electrodynamics and astronomical detectors. The approaches for biasing with a current or a magnetic field are very different and are optimized for different applications. A literature study was carried out to find the advantages and disadvantages of both methods. The results are summarized below, after which the proposed solution for this project will be selected.

1-3-1 DC current bias

When a dc current to regulate the kinetic inductance of a superconducting strip some sort of low-pass filter is necessary to merge and separate the bias signal from the actual signal. From the solutions found, two main distinctions could be made: the application to a superconducting slow traveling wave structure [11] [12] [13] and to a superconducting resonator [14] [15] [16] [17] [18].

For slow traveling wave structures the emphasis is on controlling the phase velocity of the signal through the kinetic inductance. Depending on the transmission line structure, material and bias current, values the change in phase, which is analogous to a shift in frequency, has been found to vary between 0.7% [11] to 4% [12] and even 6.7% [13].

In the case of the superconducting resonators, a shift in resonant frequency or the creation of ideal conditions for quantum measurements without affecting the resonator modes are often the objectives. The three studies which looked at the tuning of the resonant frequency demonstrated shifts of 4% [14] to 6.8% [17]. In the case of [18] a shift of 44% was predicted, this experiment was not yet measured though. The performance of resonators depends of the quality factor of their resonant peaks. When applying a bias current to the resonator, this should not effect the shape of the peaks. In [15] [16] the effect of two different low-pass filters on the FWHM of the resonance shape was found to be less than 1%. They also found that the location of the filters on the resonator can be optimized to enhance the rejection of the filter. This happens when the filters are placed on voltage nodes of the resonator standing wave pattern.

In all studies, lumped-element or distributed-element implementations of low-pass or band-pass filters were used to separate the signal paths. None of these studies, however, were conducted in the frequency range of this project, but a factor 10 to 100 times lower, which affects the choice of the filter. Creating a low pass filter to inject current is a relatively simple design to fabricate which only slightly changes the resonator structure. A drawback of this extra circuitry, however, is that it can introduce a large insertion loss for the dc current or form a leakage for the THz signal.

1-3-2 Magnetic field bias

The second method of tuning the kinetic inductance is through the application of a magnetic field. The effect of a magnetic field on the resonant frequency is significantly smaller than that of a current. In [19] the resonant frequency shifted by less than 1% for a coplanar waveguide

(CPW) resonator. For a microstrip resonator this is even smaller since CPWs focus the magnetic flux between the conductors. In an attempt to increase the effect of the magnetic field on the tuning factor, [20] and in [21] created a folded resonator in fractal patterns to trap the flux. This lead to a slightly increased frequency shift of 2.5%. This also changes the resonator geometry which is undesirable for this project.

A major advantage of using an external magnetic field is that the resonator structure does not need to be changed at all and that the Q-factor of the resonator can therefore remain high. There is, however, also a major drawback, namely that the effect of the tuning is not limited to the resonator. Since it is generated outside the cryostat there is no straightforward way to focus it only on the resonator. Therefore the whole system will be affected by the magnetic field, meaning that the MKID and signal lines will be detuned.

1-3-3 Proposed solution

From this brief study it can be concluded that the design of a current bias system is the preferable method of the two. Largest frequency shifts can be obtained and the effect of the current is limited to the resonator only. Therefore, a low-pass filter must be designed which only injects and extracts the dc current while having a minimal leakage of the THz signal. For this, different filter implementations and filter functions must be studied. Learning from the conclusions of [15] and [16] the location of the filter on the resonator must also be optimized.

1-4 Thesis outline

This thesis is structured in such a way as to guide the reader through the design process of the frequency tunable Fabry-Pérot resonators. This is done in three chapters which explain the theory, the design process and the final design which will be fabricated.

In chapter 2 the theory necessary for the comprehension of this work is explained. It is subdivided into a section on superconductivity, current biasing, resonators and low-pass filters. The section on superconductivity lays the foundation from which the effect of a biasing current and the operation of the frequency-tunable Fabry-Pérot and MKIDs can be explained. This introduces the concept of complex conductivity which is essential for most calculations performed in this thesis. The effects of a bias current are first explained through those of a magnetic field. The effect of a current and a magnetic field are analogous and some effects are easier to explain using a magnetic field. The kinetic inductance and secondary effects are derived from this. Microstrip resonators are treated next. Their frequency behavior and quality factors are first explained for a regular resonator and after the effects of the current are tied into the equations. The role of the Fabry-Pérot and MKID resonators are discussed as well. The section ends with a derivation of the behavior of stepped-impedance low-pass filters and two filter functions which can be implemented with it.

In chapter 3 the calculations necessary to design the Fabry-Pérot resonator and low-pass filter are worked-out. The design choice for the Fabry-Pérot and the low-pass filter are justified with simulations from Sonnet. After their designs are completed, the entire system is simulated together and the effect of the current is shown. The material properties and resonator architectures used in this section are not the final ones. They are used though since it gives the chance to compare the behavior of the filter and the effect of the current under different circumstances for the conclusion.

During the design process several significant changes were made. In chapter 4 the need for these changes is justified and their effects studied. The new design values are given, not calculated. This section also gives a discussion about the measurement objectives and fabrication details.

This thesis ends with a conclusion on the effectiveness of the design and gives an outlook on future work. This includes possible design improvements and a discussion on other possible areas of application.

Chapter 2

Theory

In this chapter the key concepts on which superconducting phase shifters are based are explained. These are used to justify the design of the Fabry-Pérot (FP) based prototype. The first important topic to cover is superconductivity, section 2-1. The behavior of superconductors can be described by two charge carriers. After defining the limits in which the superconductor operates, the complex conductivity will be explored. With the complex conductivity the effect of a current on a superconducting strip can be studied, section 2-2. There are limits to the application of a bias current in a superconductor. These will be derived from well-known effects of superconductivity. In section 2-3 the Fabry-Pérot resonator, implemented using a microstrip, is studied. Several characteristics of a microwave resonator, such as it's resonant frequency and the phase velocity will be defined in terms of bias current. The design of a microstrip resonator is explained using a set of parameters called the quality factors. Finally, in section 2-4 the design and synthesis of a low-pass stepped-impedance filter are explored. This is what will eventually inject the bias current into the microstrip resonator while not disturbing the resonator behavior.

2-1 Superconductivity

Atoms in a metal interact through metallic bonding. To envision this, the metal can be thought of as a lattice of positively charged ions which share a cloud of electrons as depicted in the left panel of Figure 2-1. Within this cloud electrons are allowed to move freely, allowing for the conduction of electric current. The measure of how freely the electrons can move is called conductivity σ; its inverse is defined as the resistivity ρ. As the temperature of the metal decreases, the lattice vibrations decrease, thereby increasing the mean free path l between electron scattering events and decreasing ρ [22]. At very low temperatures and for non-superconducting metals ρ becomes constant at a certain non-zero value, being limited by metal impurities. For superconductors on the other hand, the resistivity suddenly drops to zero when the temperature drops below the critical temperature T_c. This phenomenon was first observed in 1911 by Heike Kamerling Onnes when he studied the low temperature resistivity of Mercury.

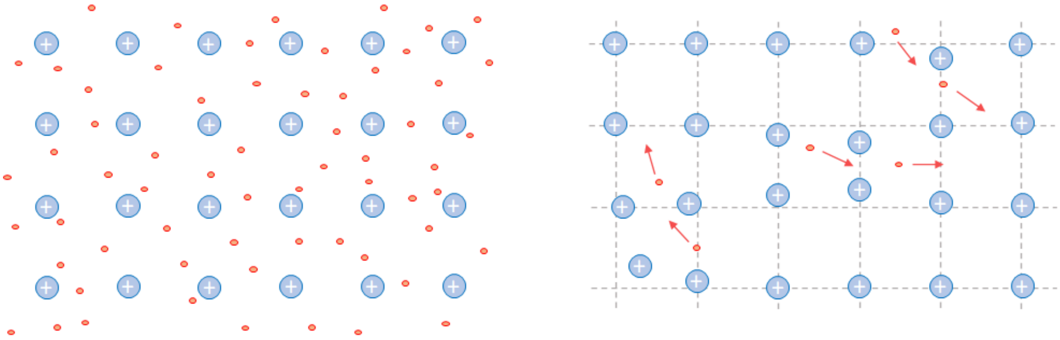

Figure 2-1: Left panel: Lattice interaction within a metal in the normal state. The positively charged ions form a lattice through which a cloud of electrons moves freely. Right panel: Example of Cooper pairs. Below T_c, when an electron moves through the lattice it leaves a positively charged area behind attracting another electron. This image has less electrons drawn in to emphasize the motion of the ions and therefore attraction of a second electron.

2-1-1 Cooper pairs and quasiparticles

For a very long time, the sudden vanishing of the resistivity at very low temperatures could not be explained. It wasn't until 1956, when L.N. Cooper [23] postulated the existence of Cooper pairs and together with J. Bardeen and J. R. Schrieffer [24] formed the microscopic theory of superconductivity (BCS theory), that this phenomenon could be explained. A Cooper pair is a pair of electrons of equal and opposite momentum and opposite spin. Even though the force between electrons is always repulsive, the Coulomb force, the net force between electrons can become attractive when the metal is in a superconducting state due to interactions between the electrons and the lattice. This is depicted in the right panel of Figure 2-1. As an electron moves through the lattice the positively charged ions are attracted to it. Due to the extremely low temperatures and their larger mass, the ions move slower than the electrons, leaving a space of higher positive charge and attracting a second electron. The conduction of these Cooper pairs is lossless which is why the resistivity vanishes. The minimum distance between the two electrons constituting a Cooper pair, also defined as the size of the pair, is called the intrinsic coherence length and is given by

$$\xi_0 = \frac{\hbar v_F}{\pi \Delta_0}, \tag{2-1}$$

where $\hbar$ is the modified Planck constant, v_F the Fermi velocity, which depends on the number of Cooper pairs and the volume of the metal, and Δ_0 the energy gap at $T = 0$ K [25]. The electrons which make up the pair switch constantly. At the onset of the superconducting state, only electrons with low kinetic energies can form Cooper pairs [22]. The other unpaired electrons, referred to as quasiparticles, will drop in number as the temperature decreases further according to the following expression [25]

$$n_{qp} \approx 2N_0\sqrt{2\pi k_B T \Delta}\exp\left(-\frac{\Delta}{k_B T}\right) \qquad \text{for } k_B T \ll \Delta, \tag{2-2}$$

where n_{qp} is the quasiparticle density per unit volume, N_0 the single spin density of states at the Fermi level, k_B the Boltzmann constant and T the temperature [25]. The formation of

Cooper pairs, and therefore reduction of quasiparticles, leads to an energy gap Δ. This gap is also known as the binding energy of a Cooper pair and in the BCS theory [24] it is defined as

$$\Delta \approx 1.76 k_B T_c \qquad T << T_c \tag{2-3}$$

$$\Delta \approx 3.2 k_B T_c \sqrt{1 - \left(\frac{T}{T_c}\right)} \qquad T \approx T_c. \tag{2-4}$$

Cooper pairs can be broken in two ways. The first is by thermal excitation. The second, shown in Figure 2-2, occurs when radiation of $\hbar\omega > 2\Delta$ is absorbed. In both cases the electrons in a Cooper pair obtain enough energy to overcome Δ and they become quasiparticles.

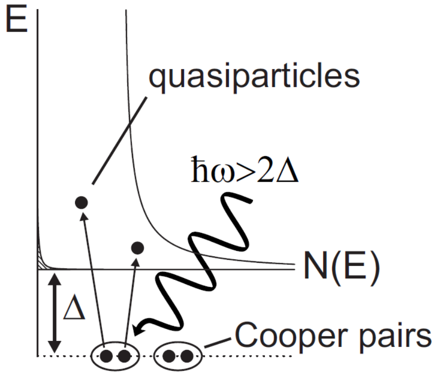

Figure 2-2: Cooper pairs are located at the Fermi energy (at the bottom of the graph). The formation of the Cooper pairs creates an energy gap Δ. The quasiparticles are located above the energy gap and are distributed according to Equation 2-2. Only particles with energies higher than 2Δ can break a Cooper pair, creating two quasiparticles. Image taken from [26].

2-1-2 Electrodynamic response

For any superconductor there are three important length scales: the electron mean free path l, the coherence length ξ and the magnetic penetration depth λ [25]. These length scales are used to define the electrodynamic response of the superconductor. The electron mean free path depends on the electron mobility, which is in turn dependent on temperature as well as the amount of impurities in the superconductor. The coherence length is derived from the intrinsic coherence length ξ_0, Equation 2-1. The ξ_0 is a lower limit of the coherence length and can only be obtained in clean materials where there are no impurities and l is very long. For dirty superconductors, for which l becomes short, the coherence length ξ is given by [27]

$$\frac{1}{\xi} = \frac{1}{\xi_0} + \frac{1}{l}. \tag{2-5}$$

In the same way that ξ is derived using ξ_0, the λ is derived from the London penetration depth λ_L. This is also a lower limit, defined by the brothers H. and F. London in [28] who derived it from Maxwell's equations for superconductors to be

$$\lambda_L(0) = \sqrt{\frac{m}{\mu_0 n_s e^2}} \tag{2-6}$$

where m is the electron mass, n_s the Cooper pair density and e the electron charge. As for Maxwell's equations, the magnetic field decreases exponentially over a certain length when it encounters a perfectly electric conductor, the same happens to a magnetic field when it encounters a superconductor. The London penetration depth is a theoretical limit for a pure (type-I) superconductor. For non-pure superconductors (type-II) the penetration depth is calculated using [29]

$$\lambda = \lambda_L \sqrt{1 + \frac{\xi_0}{l}}. \tag{2-7}$$

In the case of very thin superconductors, where the thickness t is smaller than l and therefore becomes the limiting factor, λ is described by the Pearl length [25] [30]

$$\lambda_\perp \approx \frac{2\lambda^2}{t^2}. \tag{2-8}$$

These three dimensions define whether the superconductor is operated in the clean or dirty limit and therefore define whether the response to an electromagnetic field is local or non-local [25]. The superconducting strips used to develop the phase shifter prototype are very thin. The superconducting strips are therefore operated in the dirty limit which means that $l < \xi_0$, and ρ is large. Applying this information in Equation 2-5 and Equation 2-8, it is implied that ξ is small and λ is large. When $\lambda \gg \xi$ the electrodynamic response is local because the Cooper pairs are effected by an electromagnetic field [25] [26]. For superconductors in the dirty limit with a local response, the electrodynamic response can be quantified through the complex conductivity. Another distinction which can be made is that when $\lambda > 1/\sqrt{2}\xi$, the metal is a type-II superconductor.

2-1-3 Complex conductivity

The concept of complex conductivity, $\sigma = \sigma_1 - i\sigma_2$, was derived by D. C. Mattis and J. Bardeen in [31] which is known as the Mattis-Bardeen theory. In this theory both the resistive response of the quasiparticles σ_1 and the inductive response due to the inertia of the Cooper pairs σ_2 are taken into account. The expressions for σ_1 and σ_2 are very complex, however, under the condition that $\hbar\omega$, $k_BT \ll \Delta$ these expressions can be simplified to [26]

$$\frac{\sigma_1}{\sigma_N} = \frac{4\Delta}{\hbar\omega} \exp\left(\frac{-\Delta}{k_BT}\right) \sinh\left(\frac{\hbar\omega}{2k_BT}\right) K_0\left(\frac{\hbar\omega}{2k_BT}\right) \tag{2-9}$$

$$\frac{\sigma_2}{\sigma_N} = \frac{\pi\Delta}{\hbar\omega}\left[1 - 2\exp\left(\frac{-\Delta}{k_BT}\right) \exp\left(\frac{\hbar\omega}{2k_BT}\right) I_0\left(\frac{\hbar\omega}{2k_BT}\right)\right] \tag{2-10}$$

where σ_N is the normal state conductivity and K_0 and I_0 are first and second kind of the modified Bessel functions of order 0. For very low temperatures the real part of the complex conductivity σ_1 and the change in the imaginary part of the complex conductivity σ_2 are proportional to the quasiparticle density given in Equation 2-2. The surface impedance for a thin superconducting film of thickness t is related to the complex conductivity through [25] [26] [32]

$$Z_s = \sqrt{\frac{i\mu_0\omega}{\sigma_1 - i\sigma_2}} \coth\left(\sqrt{i\omega\mu_0\sigma}t\right) = R_s + i\omega L_s \tag{2-11}$$

where the R_s is the surface resistance and L_s the surface inductance. For temperatures well below the T_c, where $\sigma_2 \gg \sigma_1$, and for an arbitrary film thickness t

$$R_s = \mu_0\omega\lambda\frac{\sigma_1}{2\sigma_2}\beta\coth\left(\frac{t}{\lambda}\right) \tag{2-12}$$

$$L_s = \mu_0\lambda\coth\left(\frac{t}{\lambda}\right) \tag{2-13}$$

where $\beta = 1 + 2(t/\lambda)/\sinh(2d/\lambda) \approx 2$ for thin films.

2-2 Biasing of superconductor

The resonant frequency of a superconducting resonator is affected by a change in temperature, the application of an external magnetic field and the injection of a dc bias current (not regarding changes in geometry). The effect of an external magnetic field and a dc bias current are related and can be observed through a change in the magnetic penetration depth λ. Even though the magnetic field biasing will not be used in this thesis, it serves to explain some important concepts such as the Meissner effect, intermediate state and vortexes. Since the effects of a magnetic field an dc current are analogous, these are later applied to the dc current. A change in temperature has an immediate effect on n_{qp}, Equation 2-2, and therefore Δ, Equation 2-4. This effect is not studied in this thesis. It is however important to keep in mind for measurements if the current locally heats the superconductor.

2-2-1 Response to magnetic field

In 1950, A. B. Pippard [27] applied an external magnetic field to a superconducting resonator. There are two conclusions to be drawn from this experiment which pertain to this thesis. The first is that he found that the application of an external magnetic field changed the resonant frequency. The second is that when applying an external magnetic field to a type-II superconductor (alloy), the resistivity no longer drops to zero for temperatures lower than T_c, but rather gently slopes down to zero. He called this transitioning state between normal and superconducting ($\rho = 0$) the intermediate state. In [33], A. A. Abrikosov found that this intermediate state is defined by two critical magnetic fields, H_{c1} and H_{c2}. For field strengths below H_{c1} the Meissner effect is observed and for field strengths above H_{c2} the superconductivity is lost as shown in Figure 2-3. The Meissner effect describes the diamagnetic property of a superconductor. An external magnetic field is effectively expelled from the superconductor by the surface currents which it induces [22]. The magnetic field can therefore only penetrate

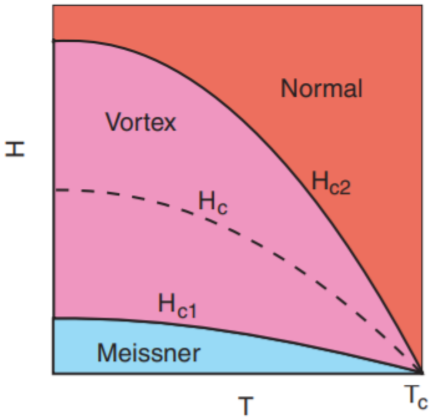

Figure 2-3: The different critical magnetic fields for type-I and type-II superconductors. Image taken from [34].

the superconductor by the magnetic penetration depth over a distance λ, Equation 2-7. The H_c in Figure 2-3 is the thermodynamic critical field of a type-I superconductor (pure metal).

There are two ways in which the magnetic field can destroy the superconducting state. The first is that a magnetic field increases the propagation velocity of the Cooper pairs, increasing their kinetic energy. When this added energy becomes larger than the condensation energy, the energy difference between the normal and superconducting state, the superconductive state becomes energetically less favorable and the superconductivity is lost [22][29][34]. The second way in which superconductivity is lost is through the formation of vortices and their combined movement. Vortexes are formed in the intermediate state. They are defined as areas where the magnetic flux can penetrate the superconductor completely (not just a distance of λ). Due to the normal core, the superconducting electron density n_s goes to zero in the center. This is shown in Figure 2-4, where $|\psi|^2 = n_s$ is the Ginzburg-Landau wave function. The core is roughly 2ξ, Equation 2-5, wide. Each vortex carries one flux quantum $\Phi_0 = h/2e$ and the vortex density n_L is such that $n\Phi_0 n_L$, n being an integer, is equal to the magnetic induction [33]. These areas consist of normal cores surrounded by superconducting currents. Ideally, vortexes arrange themselves in a triangular array in the superconductor. They are, however, pinned to impurities and irregularities in the geometry [30]. As long as these vortexes remain pinned the superconductivity is, on average, retained. The vortexes will remain pinned until a current of a certain value is induced by the magnetic field which induces a Lorentz force ($\mathbf{J} \times \Phi/c$) greater than the pinning force. If the vortexes move they experience a viscous drag which induces dissipation [35]. A voltage is therefore induced which means that the superconductivity is lost.

2-2-2 Response to current

Using the above described effects of a magnetic field, the effect of a dc current on a superconducting strip are now discussed in more detail. The effect of a dc current can be observed from two parameters: the kinetic inductance L_k and the energy gap Δ. These are discussed in the first two paragraphs. The application of a dc current is limited by the critical current

I_c, similar to H_c. This is discussed in the last paragraph.

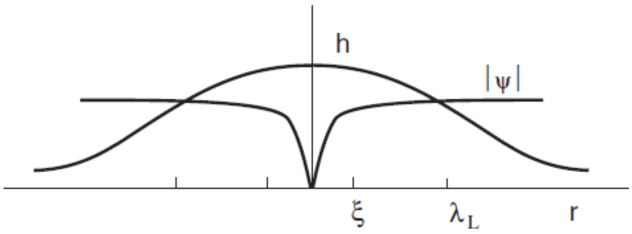

Figure 2-4: Structure of a vortex. The magnetic field is no longer expelled from the superconducting bulk since the superconducting electron density, $|\psi|^2 = n_s$, drops to zero at the core. Image taken from [34].

Kinetic inductance

Any strip of metal has an inherent capacitance and inductance due to its geometry. In addition to this, superconducting strips have a second source of inductance due to kinetic energy stored in the Cooper pairs, namely the kinetic inductance L_k. When applying a dc current, similar to the magnetic field, the kinetic energy of the Cooper pairs increases. This effects λ, Equation 2-7, which can immediately be seen as a change in L_s, Equation 2-13. The kinetic inductance is related to L_s through $L_k = L_s(l/w)$, where l and w are the length and width of the strip. The effect of the current on the kinetic inductance can be approximated by [11][12][17][36]

$$L_K(I) \approx L_K(0)\left[1 + \left(\frac{I}{I_*}\right)^2\right] \qquad \text{for } \frac{I}{I_*} \ll 1, \tag{2-14}$$

where $L_k(0)$ is the kinetic inductance at zero bias current, I is the applied bias current and I_* is a scale for the non-linearity. The value of I_* depends on the material and geometry of the superconductor and is in the order of the critical current I_c. As the applied current is increased, the kinetic inductance increases as well. When this is applied to a resonator this results in a decrease of resonant frequency (further explained in section 2-3). This effect is shown in the left panel of Figure 2-5 from [18]. In this plot, the applied current is normalized to the critical current which they denoted as I_Γ. The value of $L_k(0)$ can be approximated by [11][36]

$$L_k(0) = L_s(0)\frac{l}{w} \approx \frac{\hbar R_n}{\pi\Delta_0}\frac{l}{w} = \frac{\hbar}{\pi\Delta_0}\frac{\rho}{t}\frac{l}{w} \tag{2-15}$$

where $L_s(0)$ is the surface kinetic inductance, R_n is the normal state resistance and Δ_0 the energy gap at $T = 0$ calculated in Equation 2-3. This shows that the $L_k(0)$ and the change in kinetic inductance due to a bias current δL_k increases with the resistivity and inversely with the cross-sectional area of the superconductor.

Energy gap

The second effect which can be observed when a dc current is applied to a superconductor is that the density of states (DoS) of the quasiparticles is suppressed. This leads to a reduction in the energy gap [18][37][38] which is plotted in the right panel of Figure 2-5 from [18]. Here, the DoS is plotted for three different current values, the red line representing a very small current value, black a current value close to I_c and blue in between these two extremes. This suppression decreases the frequency threshold for which the superconductor becomes resistive, $\hbar\omega > 2\Delta$ in Figure 2-2. The reduction in the DoS accelerates the effect that a change in temperature has on the biasing of a superconductor.

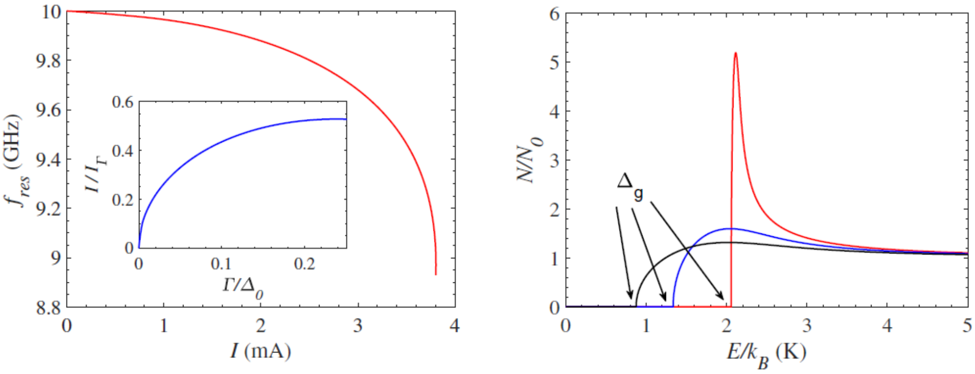

Figure 2-5: Left panel: Results of [18] show the change in resonant frequency due to an increase in the scaled bias current. Right pane: Results of [18] show the change in the superconducting density of states for different current values. In both graphs, the red curve represents a low current value and the black curve represents a current value near the pair-breaking current.

Critical current

Similar to the magnetic field, the dc current increases the kinetic energy of the Cooper pairs which is defined as

$$E_k = \frac{L_k I^2}{2} = 2N_0. \tag{2-16}$$

Another energy associated to Cooper pairs is their pairing energy E_p, which is the net attraction between the electrons in a Cooper pair, can be defined as

$$E_p = 2N_0\Delta^2 V. \tag{2-17}$$

When $E_k \geq E_p$, the bound state is energetically unfavorable and the superconductivity is lost. This is a theoretical value though, due to other phenomena such as vortex formation the superconductivity already is lost when E_k is slightly below E_p. The value of I_* can be calculated by equating the E_K to the E_p since this value is larger than (but in the same order as) I_c. The equation for I_* then becomes

$$E_k = E_p \quad \longrightarrow \quad \frac{L_k I^2}{2} = 2N_0\Delta^2 V \quad \longrightarrow \quad I_* = \sqrt{\frac{4\pi N_0 \Delta^3 V}{\hbar R_n}}, \tag{2-18}$$

where V is the volume of the superconductor. Knowing the value of I_* it is possible to approximate the value of I_c. For this approximation, the assumption that the current is uniformly distributed over the superconductor is necessary. This means that the thickness t and width w need to be smaller than the London penetration depth λ_L, Equation 2-6 [37].

The vortexes discussed in subsection 2-2-1 also play a role for in the application of the dc current. When $w < 4.4\xi$ it is impossible for vortexes to form. In this case it is possible to calculate the theoretical critical current. For realistic superconductors with imperfections, vortex flow can occur at current intensities of half the critical current [38][39].

Since N_0 in Equation 2-17 is not accurately known, a different approximation is needed. S. Zhao in [18] derived an expression for I_* from the Usadel equations [40] as

$$I_* = \frac{\sqrt{2} S \Delta_0 \sigma_N}{e\xi}. \tag{2-19}$$

where S is the cross-sectional area, σ_N the normal state conductivity and e the electron charge. The value of I_c is equal to roughly half of I_*. There is however, a small discrepancy between different studies as to the exact number. In [18][37] they find $I_c = 0.53 I_*$ while in [36][38] the find $I_c = 0.42 I_*$. It is the safest option to design the system for the lowest critical current value. It is imperative to keep its magnitude well below the critical current to avoid dissipation due to vortex movement.

2-3 Resonators

In the design used in this thesis there are two types of resonators: THz Fabry-Pérots [10], which are overmoded half-wavelength resonators surrounded by two weak couplers, and MKIDs [4], which are quarter-wavelength microwave resonators serving as detectors. The FP is in-line and open-circuited while the MKID is in-line with the FP but shunted with respect to the read-out line. The FP is implemented using a microstrip and is designed in such a way that it can be tuned by a dc bias current. The MKIDs are implemented using a coplanar waveguide (CPW). They will not be designed in this thesis and are taken from [10]. The characteristics of a superconducting microstrip resonator and the effect of a dc current on it will be treated first in this section. After this the quality factors, which are used to design an FP are discussed. To conclude this section, an overview of the MKID detector and all the signals is given.

2-3-1 Microstrip resonators

The cross-section of a microstrip is shown in Figure 2-6. The ground plane and conductor are separated by a dielectric. The signal line and the ground plane are separated by a dielectric slab with a dielectric material of ε_r. Due to fringing effects the electric field lines drawn in

Figure 2-6 are non-uniform. Since some lines travel through air before entering the dielectric a second permittivity needs to be defined, namely the effective permittivity ε_{eff} which, for a microstrip, is defined by [41]

$$\varepsilon_{eff} = 1 + \frac{(\varepsilon_r - 1)}{2}\left(1 + \frac{1}{\sqrt{1+\frac{10h}{w}}}\right). \tag{2-20}$$

B. Buijtendorp in [42] found that Equation 2-20 gives a better approximation than the standard calculation found in [43]. Using both ε_r and ε_{eff}, the filling factor p is derived. This defines how much of the electric field is concentrated in the dielectric and is defined by [43]

$$p = \frac{\varepsilon_r(\varepsilon_{eff} - 1)}{\varepsilon_{eff}(\varepsilon_r - 1)}. \tag{2-21}$$

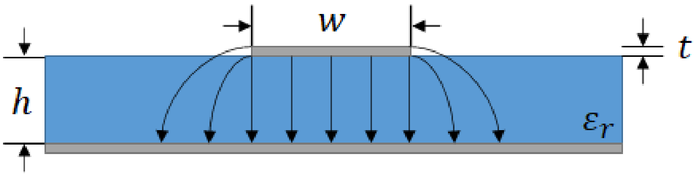

Figure 2-6: Cross section of a microstrip.

The microstrip resonator can be used to create an in-line FP by terminating both sides with an open circuit. This can be implemented by capacitors as shown in Figure 2-7. The entire structure can be modeled using S-parameters which define how much power is reflected from the two ports, S_{11} and S_{22}, and how much is transmitted between the ports, S_{12} and S_{21}. Assuming that the capacitors C_1 and C_2 are equal, due to the symmetry of the network, $S_{11} = S_{22}$ and $S_{12} = S_{21}$. These S-parameters are extremely useful for the design of the individual couplers and later, the analysis of the FP. The transmission through a coupler $S_{21,c}$ determines how much power is transferred into the FP and later out of it (into the MKID). This can be calculated through

$$S_{21,c} = \frac{2\sqrt{\mathbb{R}\{Z_1\}\mathbb{R}\{Z_2\}}}{Z_1 + \frac{1}{j\omega C} + Z_2} \tag{2-22}$$

where Z_1 and Z_2 are the impedances of port 1 and 2, ω the angular frequency and C the capacitance of the coupler. When designing the FP itself, the two most important parameters are its characteristic impedance Z_0 and propagation constant $\beta = 2\pi/\lambda$.

The frequency behavior of the microstrip resonator is defined by its natural resonant frequency f_0 through

$$f_0 = \frac{v_p}{2l} = \frac{c_0}{2l\sqrt{\varepsilon_{eff}}} = \frac{1}{2l\sqrt{(\mathcal{L}_g + \mathcal{L}_k)\,\mathcal{C}}} \tag{2-23}$$

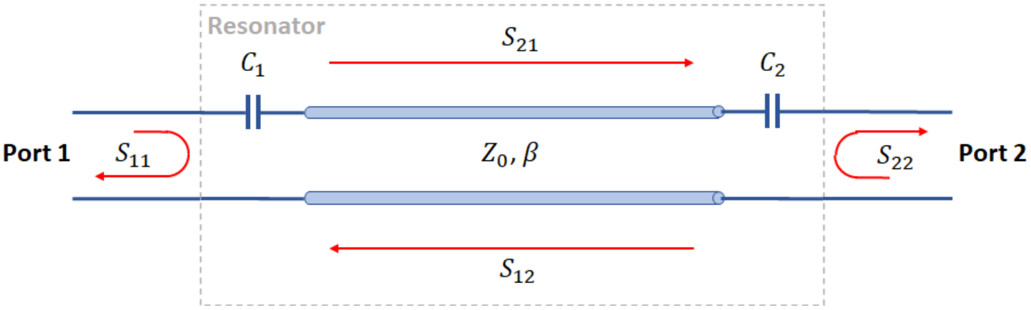

Figure 2-7: Two-port network representation of an in-line resonator. The resonator itself is capacitively coupled on both sides, so it has approximately open-ended terminations. The line itself is characterized by its impedance Z_0 and propagation constant β.

where v_p is the phase velocity, l is the length of the resonator, c_0 the speed of light in vacuum, ε_{eff} the effective permittivity, $\mathcal{L}_g$ is the geometric inductance per unit length, $\mathcal{L}_k$ (Equation 2-15 divided by the length) the kinetic inductance per unit length and $\mathcal{C}$ the geometric capacitance per unit length. When a resonator is electrically long, it can ring at multiple resonance frequencies f_n which are related to the natural resonant frequency f_0 by the mode number n as

$$f_n = nf_0 \qquad \text{for } n = 1, 2, 3, ... \tag{2-24}$$

At these resonance frequencies a standing wave pattern is produced on the resonator as shown in Figure 2-8. Due to the open-ended terminations of the FP, the current is forced to zero at the ends while the voltage is at a maximum. The locations on the resonator where the voltage is zero along the FP are called voltage nodes and where the current is zero, current nodes. The mode number n corresponds to the amount of voltage nodes/current anti-nodes in an open-ended FP. As can be seen from the impedance line in the plot, at voltage nodes the line impedance reaches zero and at current nodes it tends to infinity. The locations of these nodes shift as n changes.

The output of a FP with $f_0 \approx 8$ GHz is shown in Figure 2-9. Above f_0 the resonator only transmits the signal when the frequency is equal to f_n. The -3 dB bandwidth of the peaks is referred to as a line width. Therefore, only the signals with a frequency of f_n are transmitted to the MKID.

2-3-2 Effect of current

As discussed in subsection 2-2-2 a bias current affects the L_k (Equation 2-14) by changing the λ (Equation 2-7). The change in L_k can be expressed using the kinetic inductance fraction α which shows the ratio of the L_k to the total inductance of the resonator through

$$\alpha = \frac{\mathcal{L}_k}{\mathcal{L}_g + \mathcal{L}_k} \approx \frac{2\lambda}{h + 2\lambda} \tag{2-25}$$

where h is the height of the dielectric as shown in Figure 2-6. The second approximation can only be applied to an ideal microstrip where the fringing fields are neglected [36]. The effect

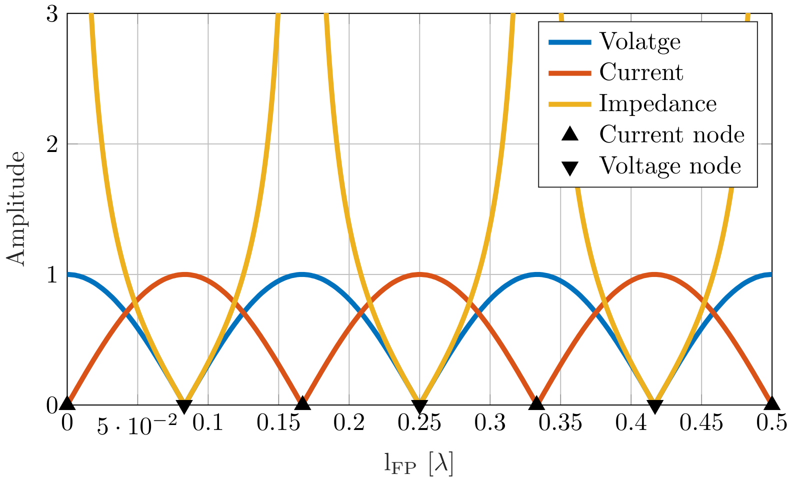

Figure 2-8: Standing wave pattern on FP for mode 3. The voltage and current nodes are marked with downward and upward facing triangles, respectively. Due to the open termination the current will always be zero at the ends and the voltage will be maximum.

of a change in L_k and thus α can be expressed in a change in f_0 through a change in the phase velocity v_p of the signal. This can be written as [11]

$$v_p = \frac{1}{\sqrt{(\mathcal{L}_g + \mathcal{L}_k)\,\mathcal{C}}} \approx v_p(0)\left(1 - \alpha \frac{I^2}{2I_*^2}\right), \tag{2-26}$$

where $v_p = \omega/\beta = 2\pi\omega/\lambda$. The resonant frequency, Equation 2-23, can then be rewritten to incorporate the effect of the current through

$$f_0 = \frac{1}{2l} c\sqrt{1-\alpha}\sqrt{\frac{1}{\varepsilon_{eff}}} \approx \frac{v_p(0)}{2l}\left[1 - \alpha\left(\frac{I}{2I_*}\right)^2\right]. \tag{2-27}$$

The resonant frequency is shifted to lower frequencies when a dc current is applied. Therefore, the sensitivity of a superconductor to a bias current improves for large α. This can be specified using Equation 2-15 to materials with a large normal state resistivity and small cross-sectional area [12][36].

It is possible that the dc current can affect the line width of the Figure 2-9. The line width widens when n_{qp} increases due to Cooper pairs which are broken. As long as the applied current is well below I_c this should not be the case as shown in [15] and [16]. There is a probability that the current could locally heat the FP, causing Cooper pairs to break due to thermal excitations.

2-3-3 Quality factors

The quality factor of a resonator is defined as the energy stored in the resonator over the power lost per cycle [10][26].

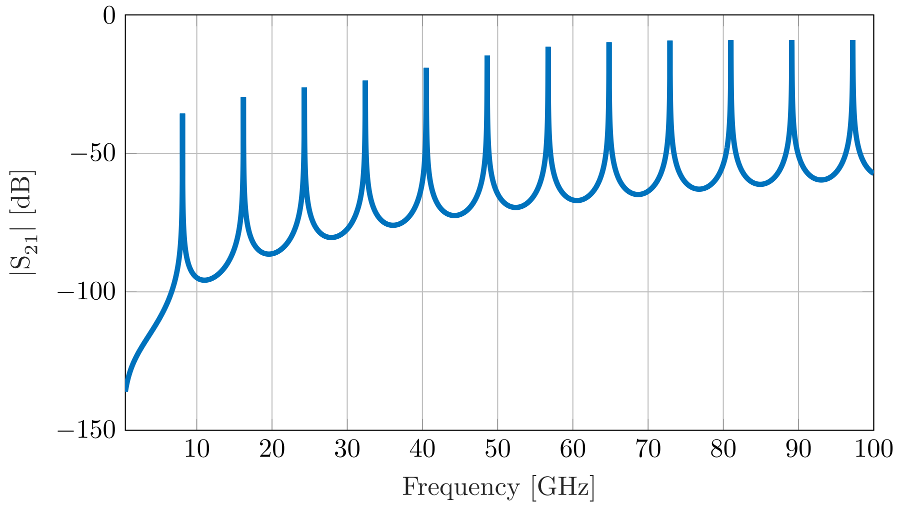

Figure 2-9: The output of a resonator. The peaks represent the different modes of the resonator, located at $f = nf_0$. The -3 dB bandwidth of each peak is called the linewidth.

$$Q = \omega \frac{\text{energy stored}}{\text{Power lost}} \tag{2-28}$$

The total Q-factor of a resonator is also known as the loaded Q-factor Q_l, which describes the performance when the resonator is connected to the rest of the circuitry. The loaded quality factor of the resonator in Figure 2-7 can be described in terms of the Q-factors of the energy leaking mechanisms as

$$\frac{1}{Q_l} = \frac{1}{Q_i} + \frac{1}{Q_{c1}} + \frac{1}{Q_{c2}} \tag{2-29}$$

where Q_i is the internal Q-factor modeling the losses, such as radiative or ohmic in the dielectric, as Q_{c1} and Q_{c2} respectively represent the coupling Q-factors of coupler 1 and 2 and the power transmitted through them. A high quality factor means a small leakage of energy, so a high Q_i represents a low loss FP and a high Q_c a weak coupler. Using Equation 2-28, the coupling quality factor of one of the two coupling capacitors can be written as

$$Q_{c1} = \frac{\omega E_{stored}}{P_{lost}} = \frac{\omega E_{stored}}{\frac{f E_{stored} |S_{21,c}|^2}{n}} = \frac{2\pi n}{|S_{21,c}|^2}, \tag{2-30}$$

where n is the mode number (Equation 2-24) and $|S_{21,c}|^2$ the transmission through a capacitor. Assuming that the coupling capacitors are identical, the total Q_c is given by [10]

$$Q_c = \left(\frac{1}{Q_{c1}} + \frac{1}{Q_{c2}} \right)^{-1} = \frac{\pi n}{|S_{21,c}|^2}. \tag{2-31}$$

In this thesis, the values of Q_i are not specifically calculated but are obtained from the experiments done in [10]. The calculations and experimentally obtained values allow for a first order approximation of the Q_l. After fabrication however, these values can differ. Another method of obtaining the value of Q_l is through the $|S_{21}|$ linewidths of Figure 2-9 for any resonance f_n as

$$Q_l = \frac{f_n}{BW_{-3dB}}, \tag{2-32}$$

where BW_{-3dB} is the bandwidth where the magnitude of the response around f_n has halved or, in other words, is -3 dB lower than the peak value.

2-3-4 MKID detector

The MKIDs used in this design are hybrid MKIDs. Their design and operation are briefly explained here. Afterwards, the addition of the FP resonator and the dc bias is discussed.

Hybrid MKIDs

The hybrid MKID design for this thesis is constructed from Niobium Titanium Nitride (NbTiN) and Aluminium (Al). An example of such an MKID, without FP, is shown in Figure 2-10 from [44]. The wider NbTiN and the narrow Al section together form the $\lambda/4$ CPW microwave resonator. NbTiN is a type-II superconductor and has a critical temperature of roughly 15 K which means that it is completely lossless up until

$$\nu = 2\frac{\Delta_0}{h} = 2\frac{1.76 k_B T_c}{h} \approx 73.6 T_c \text{ GHz} = 1.1 \text{ THz}. \tag{2-33}$$

Al is a type-I superconductor with $T_c \approx 1.28$ K which is superconducting until a frequency $\nu \approx 90$ GHz. Radiation with frequencies of $90 < \nu < 1100$ GHz will break Cooper pairs in the Al strip, but not in the NbTiN strip. The Al strip is galvanically connected to the NbTiN ground plane on the antenna side and to the NbTiN central line on the read-out side. This traps the Al Cooper pairs and quasiparticles in the Al strip allowing the baseline response to remain the same. The reason this quantum well is formed is because the NbTiN has a much higher gap energy which leads to Andreev reflections. By making the Al section very thin, the response of the KID is maximized [44].

The MKIDs are capacitively coupled to a read-out line which can be seen in the bottom right corner of Figure 2-10. A microwave signal is sent through the read-out line and when its frequency coincides with the resonant frequency of the KID, a dip can be measured in the transmission of the read-out line as shown in Figure 2-11. If the frequency of the microwave signal does not coincide with the resonant frequency nothing will happen, there will be no loss in transmission of the read-out line. This is what allows the KIDs to be multiplexed: they can all be designed to have different resonant frequencies and can therefore be read-out at the same time with a comb of microwave probing tones.

The operation of (hybrid) MKIDs depends on the changes in the surface impedance, Equation 2-11, caused by pair breaking radiation, $\hbar\omega > 2\Delta$. When the Cooper pairs break, increasing the quasiparticle density n_{qp}, Equation 2-2. For $T \ll T_c$, a change in surface

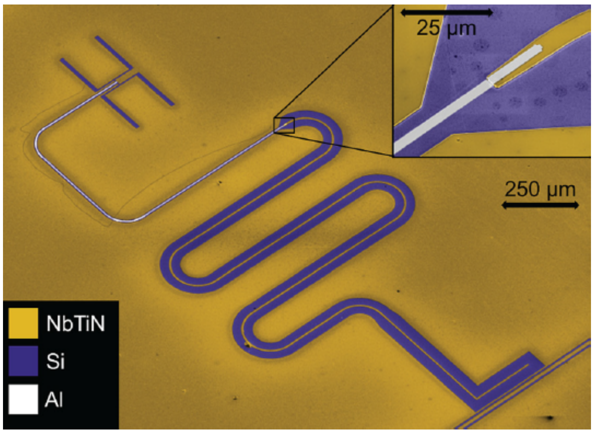

Figure 2-10: Hybrid NbTiN-Al MKID design of [44].

impedance and thus a change in complex conductivity, Equation 2-9 and Equation 2-10, is proportional to n_{qp}. This relation is written as [25][45]

$$\frac{d\sigma_1}{dn_{qp}} \simeq \sigma_N \frac{1}{N_0 \hbar\omega} \sqrt{\frac{2\Delta_0}{\pi k_B T}} \sinh\left(\frac{\hbar\omega}{2k_B T}\right) K_0\left(\frac{\hbar\omega}{2k_B T}\right) \tag{2-34}$$

$$\frac{d\sigma_2}{dn_{qp}} \simeq \sigma_N \frac{-\pi}{2N_0 \hbar\omega} \left[1 + 2\sqrt{\frac{2\Delta_0}{\pi k_B T}} \exp\left(\frac{\hbar\omega}{2k_B T}\right) I_0\left(\frac{\hbar\omega}{2k_B T}\right)\right]. \tag{2-35}$$

For small fluctuations in n_{qp} and $T << T_c$ these behave almost linearly with n_{qp}. Similar to the effect of a current on a superconducting strip, the resonant frequency of the MKID, as well as its the Q_i, vary almost linearly as well [25]

$$\frac{\delta f}{f} = \frac{\alpha\beta}{4} \frac{\delta\sigma_2}{\sigma_2} \tag{2-36}$$

$$\delta\left(\frac{1}{Q_i}\right) = \frac{\alpha\beta}{2} \frac{\delta\sigma_1}{\sigma_2}, \tag{2-37}$$

where

$$Q_i = \frac{\omega L}{R} = \frac{1}{\alpha} \frac{\omega L_s}{R_s} = \frac{2}{\alpha\beta} \frac{\sigma_2}{\sigma_1} \tag{2-38}$$

$$\beta = 1 + \frac{2t/\lambda}{\sinh\left(2t/\lambda\right)}. \tag{2-39}$$

These changes in f and Q_i can be seen in the response of the read-out line as shown in Figure 2-11. For larger n_{qp} the resonance dip shifts to lower frequencies and becomes shallower.

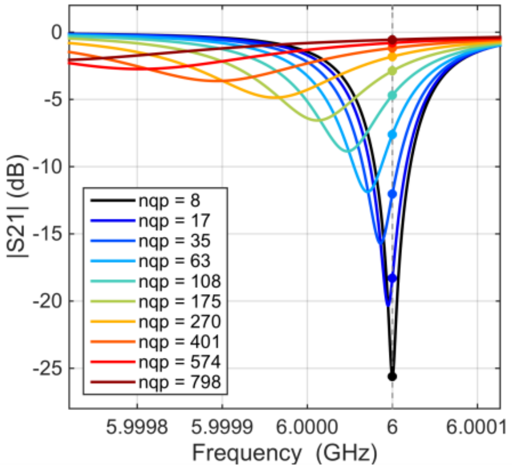

Figure 2-11: Effect of the change in f and Q_i of the KID on the read-out line. Image taken from [46].

Addition of Fabry-Pérot resonator

In [10] the previously discussed MKID design was expanded by adding a $\lambda/2$ FP resonator in series between the antenna and the MKID resonator. This resonator is used to measure the characteristics of superconducting microstrip lines at high frequencies with extremely high precision. Due to the fact that the FP is capacitively coupled to the rest of the circuit, any dc signal injected into it cannot couple to the rest of the circuit. Running a dc current through a superconductor changes its resonance behavior, and therefore tunes the input signal of the MKID and its response without physically changing any parameters of the MKID. A schematic overview of the entire circuit is shown in Figure 2-12. The FP, Al MKID section and NbTiN MKID section are represented by transmission lines. The FP is capacitively coupled on both sides and the MKID is shunted to the read-out line. The three differently colored lines represent the three signals running through the system: the dc bias, the THz signal measured by the antennas and the microwave read-out signal.

2-4 Low-pass stepped-impedance filters

A low-pass filter allows all frequencies below a certain cut-off frequency ω_c to pass through it while effectively blocking all frequencies higher than ω_c. The cut-off frequency is defined as the point where the transmission of the signal power is halved. The frequency range $0 < \omega < \omega_c$ is called the pass-band and the frequency range of $\omega > \omega_c$ is called the stop-band. An ideal low-pass filter is referred to as a brick wall filter and its transfer function is shown on the left of Figure 2-13. In an ideal filter the transition from pass-band to stop-band is very sharp, there is no attenuation of the signal in the pass-band and no transmission in the stop-band. The template of a realistic low-pass filter is shown on the right of Figure 2-13. This shows a transition band of $\omega_p < \omega_c < \omega_s$, some maximum allowable attenuation A_p in the pass-band and a minimum allowable transmission level A_s in the stop-band. From these restrictions the filter function and the necessary filter order can be derived. The filter function can take any

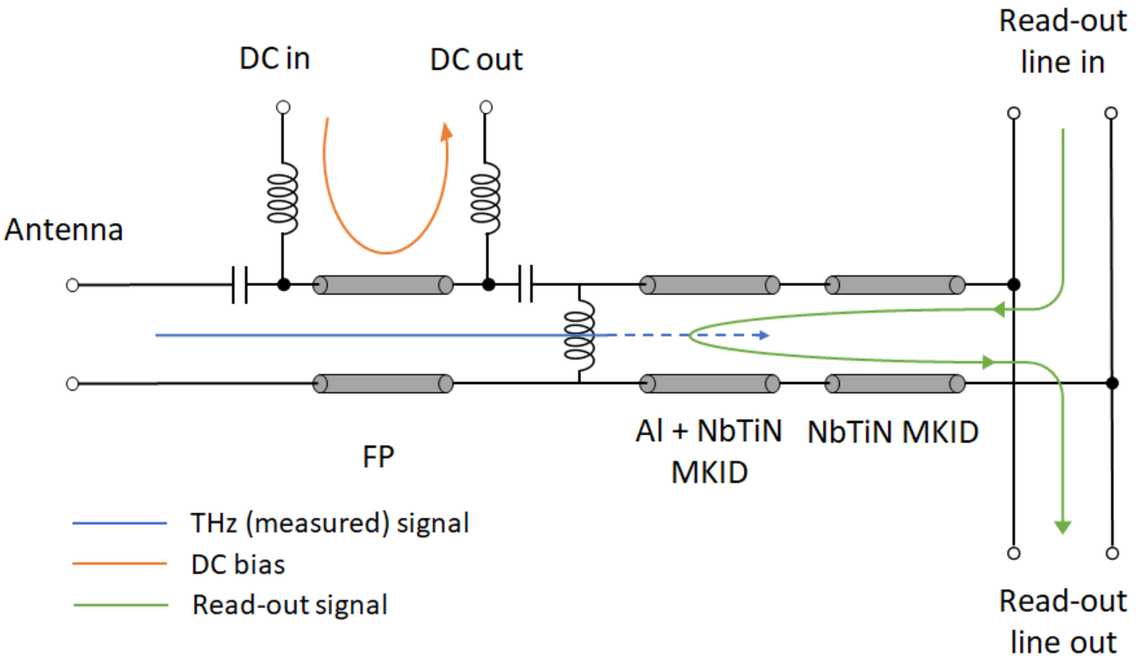

Figure 2-12: Two-port network representation of complete detector. The THz signal is absorbed in the Al part of the MKID. The dc bias signal only runs through the FP and is injected and removed through a low-pass filter, represented here by a series inductor. The shunt inductor serves as a short for the $\lambda/4$ MKID and is almost an open circuit for the THz signal. The read-out signal, typically a few GHz, is coupled into the MKID when its frequency coincides with the resonant frequency of the MKID. This results in a transmission dip in the read-out signal at that frequency.

shape as long as it remains within in the predefined white area. This section will treat two widely used filter functions, namely the Butterworth and Chebyshev filter functions.

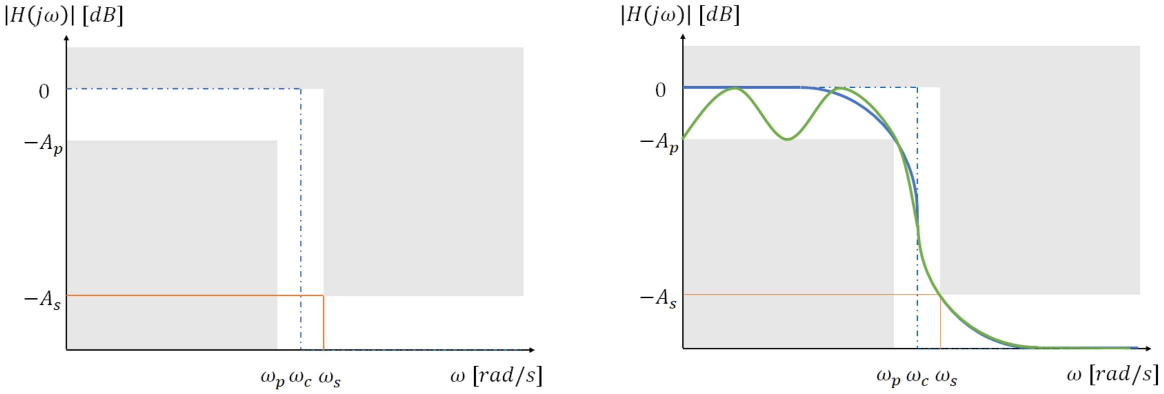

Figure 2-13: Ideal (left) and realistic (right) low-pass filter characteristics. The two realistic filter functions which are also discussed here are the Butterworth (blue) and the Chebyshev (green) responses.

To synthesize these filtering functions either lumped elements or transmission lines can be used. Given the high frequencies under investigation ($300 - 400$ GHz) and the current microfabrication capabilities [47], a transmission line approach is needed. For this we make use of stepped-impedance filters, which approximate the behavior of series and shunt reactive lumped elements.

Ladder networks such as the lumped-element filter shown in the top panel of Figure 2-14 and its analogous stepped-impedance filter shown in the bottom panel of Figure 2-14 are known as minimum phase networks. These are defined as systems where there is only one signal path which directly links the input to the output [48]. Minimum phase systems are stable systems because they have the requirement that the poles of the transfer function can only lie in the left-half plane (LHP) or on the imaginary axis of the complex plane. Another characteristic is that they have the exact same transfer function looking into both filter ports. It therefore does not matter which side of the filter you attach. A low-pass filter implementation of a stepped-impedance filter of order N consists of N sections synthesizing N reactive elements: alternating cascaded series inductors and shunt capacitors. The low-pass filter consists of N reactive elements, cascaded series inductors and parallel capacitors, and is called the filter order. At dc, the inductors behave as a short while the capacitors behave like an open, allowing the signal to pass. As the frequency increases the roles are swapped and the high-frequency signal will be effectively blocked.

In the following subsections the derivation and synthesis of stepped-impedance filters will be shown. For this analysis the filter is viewed as a passive lossless two-port network. The values of the components in the network can be determined from the input impedance of the network $Z_n(j\omega)$. The input impedance can be related to the reflection coefficient $S_{11}(j\omega)$ of the two-port network through

$$Z_n(j\omega) = \frac{1 + S_{11}(j\omega)}{1 - S_{11}(j\omega)}. \tag{2-40}$$

From the assumption that the two-port network is passive and lossless, the reflection coefficient is related to the transmission coefficient by $|S_{11}(p)|^2 + |S_{12}(p)|^2 = 1$. Therefore, if $S_{11}(j\omega)$ is a bounded function, it is possible to derive the component values from $Z_n(j\omega)$ [49].

2-4-1 Filter functions

The main difference between the Butterworth and the Chebyshev response is their behavior in the pass-band. The Butterworth response is also known as a maximally flat response which means that it has a flat transfer until ω_p. The Chebyshev filter has an equiripple pass-band response. This means that there is a ripple in the transmission between two set values in the pass-band. In the example of Figure 2-13 the ripple is between 0 and A_p. This ripple comes at the benefit of a steeper roll-off rate and thus a smaller transition period. Both functions have their zero transmission at infinity meaning they can be characterized as all-pole networks, which have the property that their magnitude squared transfer function can be written as [48]

$$|S_{12}(p)|^2 = \frac{1}{D_N(j\omega)\, D_N(-j\omega)}, \tag{2-41}$$

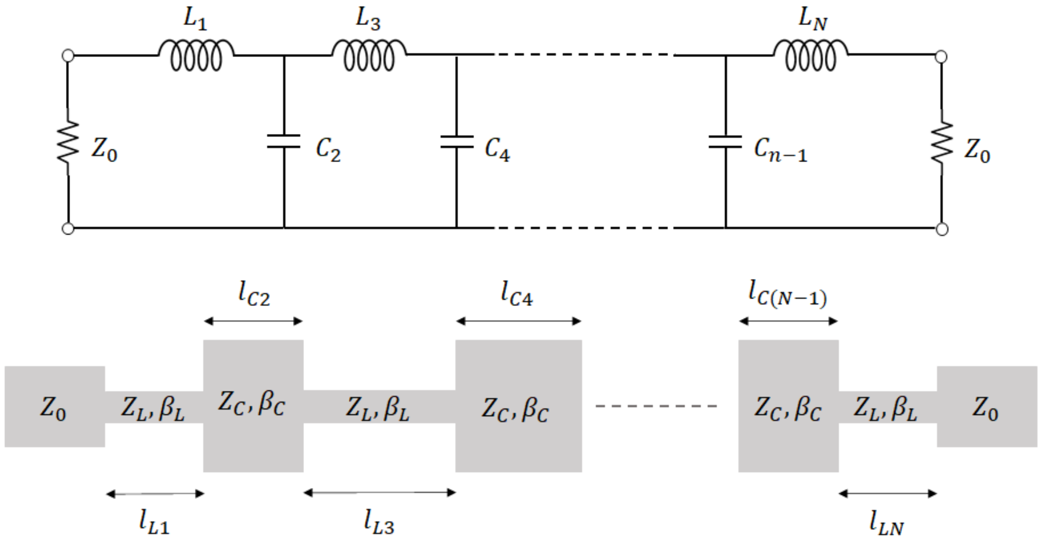

Figure 2-14: Top panel: Lumped-element ladder network. Bottom panel: Distributed-element ladder network, analogous to lumped-element ladder network.

where $D_N(j\omega)$ and $D_N(-j\omega)$ are the complex conjugates of the denominator of the all-pole transfer function. The poles of this function should all be in the left-hand plane (LHP) or on the imaginary axis of the complex plane for the filter to be stable. For the following derivations it is assumed that the source and load impedances on each side of the filter are equal to each other, that all impedances in the network are normalized to the source impedance, that all frequencies are normalized to the cut-off frequency and that $|S_{21}(j\omega)|^2 = 1$ in the pass-band.

Butterworth response

For a real lumped element network the filter function is finite and can be written as a proper rational function as [49]

$$|S_{12}(j\omega)|^2 = \frac{\sum_{i=1}^{m} a_i \omega^{2i}}{\sum_{i=1}^{n} b_i \omega^{2i}} \qquad b_n > 0. \tag{2-42}$$

The Butterworth response is also known as a maximally flat response. This is because the first $2n-1$ derivatives of Equation 2-40 can be equated to zero at $\omega = 0$ and $\omega = \infty$. When applying this condition together with the low-pass conditions, $|S_{21}(j0)|^2 = 1$ and $|S_{21}(j\infty)|^2 = 0$, then $a_i = b_i = 0$ for $i \longrightarrow n-1$ and Equation 2-42 reduces to

$$|S_{12}(j\omega)|^2 = \frac{1}{1+\omega^{2N}}, \tag{2-43}$$

which is known as the Butterworth response. The filter order N is derived in Appendix A and it is calculated as

$$N \geq \left\lceil \frac{1}{2} \frac{\log_{10} \frac{\left(10^{A_p/10}-1\right)}{\left(10^{A_s/10}-1\right)}}{\log_{10}\left(\frac{\omega_p}{\omega_s}\right)} \right\rceil . \tag{2-44}$$

To find the transmission characteristic it is necessary to first find the poles of the Butterworth response. The poles occur when

$$\omega^{2N} = -1 = \exp j\pi(2n-1) \quad \rightarrow \quad \omega_n = \exp \frac{j\pi(2n-1)}{2N} \quad n = 1, ..., N. \tag{2-45}$$

And thus the poles can be written as

$$p_n = j\omega_n = j\exp\left(j\theta_n\right) = -\sin\left(\theta_n\right) + j\cos\left(\theta_n\right), \tag{2-46}$$

where

$$\theta_n = \frac{\pi(2n-1)}{2N} \quad n = 1, ..., N. \tag{2-47}$$

All the poles lie in the LHP (if N is even) and on the imaginary axis as well (if N is odd). These poles are equally spaced on the unit circle as shown on the left of Figure 2-15. Using these poles, the filter is stable and the expression for the transmission coefficient can therefore be written as [49] [50].

$$S_{12}(p) = \frac{1}{\prod_{n=1}^{N}\left[p - j\exp\left(j\theta_n\right)\right]}. \tag{2-48}$$

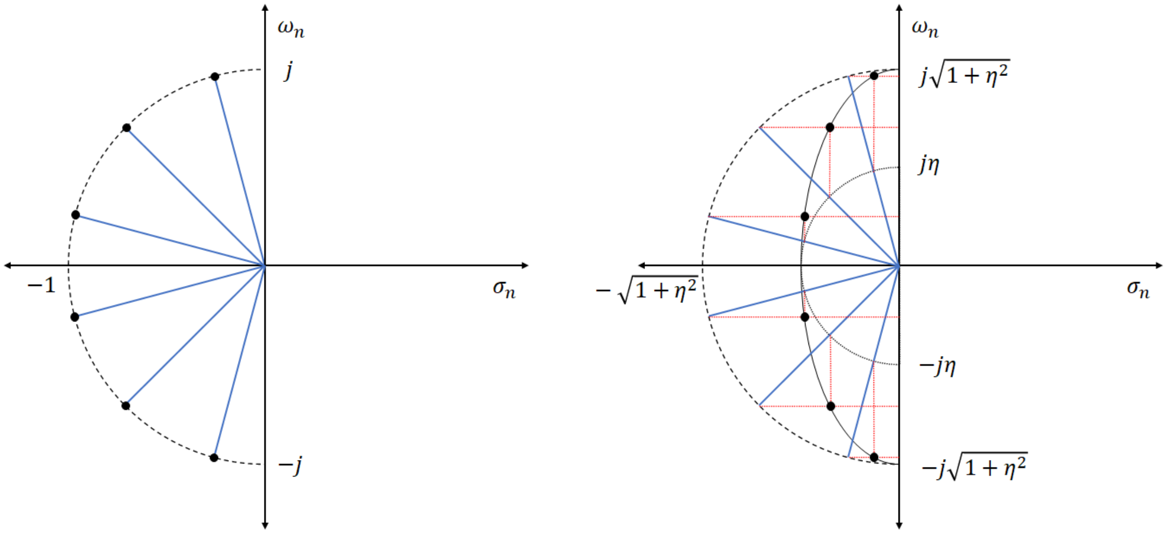

Figure 2-15: Poles of Butterworth transfer function (left) and Chebyshev transfer function (right).

The next step in the synthesis is to find the corresponding function for $S_{11}(p)$, which may be written as

$$S_{11}(p) = \frac{\pm p^N}{\prod\limits_{n=1}^{N} \left[p - j\exp\left(j\theta_n\right)\right]}. \tag{2-49}$$

The positive sign should be taken if the first element is an inductor and the negative sign if the first element is a capacitor [48]. Using Equation 2-40, the value of the coefficients in front of the poles give the impedance and frequency normalized values of the elements. The coefficients can easily be calculated from Equation 2-49 if N is small. If N is large, J. Hong derived in [50] an expression to obtain these values assuming that the filter is matched on both sides. These impedance and frequency-normalized values of the N reactive filter elements can be found using

$$g_n = 2\sin\left(\frac{(2n-1)\pi}{2N}\right) \qquad \text{for } n = 1, ..., N \tag{2-50}$$

Chebyshev response

In the case of the Chebyshev response there is a ripple in the pass-band which can be described by

$$A = \begin{cases} 1 & \text{for } N \text{ odd} \\ \frac{1}{1+\varepsilon^2} & \text{for } N \text{ even.} \end{cases} \tag{2-51}$$

Applying this ripple and the maximally flat condition to the stop-band $\left|S_{21}(j\infty)\right|^2 = 0$, Equation 2-42 reduces to

$$\left|S_{12}(j\omega)\right|^2 = \frac{A}{1 + \varepsilon^2 T_N(\omega)^2} \tag{2-52}$$

which is known as the Chebyshev response. The function $T_N(\omega)$ is the Chebyshev function defined in Equation 2-53 and is plotted in Figure 2-16 for different values of N.

$$T_N(\omega) = \begin{cases} \cos\left(N\cos^{-1}\omega\right) & \omega < 1 \\ \cosh\left(N\cosh^{-1}\omega\right) & \omega \geq 1. \end{cases} \tag{2-53}$$

The ripple of the filter is defined by

$$\varepsilon = \sqrt{10^{A_p/10} - 1} \tag{2-54}$$

and the order of the filter is be calculated from Equation 2-55. The derivation of N is also given in Appendix A.

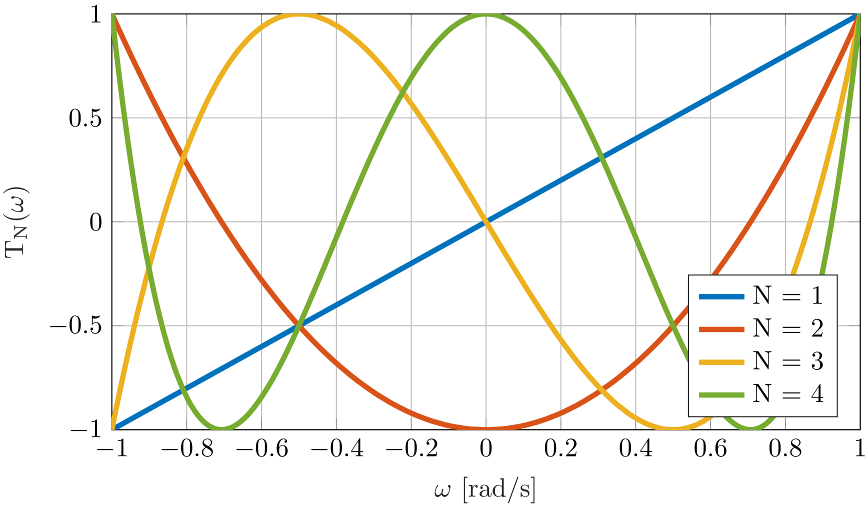

Figure 2-16: Chebyshev function for $N = 1$ to $N = 4$.

$$N \geq \left\lceil \frac{\cosh^{-1}\sqrt{\frac{10^{A_s/10}-1}{10^{A_p/10}-1}}}{\cosh^{-1}\left(\frac{\omega_s}{\omega_c}\right)} \right\rceil \tag{2-55}$$

As with the Butterworth filter, the poles of Equation 2-52 must be found. To help with this, an auxiliary parameter η is defined [49] as

$$\eta = \sinh\left(\frac{1}{N}\sinh^{-1}\frac{1}{\varepsilon}\right) \quad \rightarrow \quad \frac{1}{\varepsilon} = \sinh\left(N\sinh^{-1}\eta\right). \tag{2-56}$$

To start with the Chebyshev function itself, Equation 2-53, the zeros of the function in the pass-band are found at

$$\omega_n = \cos\frac{(2n-1)\pi}{2N} \qquad n = 1, ..., N. \tag{2-57}$$

The poles of the Chebyshev filter, Equation 2-52, are located at

$$\varepsilon^2 T_N^2(\omega_n) = -1 \quad \rightarrow \quad T_N^2(\omega_n) = -\frac{1}{\varepsilon^2}. \tag{2-58}$$

Using the auxiliary parameter defined in Equation 2-56, the poles occur at

$$\begin{aligned}
\cos^2\left(N\cos^{-1}\omega_n\right) &= -\sinh^2\left(N\sinh^{-1}\eta\right) = -\sinh^2\left(-jN\sin^{-1}j\eta\right) \\
&= -j^2\sin^2\left(-j^2N\sin^{-1}j\eta\right) = \sin^2\left(N\sin^{-1}j\eta\right) \\
\cos^2\left(N\cos^{-1}\omega_n\right) &= \sin^2\left(N\sin^{-1}j\eta\right) \\
\cos\left(N\cos^{-1}\omega_n\right) &= \sin\left(N\sin^{-1}j\eta\right) \\
\cos\left(N\cos^{-1}\omega_n\right) &= -\cos\left(N\sin^{-1}j\eta + \frac{(2n-1)\pi}{2}\right) \\
N\cos^{-1}\omega_n &= -N\sin^{-1}j\eta + \frac{(2n-1)\pi}{2} \\
\omega_n &= -\cos\left(\sin^{-1}j\eta + \frac{(2n-1)\pi}{2N}\right) \quad n = 1,...,N.
\end{aligned} \tag{2-59}$$

which means that

$$p_n = j\omega_n = -j\cos\left(\sin^{-1}j\eta + \frac{(2n-1)\pi}{2N}\right) \quad n = 1,...,N. \tag{2-60}$$

The poles are located on an ellipse as shown on the right of Figure 2-15. The expression for the transmission function can be written as [49]

$$S_{12}(p) = \frac{A^{1/2}\prod_{n=1}^{N}\left[\eta^2 + \sin^2\left(\frac{n\pi}{N}\right)\right]^{1/2}}{\prod_{n=1}^{N}\left\{p + j\cos\left(\sin^{-1}j\eta + \theta_n\right)\right\}} \tag{2-61}$$

where θ_n is the same as Equation 2-47. The corresponding function for $S_{12}(p)$ is [48]

$$S_{11}(p) = \frac{A^{1/2}\prod_{n=1}^{N}\left\{p + j\cos\left(\theta_n\right)\right\}}{\prod_{n=1}^{N}\left\{p + j\cos\left(\sin^{-1}j\eta + \theta_n\right)\right\}}. \tag{2-62}$$

Again using Equation 2-40, the values of the coefficients in front of the poles give the impedance and frequency normalized values of the elements. J. Hong derived in [50] an expression to obtain the normalized values of the filter elements from Equation 2-62, assuming that the filter is matched on both sides

$$g_1 = \frac{2}{\gamma}\sin\left(\frac{\pi}{2N}\right) \tag{2-63}$$

$$g_n = \frac{1}{g_{n-1}}\frac{4\sin\left(\frac{(2n-1)\pi}{2N}\right)\sin\left(\frac{(2n-3)\pi}{2N}\right)}{\gamma^2 + \sin^2\left(\frac{(n-1)\pi}{N}\right)} \quad \text{for } n = 2,3,...,N, \tag{2-64}$$

where g_n is the impedance and frequency normalized for each filter element and

$$\beta = \ln\left[\coth\left(\frac{A_p}{17.37}\right)\right] \tag{2-65}$$

$$\gamma = \sinh\left(\frac{\beta}{2N}\right). \tag{2-66}$$

2-4-2 Filter synthesis

A stepped-impedance filter as shown in Figure 2-17 is an alternating cascade of transmission line sections with low and high characteristic impedances which approximately synthesize shunt capacitors and series inductors, respectively. For this approximation to work, the transmission line sections need to be much shorter than the effective wavelength. For a microstrip implementation, the width of the conductor can be used to modify the characteristic impedance of the line, determining thereby whether the microstrip section behaves inductively or capacitively. The derivation is shown in Appendix B. It is necessary that Z_0, the characteristic impedance of the source/load lines, lies between the impedance of the inductive and capacitive sections: $Z_C < Z_0 < Z_L$. The larger the contrast between Z_C and Z_L, the stronger the effect of the filter can be. The value of Z_C is limited by the maximum attainable microstrip width, which in turn is limited by any extraneous resonant behavior and practically limited by the finite space available. The value of Z_L on the contrary is limited by current micro-fabrication capabilities [47] and the maximum tolerable current density.

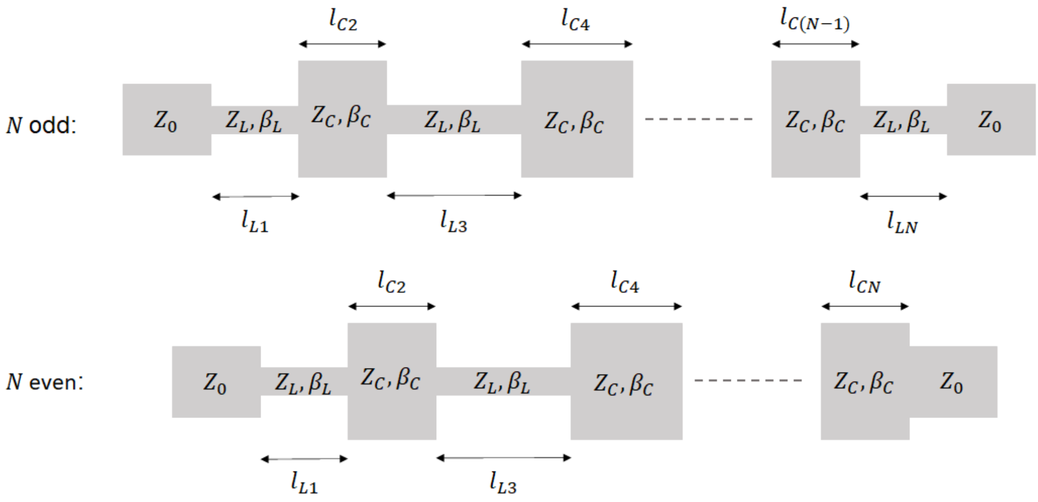

Figure 2-17: Stepped-impedance filter for odd N and even N.

In the previous section the values of g_n were derived. Re-scaling these values with the normalizing impedance Z_0 and cut-off frequency ω_c and applying the approximation for electrically short lines as shown in Appendix B, the actual line lengths can be obtained from

$$l_L = \frac{g_n Z_0}{Z_L \beta_L} \tag{2-67}$$

$$l_C = \frac{g_n Z_C}{Z_0 \beta_C} \tag{2-68}$$

where Z_L (Z_C) and β_L (β_C) are respectively the characteristic impedance and phase constant of the inductive (capacitive), or narrow (wide), transmission line sections.

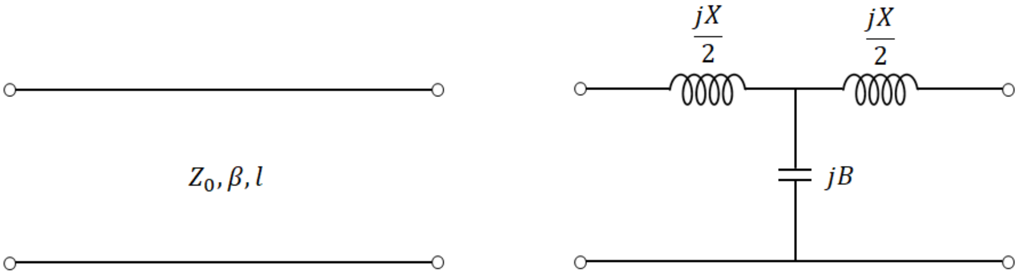

Figure 2-18: Transmission line and equivalent T-model.

Chapter 3

Design process

The design process starts with the Fabry-Pérot resonator. This defines the output of the MKID and therefore the signal which will eventually be measured. A schematic view of the FP is shown in Figure 3-1. The design of the FP is based on the design of K. Kouwenhoven in [10] and will therefore roughly follow the same design steps. The next part of the process is the design the filter, which depends on the coupler transmission characteristics. Several design choices need to be made for the filter implementation: lumped versus distributed elements, filter function (Butterworth versus Chebyshev), and the values of the cut-off frequency f_c, stop-band frequency f_s and stop-band attenuation A_s. The final part of the design is to study the placement of the filters on the FP and the effect of a bias current on both. These design steps will be discussed in the following sections, but first some broader system requirements and limits are discussed.

Since the measurements of this design will be measured with a similar set-up to the one in [10], it is beneficial to take the system limitations into consideration for this design. In this case there are two limitations. The first of these is the spurious noise floor of roughly -30 dB. Any signal below this level is irretrievable. The second is the frequency resolution of 10 MHz of the continuous-wave THz photo-mixing source (Toptica Terabeam 1550) used to probe the FP. This places a lower limit on the spectral resolution of the output peaks which can be translated into an upper limit on the Q_l. There are some further requirements for the design which need to be specified. The first being that the signals of interest, for which the FP and the filter should be optimized, are in the $300 - 400$ GHz range. The materials which are used for the design are the same as used in [10]. The relevant properties of these materials are given in Table 3-1. The T_c and ρ are known and with these the thickness t of the superconductors and their respective L_k are derived using Equation 2-9, Equation 2-10 and Equation 2-11. Since the materials are the same, the values of Q_i and Q_l in [10] can be used for this design as well. From the measurements in [51] and [52], the value of Q_i was found to average around 3500 and the value of Q_l, for two different values of a Q_c, was found to be 1500 and 2500.

Table 3-1: Material characteristics

Superconductor					
	Material	T_c [K]	ρ [Ωm]	t [nm]	L_s [pH/sq]
FP and filter	NbTiN	14.3	90×10^{-8}	92	1.009
Ground plane	NbTiN	15	100×10^{-8}	107	0.926
Dielectric					
	Material	ε_r	t [nm]		
	a-Si	10	300		

3-1 Fabry-Pérot

Given the previously mentioned system limitation it is important to design the FP in such a way that the complete transmission is above the spurious noise floor. In order to be able to quantify the effect of a bias current on the frequency behavior of the FP the number of peaks visible in the $300 - 400$ GHz range is also paramount. If this number is too low, their shape can be affected by possible fabrication tolerances in the coupler. If the number of peaks is too high it becomes difficult to track the effect of the bias current on them. The design of the FP, given the constraints on the minimum transmission level and the number of visible peaks, is a delicate balance of the three Q-factors.

The schematic overview of the FP is shown in Figure 3-1. The gray metal layer contains the CPW line from the antenna on one side, the KID on the other side and the ground plane beneath the FP. The yellow area is the a-Si dielectric. The turqoise line is the FP resonator. The length of the FP l_{FP} and the length of the couplers l_{coup}, which are identical, are the only two dimensions which can be altered to obtain the desired output. The width of the coupler is 4 μm and was specifically designed in [10] to obtain optimal coupling from the $2-2-2$ μm CPW line and for it to be robust against possible misalignment during fabrication. The width of the FP is equal to 2 μm.

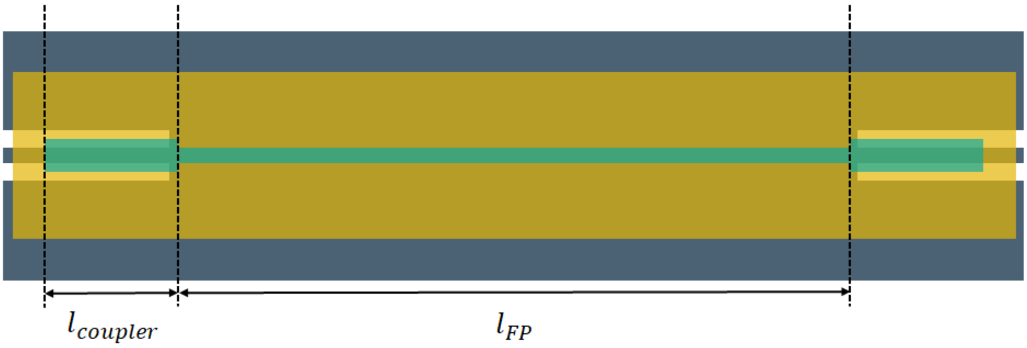

Figure 3-1: Schematic of microstrip Fabry-Pérot resonator. The ground plane NbTiN is grey, the a-Si dielectric is yellow and the FP resonator is turqoise.

As mentioned above, l_{FP} and l_{coup} are used to define the FP transmission. The latter directly affects the transmission through the couplers $|S_{21c}|^2$, as (Equation 2-31)

$$Q_c = \frac{\pi n}{|S_{21c}|^2}, \tag{3-1}$$

which is used to satisfy the requirement concerning the spurious noise floor. This effect is shown in Figure 3-2a [10]. The values of $|S_{21c}|$ and Q_c also set the requirements for the filters. The low-pass filters for the injection of the dc currents should not load the FP, which can be written as

$$\begin{gathered} |S_{21c}| \gg |S_{21filt}| \\ Q_c \ll Q_{c,filt} \end{gathered} \tag{3-2}$$

Changing l_{FP} has a direct effect on the fundamental resonant frequency and therefore the mode number n (related by Equation 2-24) as

$$f_0 = \frac{c_0}{2l_{FP}\sqrt{\varepsilon_{eff}}}. \tag{3-3}$$

This effect is shown in Figure 3-2b. Changing n however, also leads to a change in Q_c. Therefore, the determination of Q_c requires a trade-off. On one hand, if Q_c is small (high coupling strength $|S_{21,c}|$), the minimal FP transmission level increases and the peak height does so as well according to

$$|S_{21,max}| = \frac{Q_l}{Q_c}, \tag{3-4}$$

as can be seen from Figure 3-2a. On the other hand, if Q_c is large, the requirement on the filter rejection is alleviated. Also, if Q_c is large in comparison to Q_i, the design becomes robust against fabrication errors in the coupler and the Q_i can be directly estimated from Q_l using Equation 2-29.

When designing the FP it is important to keep in mind that l_{FP} is long enough for two low-pass filters to be placed sufficiently far apart to reduce any coupling between them. On the other hand, the length of the line should not be too long to be able to fabricate without faults.

3-1-1 Fabry-Pérot length

To derive L_{FP}, a set of realistic values of $|S_{21c}|^2$ is used to calculate the Q_c of the couplers using Equation 3-1. This Q_c is representative for the FP with two couplers in the fundamental mode, $n = 1$. Using the design values of Q_l and the measured Q_i value from [10] the corresponding coupling quality factor of the overmoded FP Q_c is calculated by

$$Q_c = \frac{Q_i Q_l}{Q_i - Q_l}. \tag{3-5}$$

The mode number n of a FP with a particular Q_l and Q_i can be calculated by relating the coupling quality factors of the FP (Q_c) with the one of the isolated coupler ($Q_c(n = 1)$)) as

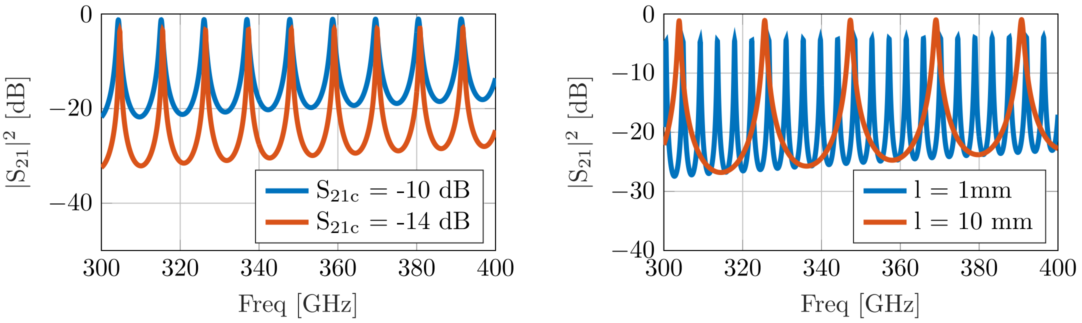

(a) $l_{FP} = 2$ mm **(b)** $|S_{21c}|^2 = -12$ dB

Figure 3-2: Effect of l_{FP} and effect of $|S_{21c}|^2$ on FP output. Adapted from [10].

$$n = \frac{Q_c}{Q_c(n=1)}. \tag{3-6}$$

The mode number immediately leads to the fundamental resonant frequency f_0

$$f_0 = \frac{f_n}{n}, \tag{3-7}$$

where f_n is equal to 350 GHz, the central frequency in the band of interest. Finally, the length of the resonator is obtained using Equation 3-3 as

$$l_{FP} = \frac{c_0}{2f_0\sqrt{\varepsilon_{eff}}}. \tag{3-8}$$

Table 3-2 shows the design values for a FP with $Q_l = 2500$ and $Q_i = 3500$ and different values of S_{21c}. This shows that, for a fixed Q_l, the larger the transmission through the couplers, the more visible peaks n_{vis} in the frequency range of 300 to 400 GHz and the longer the FP becomes. The design with $S_{21c} = -12$ dB was chosen since there are many visible peaks and the entire curve is above the spurious noise floor of -30 dB. The response of this configuration is plotted in Figure 3-3.

Table 3-2: Calculated values for an FP with $Q_i = 3500$ and $Q_l = 2500$ at 350 GHz.

$\|S_{21c}\|^2$ [dB]	Q_c	$Q_{c,FP}$	f_0 [GHz]	n_{vis}	l_{FP} [mm]
-14	78.9	8750	3.1565	31	6.9048
-13	62.7	8750	2.5073	39	8.6926
-12	49.8	8750	1.9916	50	10.943
-11	39.6	8750	1.582	63	13.777
-10	31.4	8750	1.2566	79	17.344

3-1-2 Coupler

A close-up of the coupler from Figure 3-1 is shown in Figure 3-4. The transmission through the coupler depends on how far the coupler extends over the CPW line. This overlap is

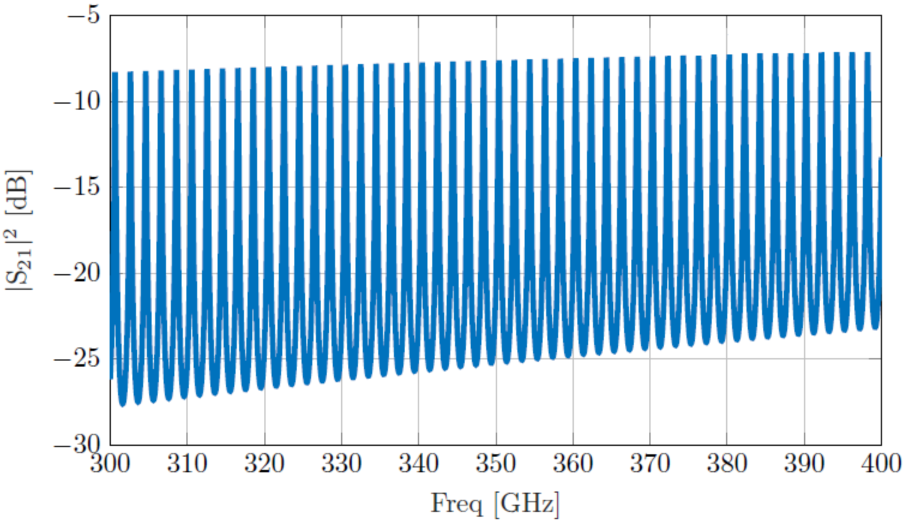

Figure 3-3: Transmission through FP with a coupler transmission of $|S_{21c}|^2 = -12$ dB from Table 3-2 for $Q_i = 3500$ and $Q_l = 2500$ at 350 GHz.

called l_{over}. A small redundancy in the coupler length is added since slight misalignment is common during fabrication. This extension of the coupler l_{red} is equal to 1 μm. Both lengths added together form l_{coup}. In Figure 3-5 a plot of the transmission through the coupler w.r.t. varying l_{over} is shown. This was simulated in Sonnet. The transmission increases almost logarithmically with longer values of l_{coup}. From this plot, the value of l_{over} corresponding to the FP transmission in Figure 3-3 is equal to 14.5 μm.

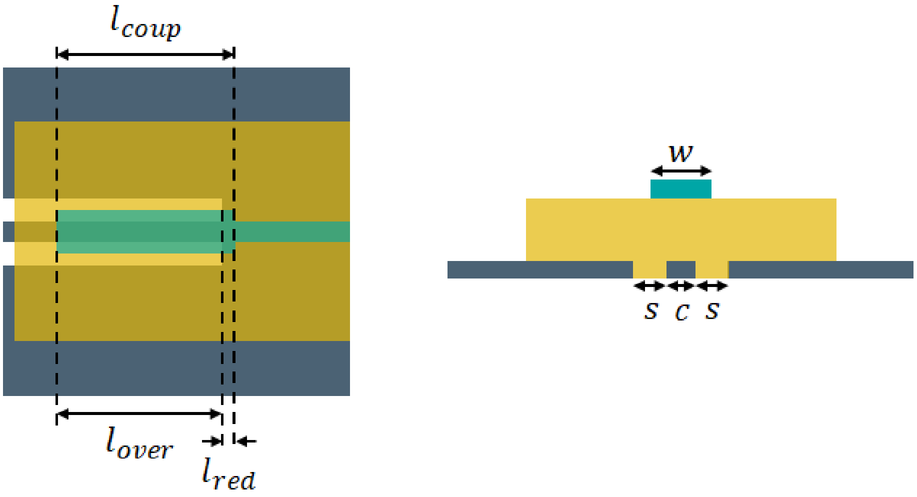

Figure 3-4: Close-up of the microstrip coupling capacitor and its cross section.

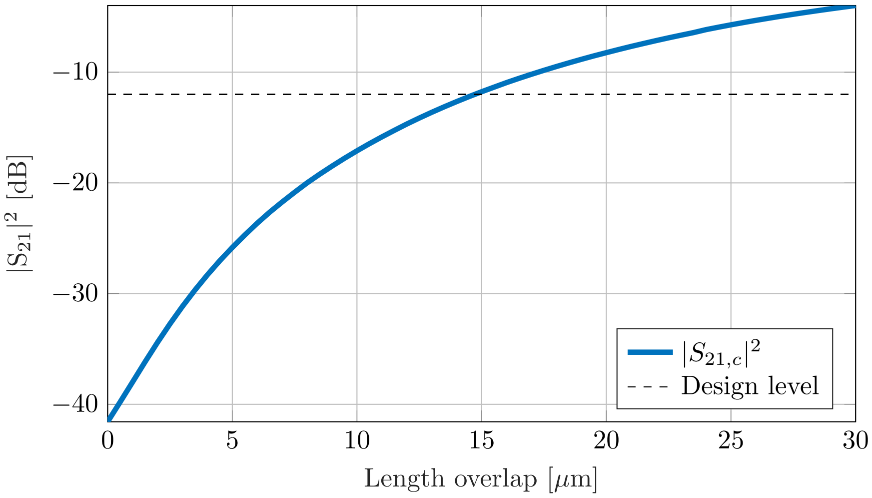

Figure 3-5: Simulated coupler overlap length l_{over} versus transmission.

3-2 Low-pass filter

As mentioned in the previous section, one requirement of the low-pass filter is based on the transmission through the couplers of the FP. The transmission of the high-frequency ($300-400$ GHz) signal through the filter should be at least 10 dB lower than the transmission through the coupling capacitors. Another aim of the filter design is its attachment to the FP, without bias currents, should ideally have little to no effect on the location of the resonant frequencies as well as the shape of the peaks. In reality however, the filter will load the FP, causing a change in the loaded quality factor and the location of the resonances in the response.

A low-pass filter can be constructed using lumped elements or electrically small transmission lines sections (distributed elements) and can be realized using different filter functions: Butterworth and Chebyshev. These choices and their implementation are discussed in the following sections.

3-2-1 Filter construction

In this section lumped components are compared to distributed components. In general, filters constructed of either lumped- or distributed elements have very similar pass-band characteristics. They both have different downsides. The lumped-element components are more difficult to fabricate and due to their intricate design, introduce many parasitic effects. The distributed elements on the other hand, are narrow band since their size should be comparable to the wavelength. It is also possible that a distributed-element filter has more pass-bands at higher frequencies. This response however, will not be periodic unless the filter sections are commensurate [43].

Lumped-element filter

The simplest form of a low-pass filter for this design is a series inductor since its impedance increases with frequency ($Z_L = j\omega L$). The implementation of a series inductor using microstrip technology looks like Figure 3-1. The planar spiral can be patterned on the same level as the ground plane of the microstrip. A via in the center of the spiral is required to connect the spiral to the FP, in the microstrip layer. The inductance of a square planar inductor can be approximated through [53]

$$L = L_{self} + M_{pos} - M_{neg} \tag{3-9}$$

where L_{self} is the self-inductance of the strip, M_{pos} the positive mutual coupling and M_{neg} the negative mutual coupling. The positive mutual coupling comes from the parallel segments in which the current flows in the same direction. The negative mutual coupling arises from the coupling between perpendicular sections. The inductance increases with the number of turns, conductor width, conductor spacing and the size of the gap between the innermost conductors [53].

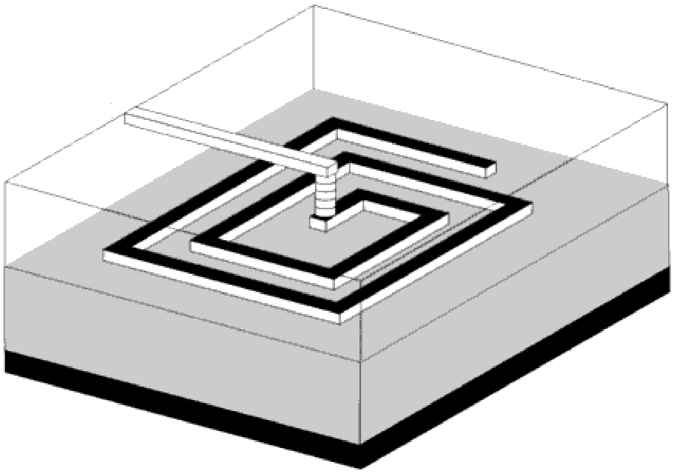

Figure 3-6: Planar inductor diagram from [54]

Using Equation 3-9, the ideal transmission of the high-frequency signal through the planar inductor is plotted in Figure 3-7a and Figure 3-7b for different combinations of number of turns N and line widths w. The same planar inductors are also simulated using Sonnet, the results are plotted in Figure 3-7c and Figure 3-7d. Using the equation for a series inductor, $j\omega L$, the transmission through the inductors is calculated. The transmission is not low enough, but it steadily decreases with frequency. The simulations show a completely different picture. It shows the negative impact of the coupling and parasitic effects of the inductor sections on the transmission. The only inductor which does not resonate everywhere has a conductor width of 0.1 μm, which is very difficult to fabricate. The lumped-element inductor therefore cannot be made electrically small enough to operate well at these frequencies. Since a single series inductor already has this kind of resonant behavior, the use of a ladder network containing shunt capacitances and more planar inductors will not be investigated and lumped-element components will not be used for this design.

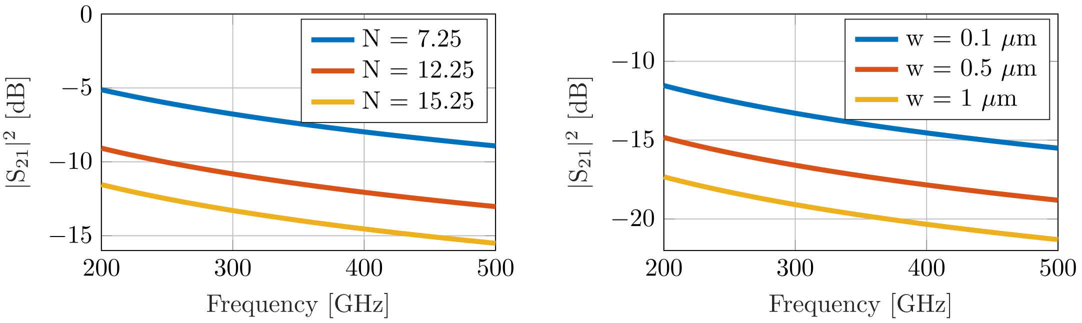

(a) $w = 0.5\mu m$ **(b)** $N = 7.25$

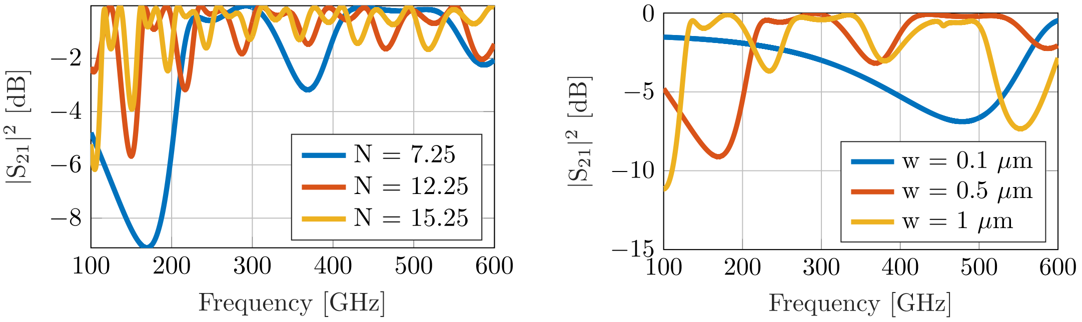

(c) $w = 0.5\mu m$ **(d)** $N = 7.25$

Figure 3-7: Ideal calculation and Sonnet simulation of square planar inductor with varying amount of turns N and line width w.

Distributed-element filter

In a distributed-element filter, electrically short transmission line sections are used to synthesize a cascade of series inductors and shunt capacitors. The cut-off frequency of the filter and the characteristic impedance of the the source/load Z_0, inductive section Z_L and capacitive section Z_C determine how well inductors and capacitors are approximated as well as their values. The distributed elements are narrow-band since their electrical phase has to be smaller than $\pi/4$ to approximate the behavior well. This can be calculated through Equation 2-67 and Equation 2-68, repeated below.

$$l_L = \frac{g_n Z_0}{Z_L \beta_L} \tag{3-10}$$

$$l_C = \frac{g_n Z_C}{Z_0 \beta_C} \tag{3-11}$$

Therefore, the range of characteristic impedances, $Z_C < Z_0 < Z_L$, is of importance and the behavior is improved as these lie further apart. Since the materials and their thicknesses are already defined, the width w of the sections is the only parameter which can change the characteristic impedances. This is the starting point of the filter design.

It is assumed that the filter is terminated on both sides with the characteristic impedance of the FP line Z_0. This value sets a lower limit for the impedance of the inductive section and an upper limit for the impedance of the capacitive section. As mentioned in subsection 2-4-2 the width for the inductive section is limited by fabrication constraints and current density requirements. Within the group it is possible to reliably pattern lines as narrow as 450 nm [47]. The width of the inductive section is chosen to be 0.5 μm. The largest limitation for the width of the capacitive section is extraneous resonances. The width should also not be too wide to create coupling between the capacitive sections. The width of the capacitive section was therefore chosen to be 10 μm. Table 3-3 compiles the characteristic impedance $Z_{L,C}$ and effective permittivity ε_{eff} of the different line sections that are obtained with Sonnet.

Since it is already decided to use distributed elements for the filter, simulations demonstrating their performance are presented in the following section when the choice between the filter functions is made.

Table 3-3: Simulated impedance and effective permittivity values for microstrips simulated with Sonnet at 350 GHz.

	w [μm]	L_k [pH/sq]	Z_0 [Ω]	ε_{eff} [-]
Inductive section	0.5	1	108.0	50.0
Capacitive section	10	1	8.0	53.2
Fabry-Pérot	2	1	34.3	47.3
CPW lines	2-2-2	0.925	80.1	15.4

3-2-2 Filter function

In subsection 2-4-1 two different filter functions were discussed: Butterworth and Chebyshev. They differ in behavior in their pass- and transition-band response. For the Butterworth the pass-band response is maximally flat while the Chebyshev response has a ripple with a constant amplitude. This ripple gives the Chebyshev a higher roll-off rate in the transition band in comparison to the Butterworth response. Their individual ideal responses are plotted in Figure 3-8 for a cut-off f_c frequency of 250 GHz, a stop-band f_s frequency of 500 GHz and a stop-band attenuation A_s of 50 dB. For the Chebyshev filter the magnitude of the ripple also needs to be defined, which in this case is set to 3 dB. The behavior in the pass-band does not weigh too heavy for this application since only a dc signal will be sent through. The ripple of the Chebyshev therefore is no problem and its faster roll-off rate already gives it an advantage over the Butterworth function. At least in the ideal case.

In order to compare the actual performance of the two filter functions, both are simulated for a set of f_c and f_s. Both filters are designed to start with an inductive section so that the connection area between the FP and the filter will be as small as possible and free from spurious coupling. Equation 2-44 is used to calculate the order of the Butterworth filter and Equation 2-50 to calculate the impedance and frequency normalized values of its sections. The Chebyshev filter requires Equation 2-55 to be used for its order and Equation 2-67 and Equation 2-68 for the impedance and frequency normalized values of its sections. The simulated impedance and effective permittivity of Table 3-3 are used as well in Equation 2-67 and Equation 2-68 to find the lengths of the individual sections of both filters. For comparative purposes, Appendix C shows tables with the segment lengths for both filters for all the following simulations.

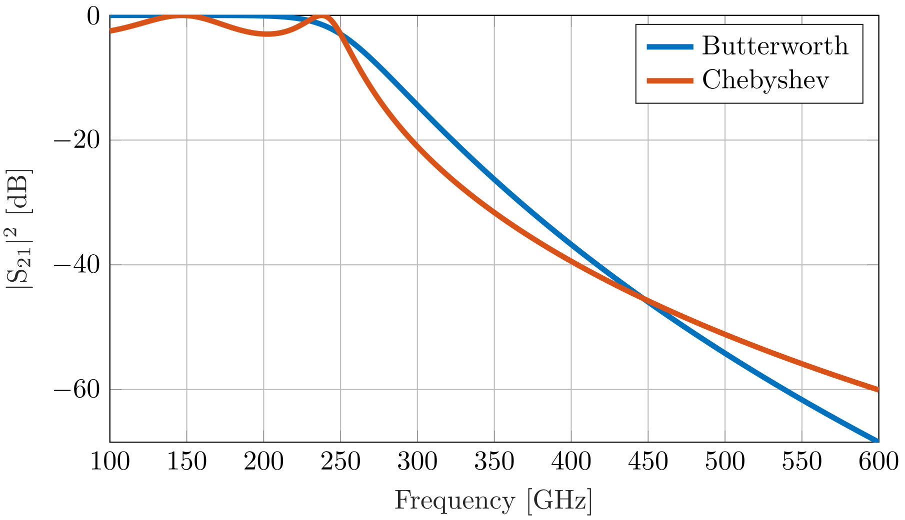

Figure 3-8: Ideal behavior of Butterworth and Chebyshev filters. The cut-off frequency for both is placed at 250 GHz and a minimum attenuation of 50 dB is required at 500 GHz. The ripple for the Chebyshev filter is 3 dB which is quite exaggerated.

Effect of cut-off and stop-band frequencies

The frequency selectivity of both filters is studied fist. Using the $S_{21,c} = -12$ dB criterion, it is implied that the $S_{21,f}$ must be at least -22 dB. From simulations it was observed that this level of transmission could easily be obtained with the stepped-impedance filter. Therefore, to create a buffer, a stop-band attenuation of 50 dB is implemented in the following designs. In Figure 3-9a and Figure 3-9b the transmission of the Butterworth and Chebyshev filters are studied for three different combinations of f_c and f_s. The value of f_s in all cases is 300 GHz and the values of f_c are 175 GHz, 150 GHz and 100 GHz. The filter order and individual section lengths can be found in Appendix C (Table C-1, Table C-2 and Table C-3).

From Figure 3-9 it is immediately visible that the theoretical slope shown in Figure 3-8 is not obtained, but it performs much better than the lumped element filter implementation of Figure 3-7. From these simulation results, a condition for f_c and f_c in order to attain the stop-band attenuation, namely $f_s \leq 2f_c$. For the two simulations in which this criteria is met, for both Butterworth and Chebyshev, there is some sort of resonance occurring around 440 GHz. After this their transmission increases which is due to the electric length of the sections becoming too large in comparison to the wavelength. From these results the faster roll-off rate of the Chebyshev filter can also be observed. In Figure 3-10 different combinations of $f_s = 2f_c$ are used where f_c is equal to 75 GHz, 100 GHz and 175 GHz. The section lengths can again be found in Appendix C (Table C-3, Table C-4 and Table C-5).

From this second round of simulations it is clear that the stop-band frequency f_s cannot be chosen arbitrarily. If f_s is too low, the frequency band on interest is cluttered with spurious resonances. If f_s is too high, the frequency band of interest will lie in the pass-band or not yet have reached a satisfactory amount of attenuation.

From the fact that the Chebyshev filter has a steeper roll-off rate and the fact that it requires a smaller filter order than the Butterworth filter in each case, the Chebyshev filter will be

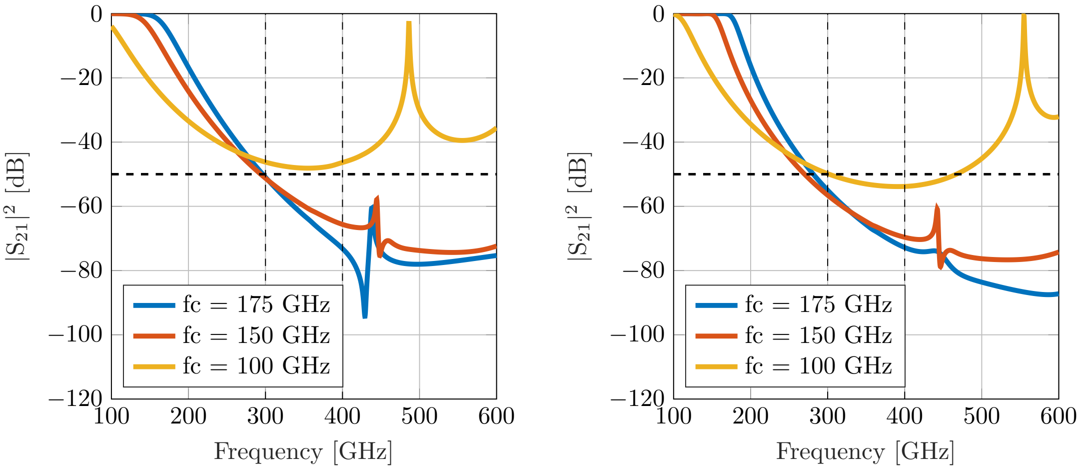

(a) Butterworth **(b)** Chebyshev

Figure 3-9: Sonnet simulations Butterworth and Chebyshev filters with $f_s = 300$ GHz, $A_s = 50$ dB and a ripple of 0.01 dB for different f_c.

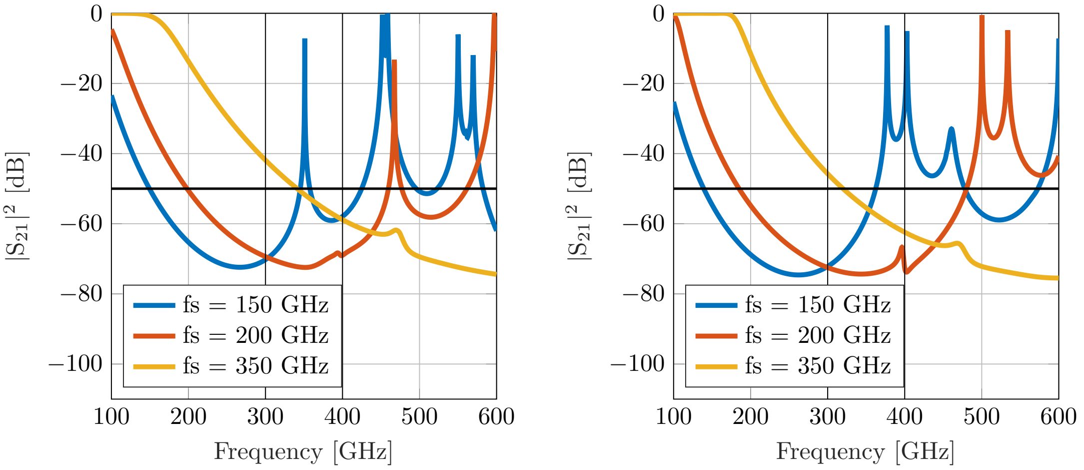

(a) Butterworth **(b)** Chebyshev

Figure 3-10: Sonnet simulations Butterworth and Chebyshev filters with $f_c = f_s/2$ GHz, $A_s = 50$ dB and a ripple of 0.01 dB.

implemented in this design. More specifically, a Chebyshev filter with $f_c = 175$ GHz, and $f_c = 300$ GHz and $A_s = 50$ dB. Now that the Chebyshev filter is chosen, the effect of its ripple and the effect of unmatched filter terminations are briefly discussed as well.

Effect of ripple

The results of three simulations, performed on the above mentioned Chebyshev filter, with different values of ripple magnitude ε is shown in Figure 3-11. For these simulations as well, the filter order and individual segment lengths can be found in Appendix C (Table C-1, Table C-7 and Table C-8). Even though an increase in ripple requires a lower filter order for the design, the roll-off rate in the transition-band decreases and the maximum attenuation decreases as well. For this reason the Chebyshev filter will be implemented with a ripple magnitude of 0.01 dB.

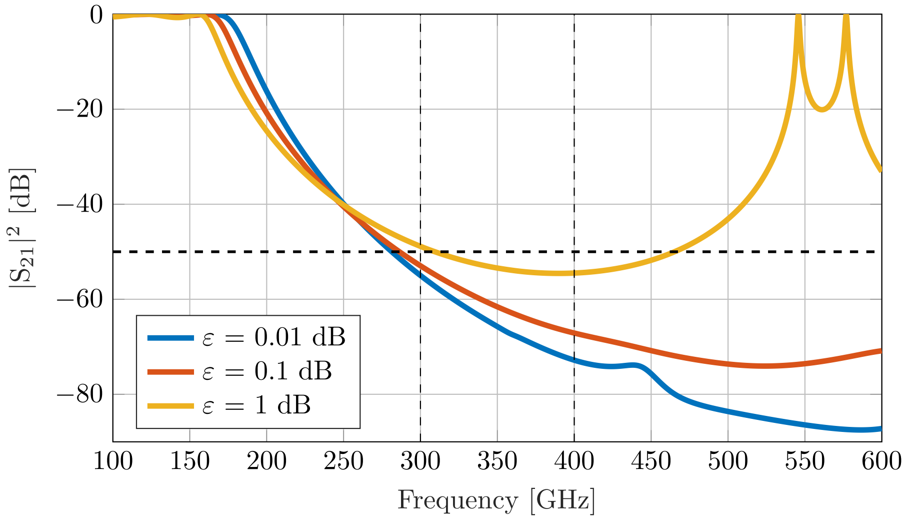

Figure 3-11: Effect of ripple on Chebyshev filter transmission. In this case, $f_c = 175$ GHz, $f_s = 300$ GHz and $A_s = 50$ dB.

Effect of unmatched terminations

The Chebyshev filter is designed to be terminated on both sides with the impedance of the FP, 34.3 Ω. These impedances can vary as a result of fabrication tolerances and due to the uncertainty in the actual loading posed by both the FP and the dc lines on the filter. It is therefore useful to know how the filter transfer changes if these impedances are not identical or have different values. This is studied in Figure 3-12. The filter transfer function is simulated for the termination of the FP impedance on one side, and different termination impedances on the other side. The black line represents the matched case. The other cases represent different loading values of the dc line at THz frequencies, varying from impedances lower than Z_C to higher than Z_L. There is no large impact visible unless the impedance of the bias lines is very low. In that case the pass-band attenuation is non-zero. The variation in termination impedance is therefore not a problem.

3-3 System design

The filter has been designed with an extremely high rejection ($|S_{21}|^2 < -50$ dB) for the frequencies between 300 and 400 GHz so that the transmission of these frequencies through the FP will be almost unaffected. In order to avoid the degradation of this rejection level, the placement of both filters along the FP is optimized. After this, the effect of the bias current and sensitivity of the FP to the bias current will be studied.

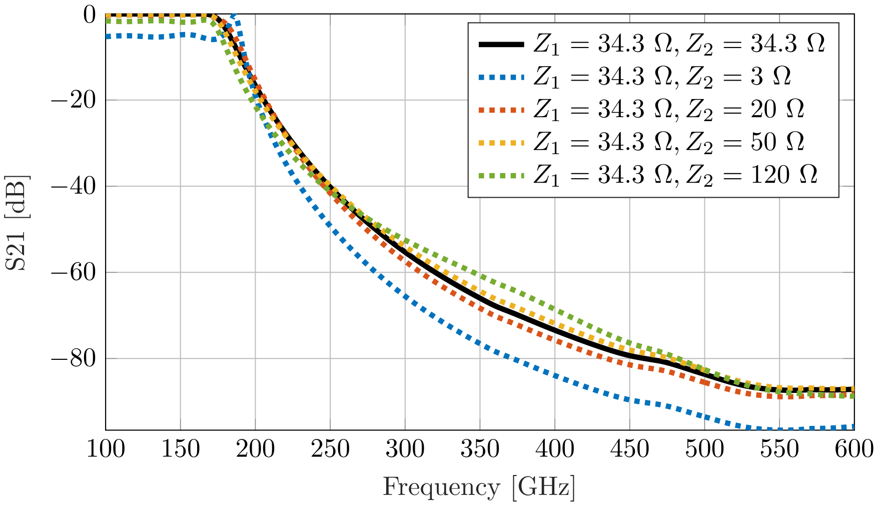

Figure 3-12: Effect of changing the load at one side of the filter. The black line represents the filter transfer for the ideal terminations ($34.3\ \Omega$).

3-3-1 Filter location

As discussed in subsection 2-3-1, the FP has many voltage and current nodes depending on n. Different from what is shown in Figure 2-8, realistically the impedance at the current and voltage nodes will not tend to zero and infinity, but just differ slightly from each other. The filter by itself has a large input impedance for high frequencies. If the filter is connected to a current node, the filter impedance might be less or close to that of the FP, therefore reducing the rejection of the filter. If the filter is connected at a voltage node, its impedance will be larger than that of the FP which preserves its rejection of the high frequency signals.

Another issue for the placement of the filters is that the couplers affect the standing wave patterns around them. This is one of the reasons for having a large number of visible peaks between 300 and 400 GHz. With the following simulations, the placement of the filter is optimized, keeping in mind the location of the voltage nodes (low-impedance points). In Figure 3-13 the simulations of the current distribution for four different modes is presented. For these simulations the length of the FP was varied, the coupler length remained the same 15.5 μm, to accommodate a different number of modes each time. It was not possible to simulate the entire length of the FP, 10.943 mm, due to the size of the simulation; however these simulations are still meaningful to quantify the effect on the FP transmission in the presence of the designed shunted low-pass filters. The dashed black lines in each simulation indicate the end of the coupler and the 1 μm extension (l_{red}) of the coupler. It is obvious that the coupler has a large effect on the current distribution. Looking at the values of the current distribution on the coupler, it is wise not to attach the filters on the couplers but rather on the FP, where the current reaches its maxima, and thus the impedance minima. Furthermore, the transmission through the FP couplers can be disturbed if the filters are directly connected there. In Table 3-4 the locations of the current nodes (minima) and voltage nodes (current maxima) are shown for the four simulations. These distances are measured from the outer edges of the coupler, that is including the complete coupler length ($l_{over} + l_{red}$) as shown in Figure 3-14. These lengths are similar for each mode number. Possible coupling between the filter elements and the coupler or between the two filters should be studied as well in simulations to find the optimal filter location.

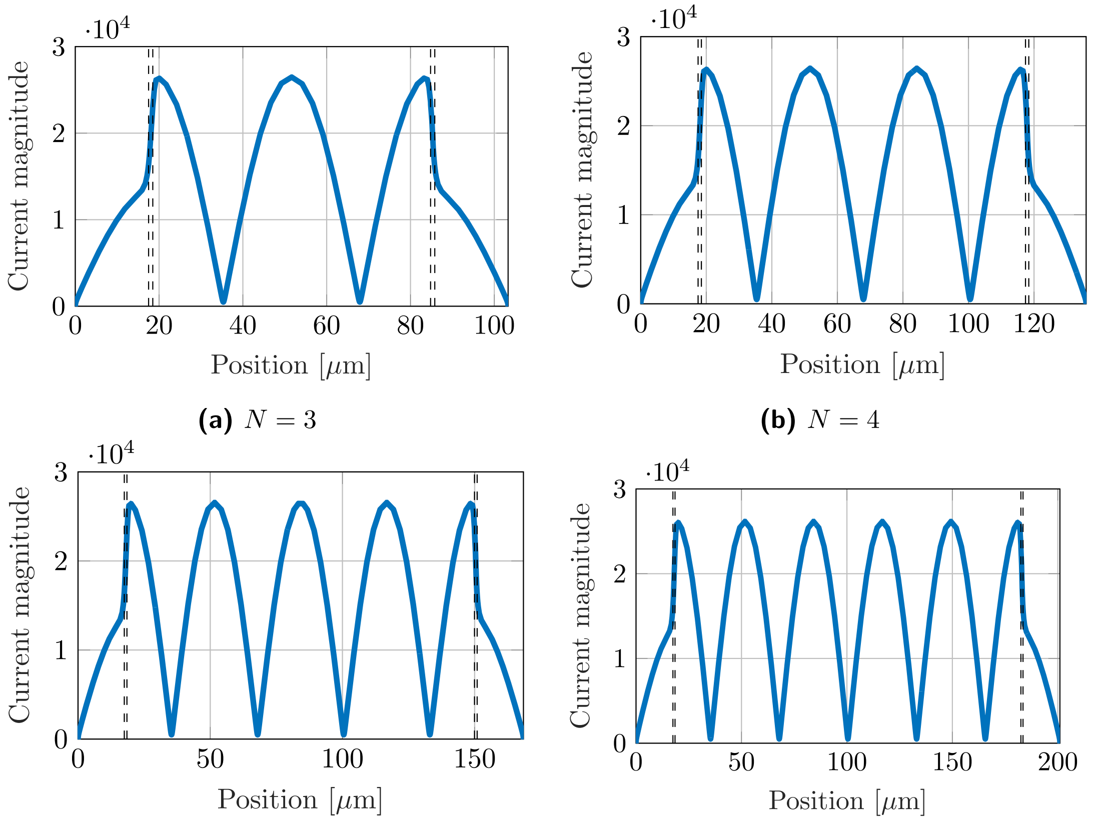

(a) $N = 3$ **(b)** $N = 4$

(c) $N = 5$ **(d)** $N = 6$

Figure 3-13: Simulation of current distribution on FP for different amount of modes. This simulation is used to determine the optimal locations for the filters.

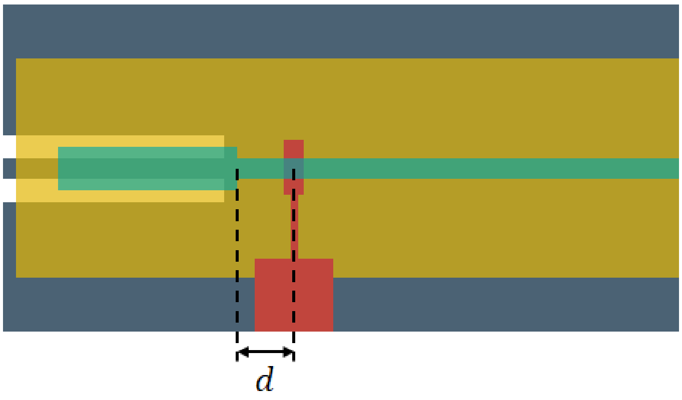

Figure 3-14: Filter placement. The length between the coupler and the center of the filter is used in Table 3-4.

Table 3-4: Locations of current maxima and minima, measured from the inner side of the coupler as shown in Figure 3-14.

Maxima (Voltage nodes)							
Mode	Length [μm]	Max 1	Max 2	Max 3	Max 4	Max 5	Max 6
2	85.1	10.68	74.42				
3	146.9	10.68	73.45	136.22			
4	208.85	10.66	73.16	135.62	198.15		
5	270.75	10.83	73.33	135.40	197.47	259.97	
6	332.4	10.68	73.18	135.67	196.73	259.22	321.72
Minima (Current nodes)							
Mode	Length [μm]	Min 1	Min 2	Min 3	Min 4	Min 5	
2	85.1	42.55					
3	146.9	42.55	104.36				
4	208.85	42.58	104.40	166.22			
5	270.75	42.66	104.50	166.31	228.14		
6	332.4	42.56	104.38	166.20	228.02	289.84	

To test the statement made above about the effect of the placement of the filter, simulations were performed with the filter attached in three different locations with respect to the coupler, namely on the first voltage node and current node and the second voltage node. A schematic of this design is given in Figure 3-15. The port numbers are the same as in the simulations whose results are plotted in Figure 3-16. In these simulations the gray line represents the transmission through the FP without any filter, S_{21} is the transmission through the FP, S_{31} the transmission between one coupler and the closest filter and S_{41} the transmission between one coupler and the furthest filter.

In all cases the resonance peak is shifted to higher frequencies with respect to the resonance peak of the FP without filters (which is at 350 GHz). The amount by which it is shifted can be found in Table 3-5. This shift is because of the reactive loading of the FP by the filter. This is probably indirect coupling due to parasitic effects between the filter and the coupler. It can also be due to the fact that the filter itself is not ideal. The effect of the reactive loading seems to decrease as the filter is placed further away from the coupler, which indicates that there is quite some spurious coupling between the filter and the coupler. Another aspect to keep in mind is that these simulations are done for very short FPs (low mode numbers), but in the actual design the size of the FP is significantly larger than the filters. When looking at the rejection levels of the filter it is clear that the location of the filters does make a difference. When the filters are attached at the voltage nodes the rejection remains below 60 dB. When the filter is attached to the current node the shape of the rejection follows the resonance peak up to -43 dB. Therefore it is preferable to attach the filters at the voltage nodes. In Appendix C the current distribution on the FP and filters and ground plane corresponding to Figure 3-16 are shown.

Despite the shift in resonant frequency due to the loading of the FP by the filters and the smaller rejection if the filters are attached at current nodes, these effects are not detrimental to the functioning of the FP. This design is therefore robust against any misalignment of the filters during fabrication.

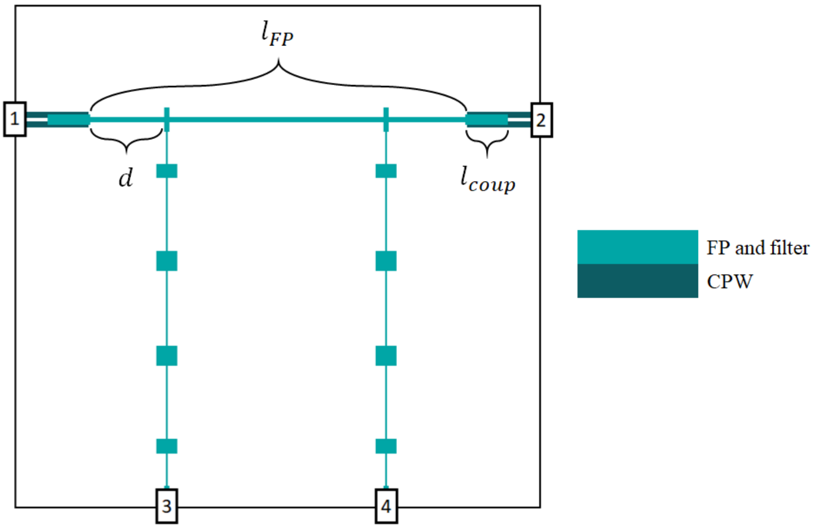

Figure 3-15: Schematic of the design of the FP with the filters attached. The port numbers are the same as will be used for the following simulations.

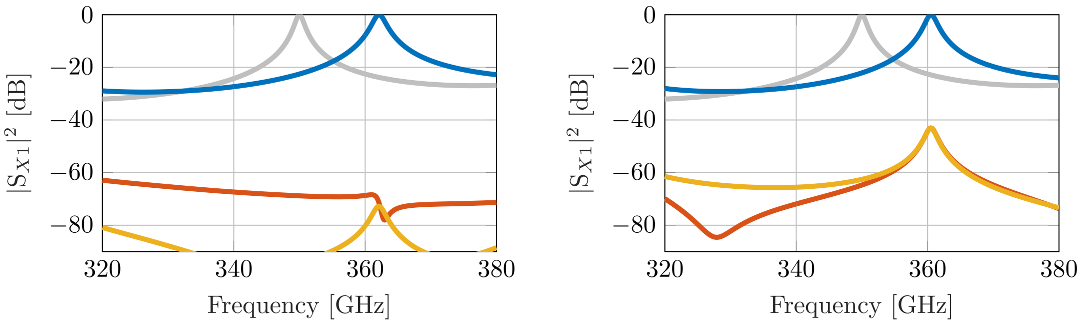

(a) First voltage node.

(b) First current node.

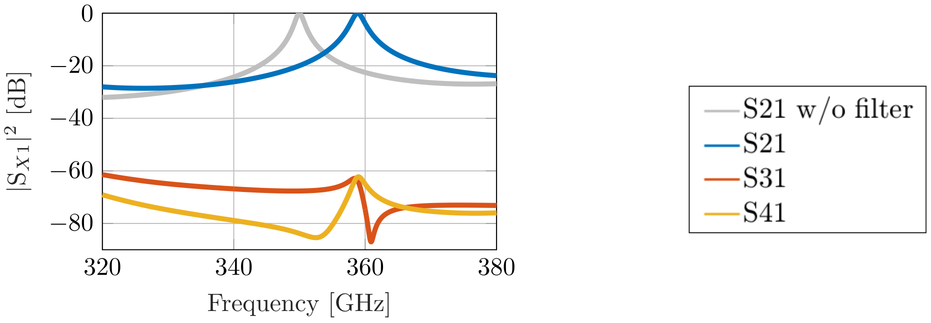

(c) Second voltage node.

(d) Legend

Figure 3-16: The effect of the filter (without bias current) on the transmission of the FP with $n = 6$ at 350 GHz. The grey line in each plot is the S21 for the FP without the filters attached. $S21$ is the transmission of the resonator, $S31$ the transmission between one coupler and the filter nearest to it and $S41$ is the transmission between one coupler and the filter furthest from it as shown in Figure 3-15.

Table 3-5: Resonance peak locations for different filter locations and their respective differences from the FP without filters, nominally designed to resonate at 350 GHz. The peak frequencies and difference between them were taken from Figure 3-16 from the S_{21} of the FP (blue line). The shift in frequency was taken with respect to the FP without any filters attached to it (gray line).

Filter location	Peak frequency [GHz]	Frequency shift [GHz]
1st voltage node	362.11	12.11
1st current node	360.52	10.52
2nd voltage node	358.86	8.86

3-3-2 Current considerations

Since the NbTiN layer of the FP and the filter have the same thickness, the critical current I_c in this design will be limited by the part which is the narrowest: the inductive filter sections. Using Equation 2-16 and Equation 2-19, I_c and I_* were calculated to be roughly twice as large as the values found in other studies. Therefore, to be on the safe side, these values are estimated by scaling the measured values of S. Shu [12], very similar to the values of T. Basu [13], for a 35 nm thick, 250 nm wide NbTiN microstrip to the dimensions of the inductive filter section. In [12] they found the value of I_c to be equal to 0.8 mA and the non-linearity scaling factor I_* to be equal to 3 mA. Both values are scaled to the dimensions of the FP and the inductive filter section used here through

$$I_{c,*} \approx I_{c,*:Shu} \left(\frac{t}{35 \text{ nm}}\right) \left(\frac{w}{250 \text{ nm}}\right). \tag{3-12}$$

The approximated values of I_c and I_* of the FP and the inductive filter section are given in Table 3-6. Since the current is limited by the inductive filter sections, the sensitivity of the FP to the current is limited as well. This is evident from the calculation for the change in L_k due to a bias current, Equation 2-14, repeated below

$$L_k(I) \approx L_k(0) \left[1 + \left(\frac{I}{I_*}\right)^2\right] \quad \text{for } I \ll I_*. \tag{3-13}$$

The equation only holds for currents well below the I_* and of course, for currents below I_c. Therefore, the change in L_k for the FP cannot be exploited to the maximum. The change in L_k in both the inductive filter section and the FP was simulated for currents up to 2 mA as is shown in Figure 3-17. For the maximum value of 2 mA, the change in kinetic inductance δL_k for the inductive filter section is 0.1% and for the FP it is 1.61%. In this design, the FP is not very sensitive to the bias current.

With the values of L_k after biasing with a current of 2 mA the filter and FP can individually be simulated to quantify the effect of the current on their transmission. The left panel of Figure 3-18 shows the simulation results of the transmission of the unbiased FPs of Figure 3-13. On the right, the same FP is bias with 2 mA, which coincides with the values of L_k given in Table 3-7. The increase of L_k causes a decrease in the resonant frequency as expected. This frequency shift however is very small compared to the FWHM of the resonance peak. The

Table 3-6: Critical current and non-linearity scaling factor of the FP and the filter. The values are derived from the measurements in [12] and scaled to the dimensions of this design using Equation 3-12.

	I_c [mA]	I_* [mA]
FP	16.8	63.1
Filter	4.2	15.8

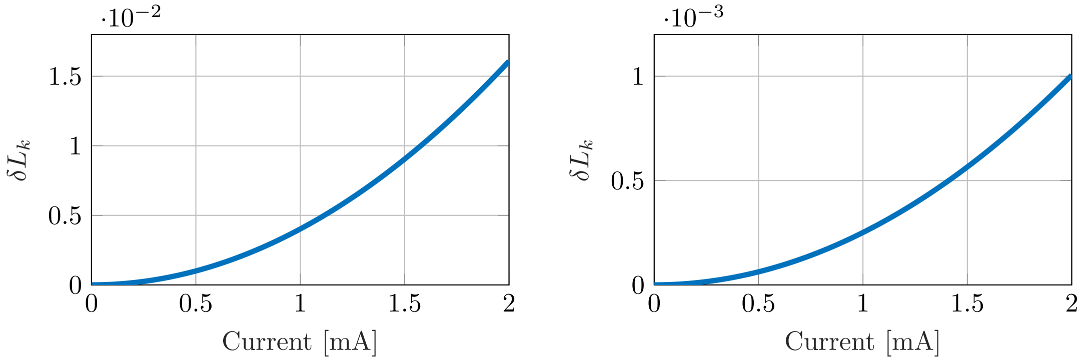

(a) Filter **(b)** FP

Figure 3-17: The relative change in kinetic inductance ($\delta L_k = (L_k(I) - L_k(0))/L_k(0)$) for the filter and the FP.

resonant frequencies for the unbiased and biased FPs and their difference with 350 GHz are shown in Table 3-8. Because the FWHM of a highly overmoded FP (high mode number n) is much narrower, the ratio of resonance shift to FWHM will be larger for the actual design. It will still however, be smaller than the FWHM.

Table 3-7: Values of L_k for the FP and filter without biasing and with bias with a dc current of 2 mA.

	Unbiased L_k [pH]	Biased L_k [pH]	ΔL_k [pH]
FP	11049	11060	11.1
Filter	181.6	184.5	2.92

The same simulations are done for the Chebyshev filter. In Figure 3-19 the filter is simulated to see the effect of the current. The values of L_k for this simulation are shown in Table 3-7 as well. From this simulation it is clear that the dc current biasing barely has any effect on the filter except at the resonant behavior around 440 GHz, which is outside of the bandwidth of interest.

The effect of the current on the FP together with the filter is shown in the Appendix C in Figure C-4. Here the transmission through the entire system, shown in Figure 3-16, is repeated next to the response of the entire system when biased at 2 mA. As was derived from the previous simulations, the effect of the current is minimal as the resonance peaks shift slightly to lower frequencies.

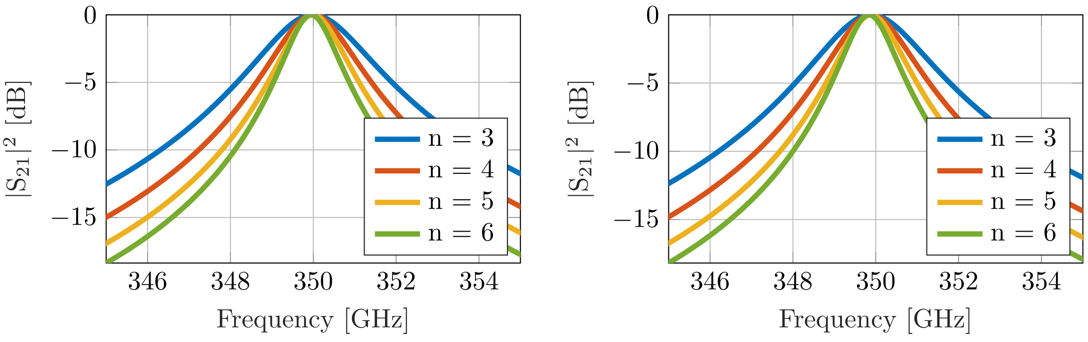

(a) Unbiased **(b)** Biased

Figure 3-18: Effect of current on a FP without filter. The level of current for the biased FPs is 2 mA.

Table 3-8: Resonance peak of Figure 3-18 for biased and unbiased FP and the frequency difference of their resonance peaks.

	f_0 Unbiased [GHz]	f_0 biased [GHz]	δf [GHz]
3rd mode	350	349.89	0.11
4th mode	350	349.89	0.11
5th mode	350	349.89	0.11
6th mode	349.95	349.84	0.11

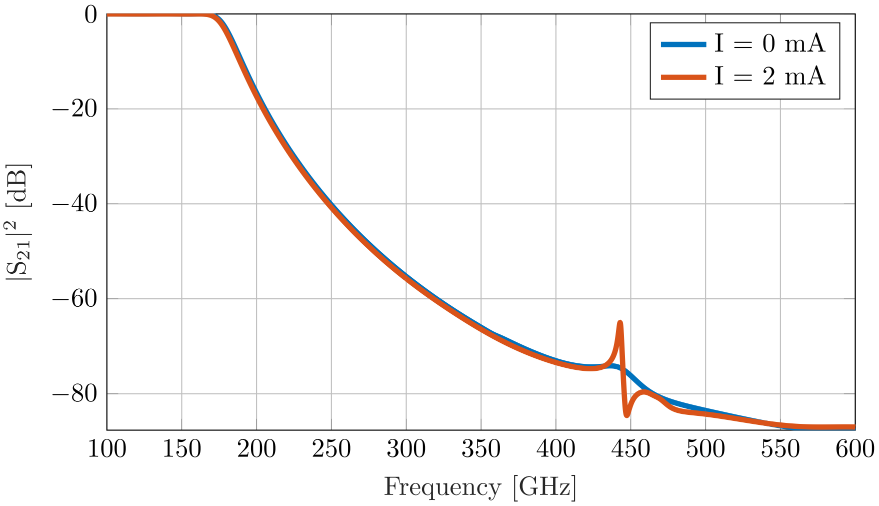

Figure 3-19: Effect of bias current on filter. The level of current for the biased filter is 2 mA.

3-4 Conclusion

In this chapter a Fabry-Pérot resonator and the shunted low-pass filters attached to it were designed. From all the simulations it was found that the designs are very robust against fabrication misalignments, filter termination mismatches, and filter positioning. Since it is possible to design the filter with an extremely high rejection, the transmission through the FP is barely unaffected. The only caveat of this design is the limited heat dissipation capability of the microstrip biased lines, thereby limiting the maximum allowable bias current and thus the range of tunability. The solutions to this are explained in the following chapter.

Chapter 4

Final chip design

There are two factors which limit the sensitivity to a dc bias current of the design discussed in chapter 3, namely the low unbiased kinetic inductance $L_k(0)$ of the Fabry-Pérot and the low critical current I_c due to the narrow width of the inductive filter sections. Both problems can be solved by making the FP thinner. Another possible issue with the design is heat dissipation. It is possible that heat will build up when the current is run through the filter and FP. Since a-Si has a lower thermal conductivity than Si it is beneficial to implement the FP and filters as inverted microstrips rather than regular microstrips. The difference between regular and inverted microstrips is shown in Figure E-3. The impact of these design changes will be discussed first. Since the design steps are exactly the same, only the important results will be examined in detail. Based on the new design, the measurement strategy is explained. This includes the design of the chip and all other aspects necessary for the measurements. Finally, the fabrication procedure is discussed.

4-1 Final design

The $L_k(0)$ of the FP can be increased by making the superconductor thinner (Equation 2-15). If the FP is made thin to such an extent that its cross-sectional area becomes smaller than that of the inductive filter section, I_*, and therefore I_c, become limited by the FP (Equation 2-19). In that case, the FP becomes the most sensitive part of the design to a dc biasing current. The important material properties, including those of the new thin layer for the FP, are shown in Table 4-1.

Changing the thickness of the FP as well as implementing the inverted microstrip structure have a significant impact on Z_0 and ε_{eff} of the filter sections and the FP. The new values of Z_0 and ε_{eff} are obtained from Sonnet simulations and are given in Table 4-3. With these new values the FP and filter are re-designed following the exact same steps as in chapter 3. For this reason, only simulations of the final results will be discussed in this section. All other simulations discussed in chapter 3 are shown in Appendix D for further comparison between the designs. For the simulations of the filter, the lengths of the filter sections can be found in Appendix C.

Table 4-1: Material characteristics for final design of inverted microstrip architecture.

Superconductor					
	Material	T_c [K]	ρ [Ωm]	t [nm]	L_s [pH/sq]
FP	NbTiN	14.3	90×10^{-8}	22	4.068
Filter	NbTiN	14.3	90×10^{-8}	92	1.009
Ground plane	NbTiN	15	100×10^{-8}	107	0.926

Dielectric			
	Material	ε_r	t [nm]
	a-Si	10	300

4-1-1 Fabry-Pérot

From Equation 2-22 and Equation 2-23 it is clear that any change in Z_0 and ε_{eff} affects both the FP and its coupling capacitors. If the same resonator output shown in Figure 3-3 is desired, the length of the FP and that of the coupler need to change. Performing the same calculations, the new FP lengths for different $|S_{21,c}|^2$ is given in Table 4-2. This shows that the l_{FP} is almost halved with respect to Table 3-2 for the same Q_c using $|S_{21c}|^2 = -12$. The new value of l_{coup} is again obtained through the Sonnet simulation shown in Figure D-1. This new value corresponding to $|S_{21,c}|^2 = -12$ dB is now equal to 17.5 μm, which leads to a total $l_{coup} = 18.5$ μm.

Table 4-2: Calculated values for an FP with $Q_i = 3500$ and $Q_l = 2500$ at 350 GHz.

$\|S_{21c}\|^2$ [dB]	Q_c	$Q_{c,FP}$	f_0 [GHz]	n_{vis}	l_{FP} [mm]
-14	78.9	8750	3.1565	31	3.6507
-13	62.7	8750	2.5073	39	4.596
-12	49.8	8750	1.9916	50	5.786
-11	39.6	8750	1.582	63	7.2842
-10	31.4	8750	1.2566	79	9.1702

4-1-2 Low-pass filter

The change in Z_0 and ε_{eff} of the inductive and capacitive filter sections, as well as the change in the Z_0 of the FP, also have a significant effect on the behavior of the filter. To compensate the change in Z_0 and ε_{eff}, the lengths of the filter sections need to change. A simple change in length in this case, however, does not lead to the same results as in subsection 3-2-2. This becomes visible when the simulations for both the Butterworth and Chebyshev filter functions are repeated. The results for the simulations with $f_s = 300$ GHz, $A_s = 50$ dB and a ripple of 0.01 dB for different f_c are shown in Figure D-2. The simulations with $f_c = f_s/2$ GHz, $A_s = 50$ dB and a ripple of 0.01 dB are found in Figure D-3.

From these plots it is clear that the changes in the design are not optimal for the behavior of the filters. The minimal rejection of 50 dB is not reached in most cases and there is a lot of resonant behavior in the stop-band, making the application of the filter more narrow-band.

Table 4-3: Simulated impedance and effective permittivity values for inverted microstrips simulated with Sonnet at 350 GHz. The values of the old design can be found in Table 3-3.

	w [μm]	L_k [pH/sq]	Z_0 [Ω]	ε_{eff} [-]
Inductive section	0.5	1	90.6	78.9
Capacitive section	10	1	6.6	59.5
Fabry-Pérot	2	4	52.8	169.2
CPW lines	2-2-2	0.925	88.6	12.6

One reason for this is that the range $Z_C < Z_0 < Z_L$ has changed: Z_0 is now much closer to Z_L. From Equation 2-67 and Equation 2-68 the dependence of l_L and l_c on this ratio is observed (Z_0/Z_L and Z_C/Z_0, respectively). Since the characteristic impedance of the FP is closer to Z_L and further away from Z_C with respect to the old design values, the l_L necessary to obtain the new inductance value becomes larger while the l_C becomes smaller. With the increase in ε_{eff} of the filter sections, the propagation constant $\beta = 2\pi/\lambda = 2\pi f\sqrt{\varepsilon_{eff}}/c$ increases as well. Both the increase in l_L and in β_L cause some of the inductive filter sections to become electrically too long, $\beta_L l_L > \pi/4$ rad, making these sections to approximate less an ideal inductor. This is denoted in the tables in Appendix C.

From these results, similar to the old design, the Chebyshev filter with $f_c = 175$ GHz, $f_s = 300$ GHz, $A_s = 50$ dB and a ripple of 0.01 dB performs the best. Its transfer function is plotted in Figure 4-1 together with the transfer of the old design. Despite the resonant behavior in the stop-band, a minimum rejection of roughly 40 dB should still be enough to not disturb the signal in the 300 to 400 GHz range.

The effect of the ripple on the filter and the effect of non-matching filter terminations are also simulated and shown in Figure D-4 and Figure D-5. The same conclusions as in subsection 3-2-2 can be drawn. Increasing the ripple of the Chebyshev filter lowers the rejection of the filter and brings the resonant behavior into the bandwidth of interest. The terminations do not have a large effect unless they become extremely low, lower than Z_C. In this case the rejection of the filter between 300 and 400 GHz improves, however the pass-band attenuation becomes non-zero.

4-1-3 System design

Due to the smaller l_{FP}, the location of the filters needs to be optimized again. With these in place, the new I_c of the system and the sensitivity of the FP to current need to be analyzed. This is what will be studied in the following two paragraphs.

Filter location

To find the location of the voltage and current nodes the current distribution over the resonator was simulated for different modes using Sonnet. These are plotted in Figure D-6 and the distance of the nodes with respect to the coupler are given in Table D-1. As before, the first voltage and current nodes and the second voltage node are of interest. A schematic of the new design is given in Figure 4-2. The response of the FP with the filters attached at

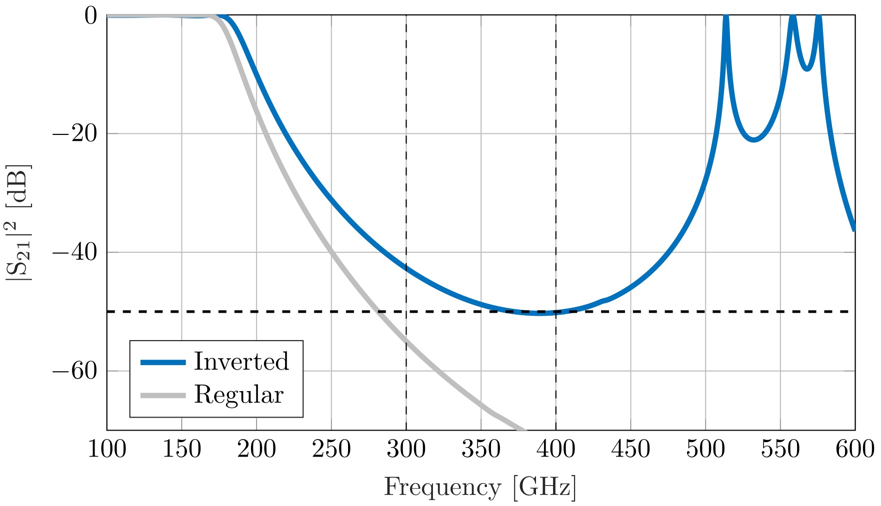

Figure 4-1: Chebyshev filter with $f_c = 175$ GHz, $f_s = 300$ GHz and $A_s = 50$ dB implemented with an inverted microstrip architecture.

these three locations in plotted in Figure 4-3, where the port numbers are the same as in Figure 4-2. Here the blue line represent the transmission of the FP, the red line the transmission between a coupler and its closest filter, the yellow line the transmission between a coupler and the filter furthest from it and the gray line the transmission of the FP without any filters attached.

The reactive loading from the filter, especially in the case of the first voltage node, shifts the resonance peak to higher frequencies. The frequency difference between the resonance peaks of the loaded FPs and the non-loaded FP, located at 350 GHz, is given in Table 4-4. For the filter located at the first voltage node this effect is so large that the resonance peak is moved out of the frequency range. This is probably due to coupling with the coupler. For the filters attached to the first current node and the second voltage node, the shift in resonant frequency is smaller than the first design. The current distribution on the FP and filters and ground plane corresponding to Figure 3-16 are shown in Figure D-7, Figure D-8 and Figure D-9. In Figure D-8, where the filter is located at the current node, the coupling of the 350 GHz signal into the filter is the largest; it is visible in the third inductive section. When the filter is located at the second voltage node the coupling is the least, making this location the most ideal one as for the old design.

The reactive loading of the filter on the FP is decreased by placing the filters on the voltage nodes far away from the coupler. This should minimize any coupling between the filter and the coupler. It is however, beneficial to have the filters close to the coupler so that the current runs through the longest possible length of the FP. Should the filter be placed at a less favorable location, the effect will not be detrimental due to the high rejection of the filter.

Current considerations

Now that the cross-sectional area of the FP is smaller than that of the inductive filter section, the critical current of the system must be recalculated. The new value of I_c and I_* for both

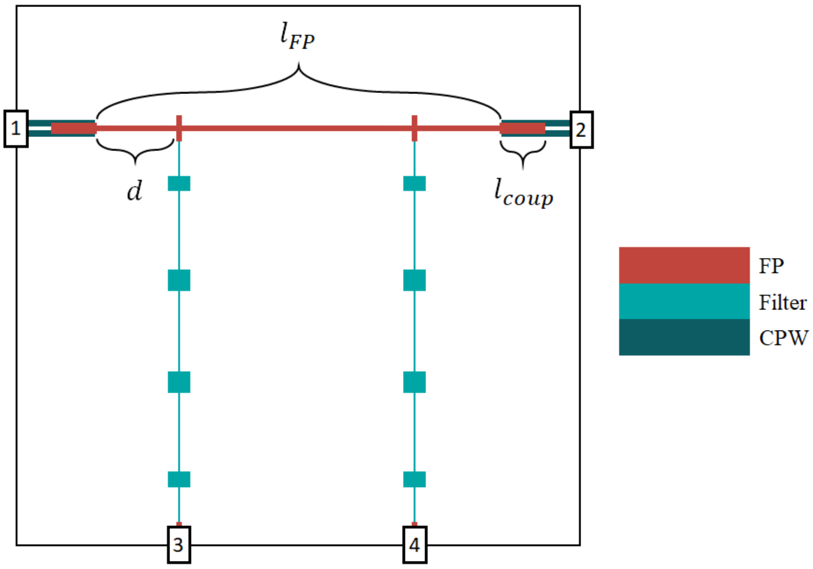

Figure 4-2: Schematic of the design of the inverted FP with the filters attached. The port numbers are the same as will be used for the following simulations.

Table 4-4: Resonance peak locations for different filter locations and their respective differences from 350 GHz. The peak frequencies and difference between them were taken from Figure 4-3 from the S_{21} of the FP (blue line). The shift in frequency was taken with respect to the FP without any filters attached to it (gray line). The peak of the 1st voltage node is out of the frequency range, therefore the shift must be larger than 30 GHz.

Filter location	Peak frequency [GHz]	Frequency shift
1st voltage node	-	> 30
1st current node	355.26	5.255
2nd voltage node	362.75	12.275

structures are given in Table 4-5. Since the I_c of the FP does not differ that much from the I_c of the inductive filter section, the simulations are again performed with a maximum current of 2 mA. The change in L_k this current induces is given in Table 4-6. For the maximum value of 2 mA, the change in kinetic inductance δL_k for the inductive filter section remains 0.1% and for the FP it is 1.76%.

Table 4-5: Critical current and non-linearity scaling factor of the FP and the filter. The values are derived from the measurements in [12] and scaled to the dimensions of this design using Equation 3-12.

	I_c [mA]	I_* [mA]
FP	4.0	15.1
Filter	4.2	15.8

Due to this high value of L_k and the fact that the critical current itself is limited by the FP, the FP is now notably sensitive to a dc bias current. In Figure 4-4, the effect of the 2 mA bias current on the FP without any filters is shown. This results in a resonant frequency shift

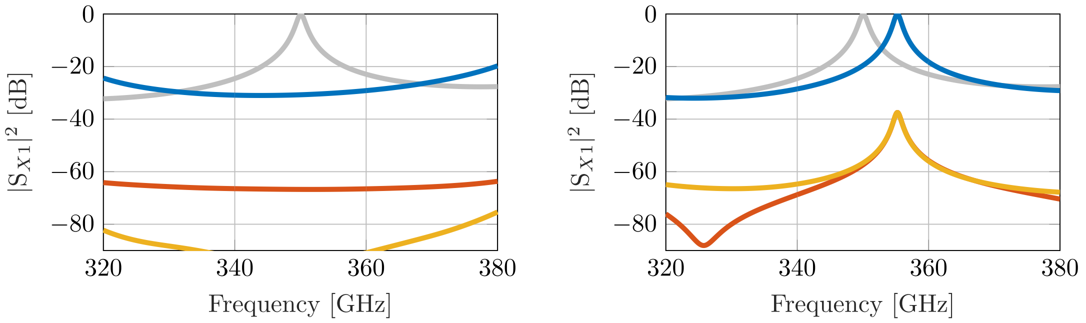

(a) First voltage node. **(b)** First current node.

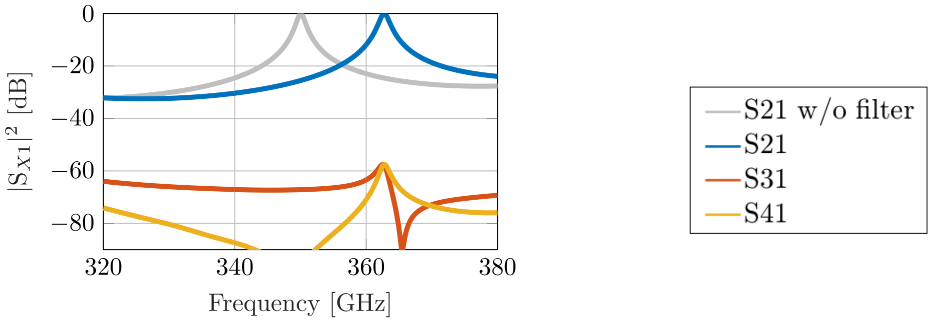

(c) Second voltage node. **(d)** Legend

Figure 4-3: The effect of the filter (without bias current) on the transmission of the FP with $n = 6$ at 350 GHz. The grey line in each plot is the S21 for the FP without the filters attached. $S21$ is the transmission of the resonator, $S31$ the transmission between one coupler and the filter nearest to it and $S41$ is the transmission between one coupler and the filter furthest from it as shown in Figure 4-2.

Table 4-6: Values of L_k for the FP and filter without biasing and with bias with a dc current of 2 mA.

	Unbiased L_k [pH]	Biased L_k [pH]	ΔL_k [pH]
FP	23577	23992	434.4
Filter	181.6	184.5	2.92

of roughly 2.6 GHz. The exact frequency shifts for modes 3 to 6 are given in Table 4-7. This shift is more than one FWHM for all modes except $n = 3$. As the mode number increases the FWHM of the peaks decreases, meaning that for larger mode numbers the shift in resonant frequency will be much more than one FWHM.

To get a better picture of the effect of the dc bias current on the entire system, the transmission through the FP for zero bias current plotted in Figure 4-3 is plotted next to the transmission with bias current of 2 mA in Figure D-11. To see the quadratic effect the current has on the shift in resonant frequency the system with the filter attached at the three different nodes has been simulated for equally spaced bias currents. The current and the corresponding value of L_s used for the simulation is given in Table D-2, the simulations in Figure D-10. The effect of the bias current on the Chebyshev filter is plotted in Figure D-12. The current has no significant impact on the filter behavior.

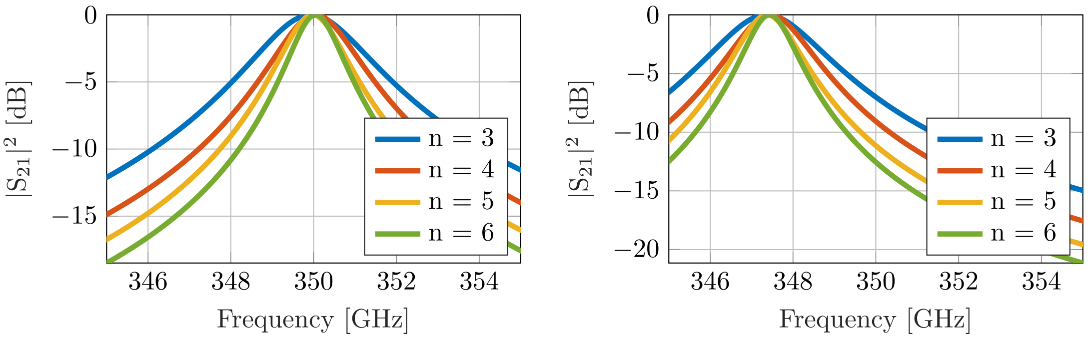

(a) Unbiased **(b)** Biased

Figure 4-4: Effect of current on a FP without filter. The level of current for the biased FPs is 2 mA.

Table 4-7: Resonance peak of Figure 4-4 for biased and unbiased FP and the frequency difference of their resonance peaks.

	f_0 Unbiased [GHz]	f_0 biased [GHz]	δf [GHz]
3rd mode	350	347.37	2.635
4th mode	350.5	347.46	2.59
5th mode	349.98	347.37	2.605
6th mode	350.5	347.44	2.615

4-1-4 Conclusion

While the new design improves the sensitivity of the FP to a bias current, it degrades the performance of the low-pass filter. Due to the electric lengths of the filters which become too long, extraneous resonances occur just outside of the 300 to 400 GHz range which makes the filter have a narrower band in comparison to the filter of the regular microstrip design. Despite this, the rejection level remains satisfactory at >45 dB levels. Despite the response of the FP being slightly disturbed by the reactive loading of the filters, the effect is not limiting its operation. As was already known from previous simulations, the optimal filter location is at a voltage node, preferably not immediately next to the coupler. When the FP is attached near the coupler there will be indirect coupling of the filter to the FP line via parasitics. The loading posed by the low-pass filter is unaltered by its positioning on the FP. However, what is reduced is the ratio of the characteristic impedance of the FP to those of the filter sections when at different locations on the FP. The application of a current of 2 mA allows the resonant frequency to be shifted by more than one FWHM which meets the system requirements. A conservative analysis with respect to the current level has been performed, so it might be possible to use a higher bias current if the measured value for I_c turns out to be larger, allowing for an even larger shift.

4-2 Measurement objectives

Now that the design works in theory, it must be implemented in such a way that it be fabricated and fit on a chip so that it can be measured. Due to the similarities between this project and the projects of K. Kouwenhoven [10] and S. Hähnle [52], the chip design for this thesis is based on theirs. A wafer can fit up to eight of these chip designs. The chips on the wafer do not need to be identical. It is however, wise to have some spare duplicates in case something goes wrong during fabrication. In the following sections, the components on the chip will be discussed. From this, the measurement objectives will be explained.

4-2-1 Chip overview

A schematic of the chip design is shown in Figure 4-5. During the measurements a chip will be placed in a holder within a cryostat. This holder is not only used to keep the chip in place, but also to prevent stray radiation, not coupled through the antenna, from being absorbed by the detectors. This stray radiation is one of the causes of the spurious noise floor [55].

The antenna design is exactly the same as in [10] [52]. There are four twin slot antennas [56] Their lenses, indicated by the dashed lines around the antennas, couples the radiation into them. After the radiation is absorbed by the antenna, it is led to the FPs (red). There are four FPs on one chip. Only the outer two FPs can be biased without having to fabricate bridges for the dc bias signal to reach them. These bias lines run through the holder to the bond pads. The output of the FPs is fed into the KID detectors which consist of an Al part (black) and an NbTiN part (green). Their behavior is measured from the read-out line. On the chip there are three blind KIDs and one blind NbTiN. These are not coupled to the antennas and therefore measure only stray radiation. This can be used in the post-processing of the data.

On the wafer, apart from the chips, there are alignment markers and dc test structures. The alignment markers will not be treated. The dc test structures are used to measure the properties of the deposited superconductors.

4-2-2 Measurement choices

The objective of the measurements is to quantify the maximum achievable frequency shift of the superconducting FPs with a dc bias current. To quantify this, three FP responses need to be known:

1. the response of a FP without any filters attached to it,
2. the response of a FP with filters attached to it but without any dc bias current and
3. the response of a FP which is biased at different current values up to the critical current.

From simulations it is known that the location of the filter on the FP has an effect on the response. Therefore it is practical to test this response with the filter at different locations. The effect on the FPs due to bias current values below $0.5I_c$ (theoretically no vortex nucleation),

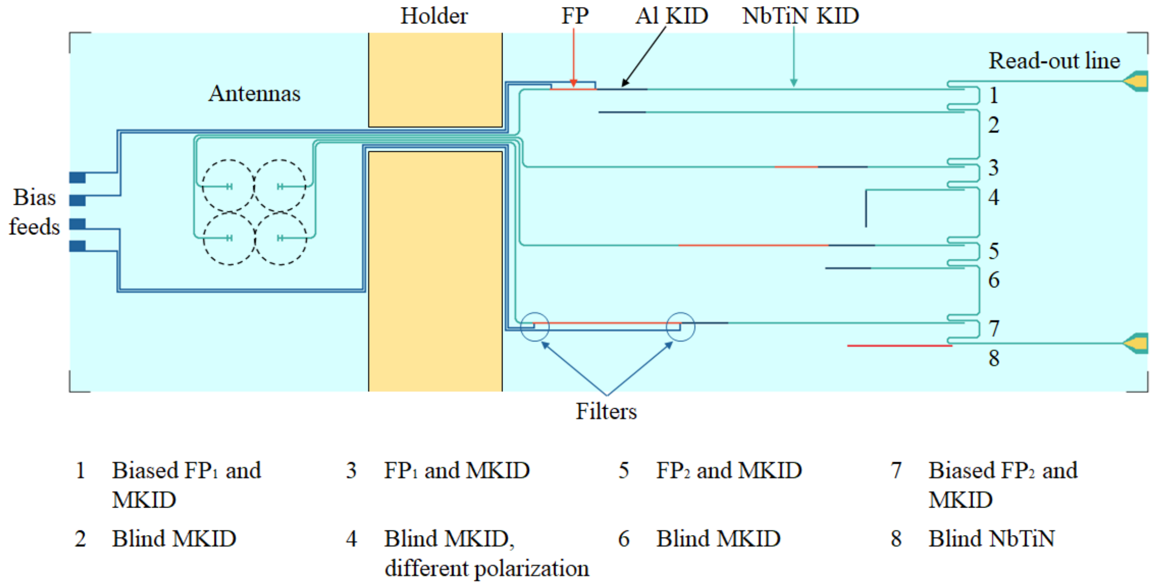

Figure 4-5: Schematic of chip layout.

between $0.5I_c$ and I_c (superconductor enters mixed state) and above I_c (superconductivity lost) should be measured. It is also very useful to measure the current in order to confirm the exact value of the critical current to be able to establish whether the equations (Equation 2-19 and the ones in the text) are correct.

All these responses can be measured using a chip design as shown in Figure 4-5. On a single chip there is a total of four in-line FPs (numbers 1, 3, 5 and 7) of which two are biased (1 and 7) and two are not biased (3 and 5). Apart from the biasing, FPs 1 and 3 and FPs 5 and 7 are identical to each other. In this way, the difference between responses 1 and 2/3 can be measured. The design specification for the two different FPs is given in Table 4-8. Their output should theoretically look like the ones in Figure 4-6. All MKIDs, behind a FP or a blind FP, are designed for different frequencies so that the measurements of all seven can be read-out simultaneously.

Table 4-8: Calculated values for an FP with $Q_i = 3500$ at 350 GHz.

Q_l	S_{21c} [dB]	Q_c	$Q_{c,FP}$	f_0 [GHz]	n_{vis}	l_{FP} [mm]
2500	-12	49.8	8750	1.9916	50	5.786
1500	-12	49.8	2625	6.6388	15	1.7358

Since there can be up to eight different chips on the wafer, each chip will have the filters at a different location on both biased FPs. The locations will be the ones which were simulated, namely the first voltage and current nodes and the second voltage node. This gives three different chip designs. To ensure that a small fabrication error does not ruin the measurement, each of these three chips is fabricated twice, giving six chips in total. Because of the extra space, it is possible to have a dc test structure in between each chip as well as on the sides of the wafer.

Each dc test structure contains four pads which are used to measure the characteristics of

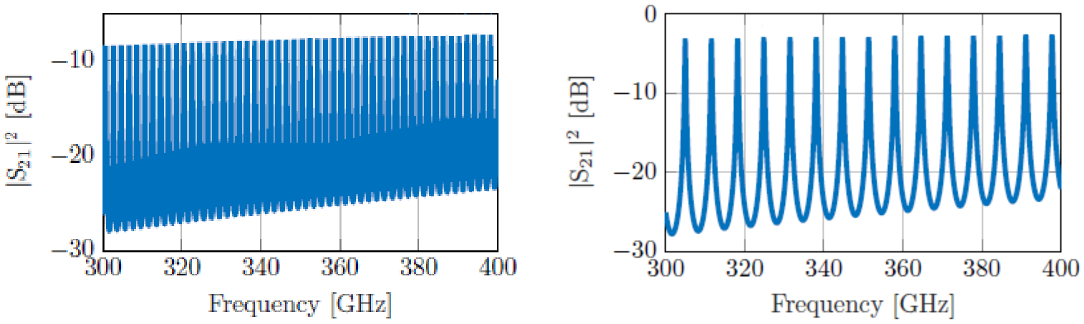

(a) $Q_l = 2500$

(b) $Q_l = 1500$

Figure 4-6: Effect of current on a FP without filter. The level of current for the biased FPs is 2 mA.

the different NbTiN layers (FP, filter and ground plane) as well as the Al of the KIDs. It is beneficial to have several of these test structures close to the chips as the metal layers may vary across the wafer [57]. The test structure of the FP NbTiN and the filter NbTiN are also used to measure the exact value of I_c. As the I_c of the FP and the inductive filter section are very close, it useful to measure this and determine the upper current limit of the system.

4-3 Fabrication

While preparing for the fabrication of the wafer some aspects of the design had to be worked out in further detail and issues came to light. These are discussed briefly before moving on the to fabrication process. Here the detail of the masks will be discussed and the final material properties given.

4-3-1 Additional design details

To avoid problems with fabrication and to ensure the functionality of the design four changes were made to the final design. The reason for these changes and how they are implemented are discussed below. None of these changes are simulated.

FP thickness

In the new design, the FP is so thin that the calculations of the sheet kinetic inductance require feedback from previous batches to accurately infer the properties of the film. Therefore, the thickness and corresponding L_s are extrapolated from fabrication data [58]. The measured data for films of different thicknesses is plotted in Figure 4-7. From the extrapolated curve, a superconducting NbTiN strip with $L_s = 4$ pH/sq corresponds to a thickness of the FP is 34.847 nm. This value, instead of the $t = 22$ nm given in Table 4-1, is used for fabrication. This causes the I_c of the system to be limited by the inductive filter section since its cross-sectional area is again smaller and therefore makes the FP slightly less sensitive.

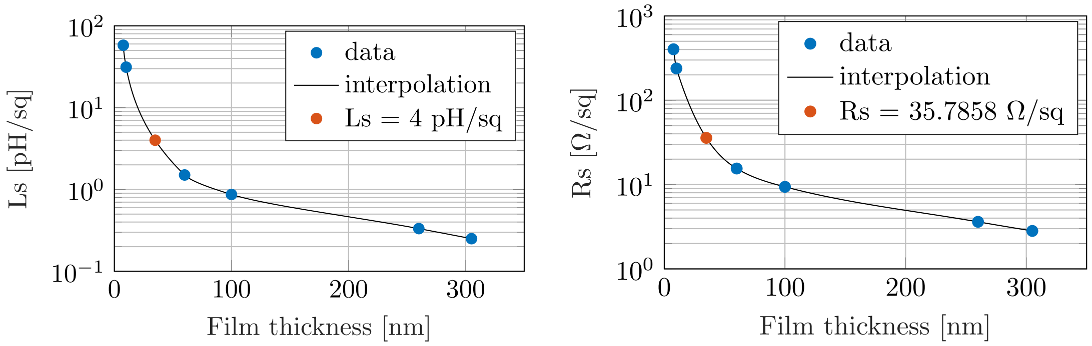

(a) L_k extrapolation **(b)** R_s extrapolation

Figure 4-7: Extrapolation of L_k and R_s from fabrication data [58] to ensure correct FP thickness. The correct thickness is equal to 34.847 nm.

Current crowding

As mentioned before, the critical current of a superconductor heavily depends on the geometry; not only on the cross-sectional area, but also on any sharp discontinuities such as 90° turns, sudden changes of the strip width or intersections. This effect is shown in Figure 4-8. The current tends to concentrate in the inner corners of these discontinuities, forming local hot spots. In these hot spots the critical current can be greatly reduced. This reduction is caused by heat build-up as well as vortex formation as vortexes are pinned to both impurities and irregularities in the geometry of the superconductor [59]. H. L. Hortensius in [60] found that for strips with a width smaller than the Pearl length (Equation 2-8) but larger than the coherence length (Equation 2-5) the reduction R in I_c is proportional with

$$R \propto (\xi/w)^{1/3} \qquad \text{for } \xi < w < \lambda_\perp. \tag{4-1}$$

The coherence length for NbTiN is roughly 50 nm, so for the FP a reduction of roughly $R \propto 0.3$ and for the inductive sections of the filter roughly $R \propto 0.45$ are expected. To avoid this reduction, curves with a radius of 700 nm have been added to the filter and FP.

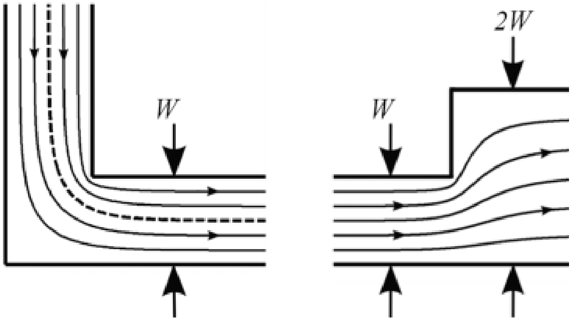

Figure 4-8: Current crowding in the case of a sharp current and a sudden widening in the superconductor geometry. Image taken from [60].

Trenching

Trenching is an unwanted phenomenon which can occur around a structure after it is etched. In some cases the etching medium can over-etch the surrounding of the mask, causing a trench to form around it. This poses an even bigger problem when the superconducting strips are very thin as in the case of the connection of the filter and the FP. After the excess NbTiN of the filter is etched away the thin layer of FP is deposited over it. If a trench has formed, it could cause the FP strip to break. To prevent this, a patch of Silicon-Nitrite (SiN) is placed below this connection point. This helps because SiN etches away slower than the Si of the wafer.

Trenching however, can also occur around dielectrics such as a SiN patch. An example of trenching is shown in Figure 4-9. The SEM image in both panels is the same, on the left the layers are identified and the numbers stand for the amount of times the material is etched, on the right the trench is highlighted for clarity. On this particular wafer five layers are deposited and etched in the following order: the SiN patch, the NbTiN ground plane (GP), the a-Si dielectric, the NbTiN strip in the middle and finally the Al strip in the middle. After the first four steps, the Si of the wafer, not covered by the NbTiN GP, has been etched four times, forming a trench. This trench is too deep and Al strip does not connect over it.

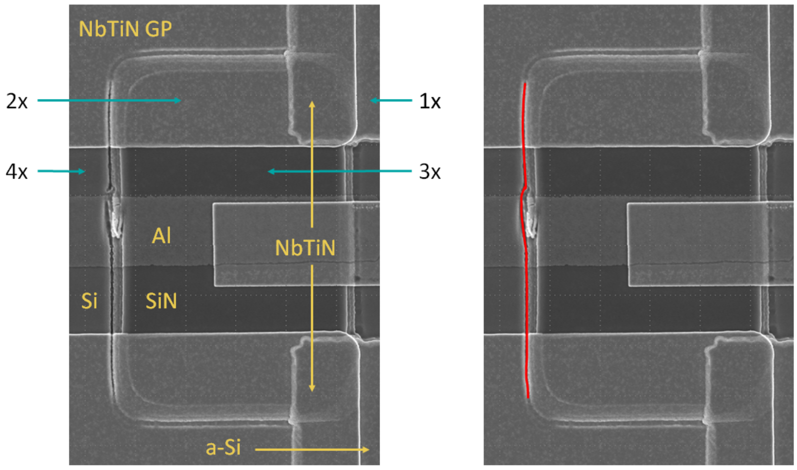

Figure 4-9: SEM image from [61] showing a trench formed in an area where there has been too much etching. Left panel show the materials and how many times they have been etched during fabrication. Right panel highlights the trench. The artifact between the trench and the SiN patch is debris.

In order to avoid trenching in all areas where SiN patches are used, patches of a-Si are deposited, and if already there, extended. The a-Si patch acting as the dielectric for the microstrip filter and FP is extended over the newly placed SiN patch. This is shown in Figure E-1. A large patch of SiN is also located beneath the transition of the Al to NbtiN section of the KIDs. In this case a new patch of a-Si is deposited as shown in Figure E-2. The same is done at both ends of the blind KIDs.

Quality factor of inverted microstrips

Right before the masks for this design were finished, measurement from within the Terahertz Sensing group showed that the Q_i of inverted microstrip resonators is lower than expected. K. Kenichi, [62] [63], showed that the actual Q_i value lies between 400 and 500. From Equation 2-29 and Equation 2-32, it is clear that this has a detrimental effect on the peaks in the resonator. Due to the drop in Q_i, the Q_l will drop as well meaning that the peaks will be very low, possibly below the noise floor.

For this reason two more chips are designed using a CPW FP. This architecture is shown for one coupler in Figure 4-10. From the antenna side the design remains the same: the coupler and the beginning of the FP, where the filter is attached is still implemented as an inverted microstrip. After the filter is attached the CPW starts on top of the a-Si patch. This is a negative mask, so the green lines indicate where the NbTiN of the CPW will be etched away. After the a-Si patch stops, the CPW drops to the same level of the microstrip FP, and the microstrip forms the center line of the CPW. This trick should improve the Q_i. The addition of two CPW FP chips removes the extra space for the dc test structures. In the final mask there are only two dc test structures located either side of the wafer.

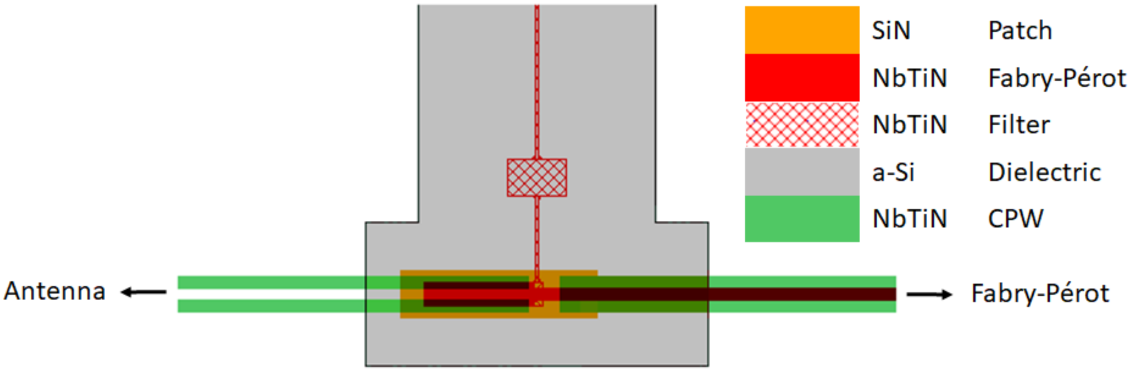

Figure 4-10: Schematic of the CPW FP.

4-3-2 Mask layers

For this design there is a total of eight masks. There are different etching processes or combinations of etching processes used for each mask. The choice between these options depends on the dimensions of the structure which needs to be printed and tolerances in misalignment. The process, in order of very to less accurate, are Electron Beam Pattern Generator (EBPG), UV Lithography and wet/gas etching. The EBPG is used for five layers. The fabrication process and important properties of the superconductor and dielectric layers are briefly discussed in the paragraphs below. This is only done for the chips, without the alignment markers, not the entire wafer.

Step 1

The first step in the process is the deposition of the SiN patches. These are located beneath the point where the FP is attached to the filter to prevent trenchig as shown in Figure 4-9, beneath the Al section of the KID and beneath the CPW read-out line. This is shown in Figure 4-11.

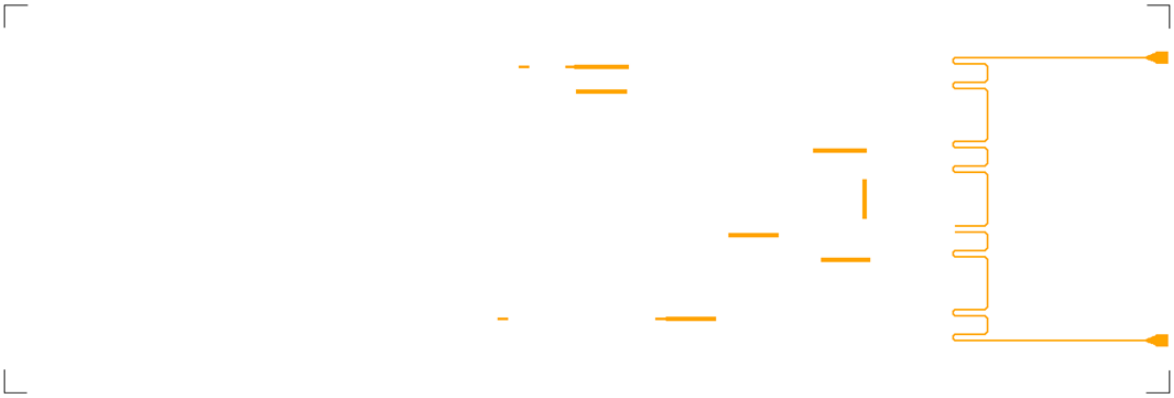

Figure 4-11: Mask layer 1: SiN patches.

Step 2

The first layer of NbTiN is deposited in the second step. This is used for the filters and the dc bias lines as shown in Figure 4-12. The end of the filter, which is connected to the FP, climbs up the SiN patch which is already deposited. The dc bias lines run through the chip to the connectors on the side of the antennas. Due to the width of the individual filter sections, the EBPG is necessary. The final NbTiN properties for this layer are shown in Table 4-10.

Table 4-9

ρ [Ωm]	T_c [K]	L_k [pH/sq]	t [nm]
$120 \cdot 10^{-8}$	14.3	1.0	115

Step 3

The EBPG is used again for the second NbTiN layer due to the small tolerances in misalignment. The NbTiN is also deposited for the blind NbTiN strip. This addition to the chip is shown in Figure 4-13 and the extrapolated NbTiN properties from Figure 4-7 are given in Table 4-10.

Table 4-10

ρ [Ωm]	T_c [K]	L_k [pH/sq]	t [nm]
$122.5 \cdot 10^{-8}$	13	4.0	35

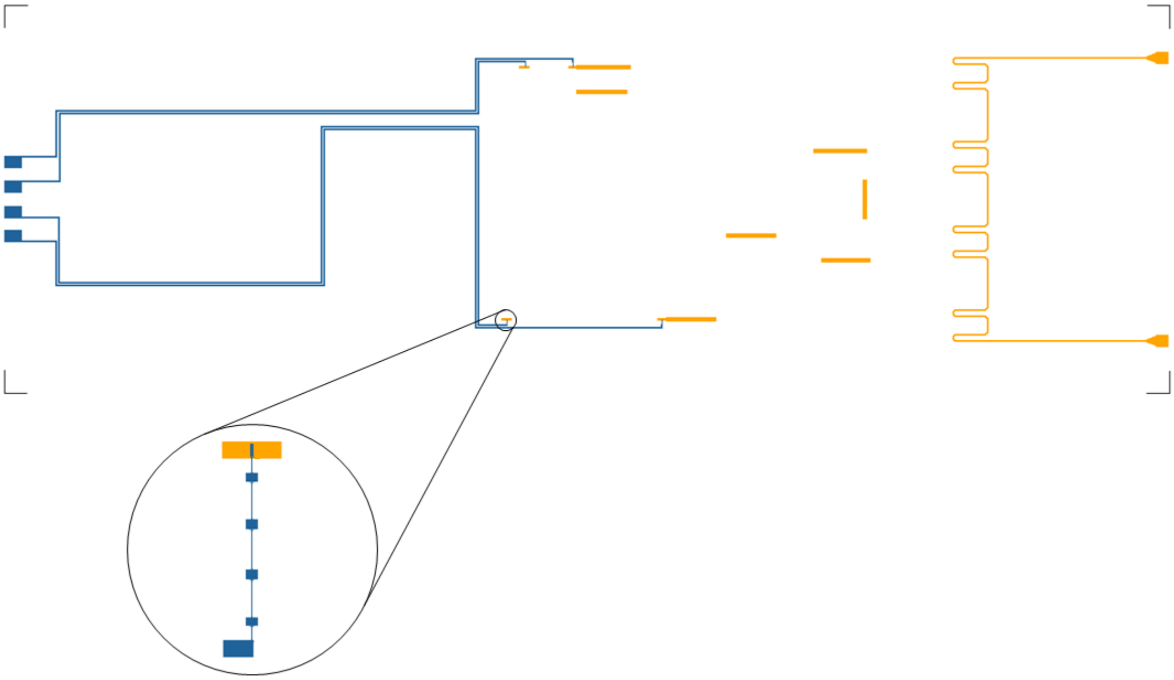

Figure 4-12: Mask layer 2: NbTiN of the filters and dc bias lines.

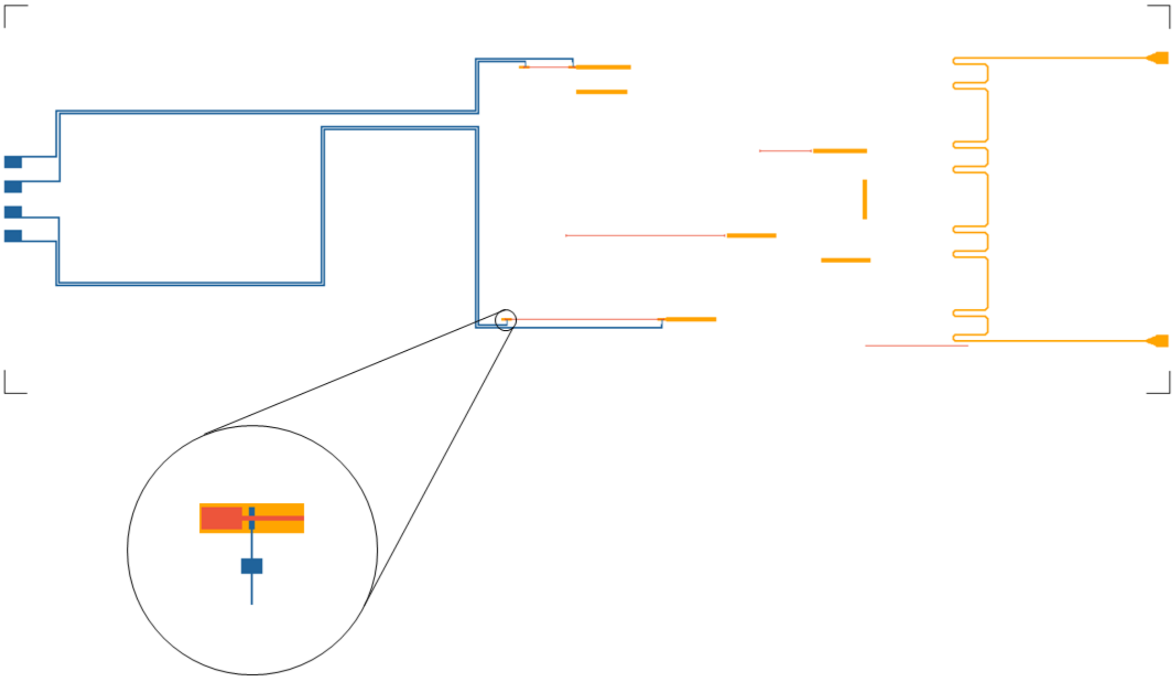

Figure 4-13: Mask layer 3: NbTiN of the FP.

Step 4

The patches of a-Si are deposited and etched in step 4. The a-Si is used as the dielectric for the microstrip filters and FPs as well as to prevent the trenching in all areas where a SiN patch may be etched too many times. a-Si has a dielectric constant of 10 and the layer itself will be 300 nm thick. This is shown in Figure 4-14.

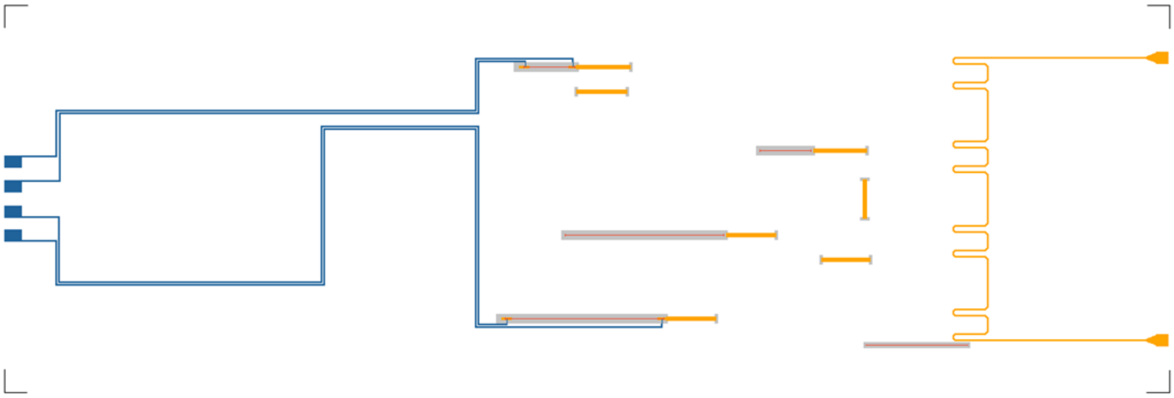

Figure 4-14: Mask layer 4: a-Si patches.

Step 5

The fifth step in the process is the deposition of a Tantalum (Ta) mesh on the backside of the wafer as shown in Figure 4-15. This mesh is used to block stray radiation from entering the chip through the backside or reaching the detectors as surface waves. Ta has a resistivity ρ of $240 \cdot 10^{-8}$ Ωm and after etching has a thickness of 40 nm.

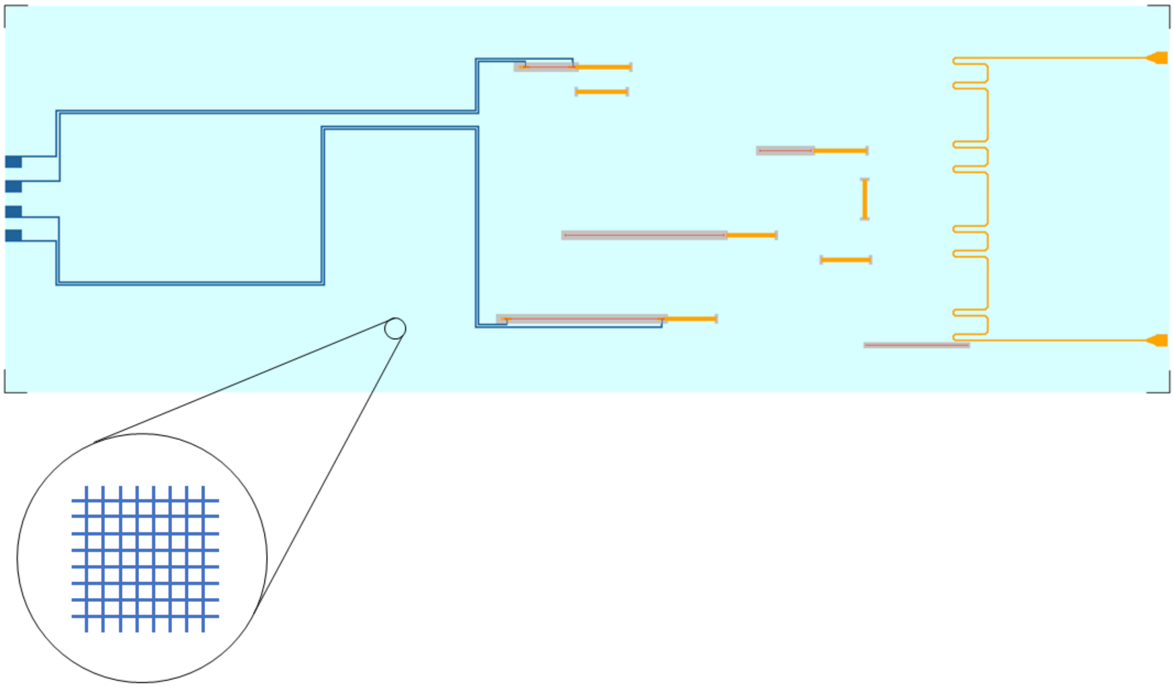

Figure 4-15: Mask layer 5: Ta backside.

Step 6

The third layer of NbTiN makes up the ground plane for the microstrip structures, KID, antennas and THz line and the read-out line. This is a negative mask, meaning that everywhere it is drawn in, the NbTiN will not be deposited. The properties of this layer of NbTiN are given in Table 4-11. Especially for the fourth CPW FP strip, there is barely room for any misalignment, therefore EBPG is used again in this step. The addition of this layer is shown in Figure 4-16.

Table 4-11

ρ [Ωm]	T_c [K]	L_k [pH/sq]	t [nm]
$900 \cdot 10^{-9}$	15	0.926	107

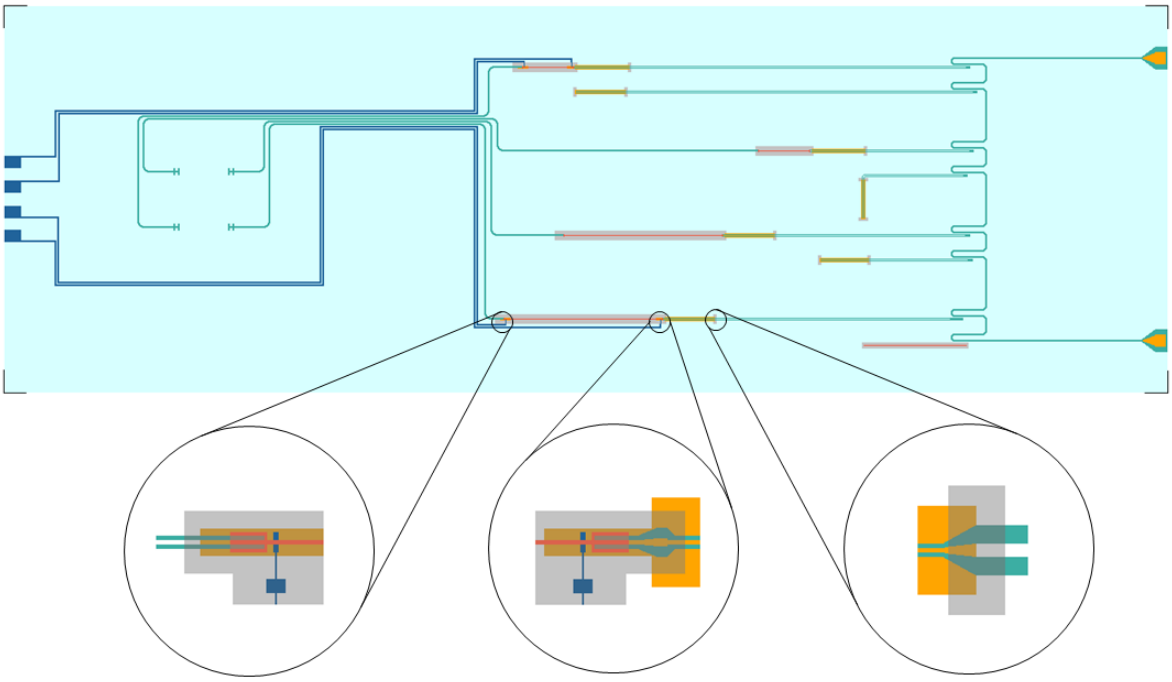

Figure 4-16: Mask layer 6: NbTiN ground plane and CPW read-out line, THz line and KID.

Step 7

In the seventh step, small patches of Polyimide are deposited over the CPW read-out and THz-signal lines Figure 4-17. Over these bridges, small Al strips will connect both ground planes. This is done to avoid any common-mode excitation in the CPW lines. The thickness of the Polyimide bridges will be 400 nm.

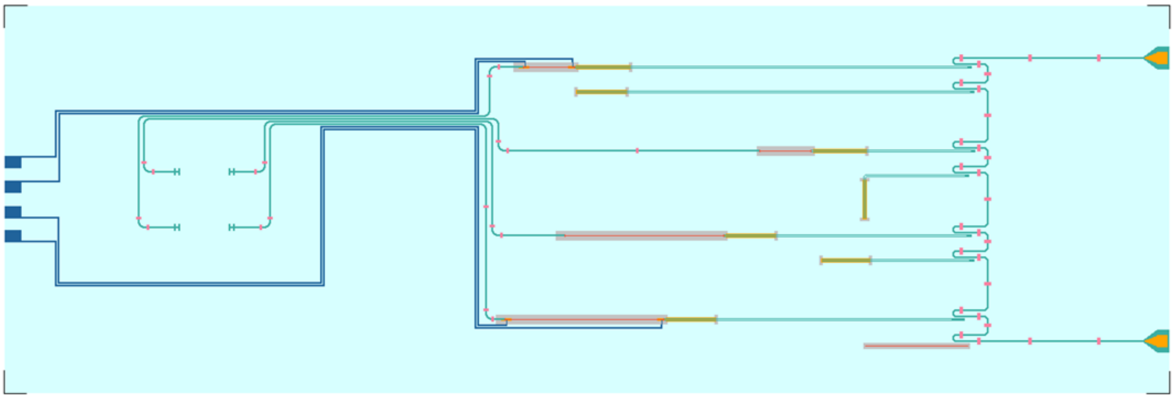

Figure 4-17: Mask layer 7: Polyimide for bridges.

Step 8

The final step involves the deposition of the Al KIDs and bridges as shown in Figure 4-18. The material properties are given in Table 4-12.

Table 4-12

ρ [Ωm]	T_c [K]	t [nm]
$1.6 \cdot 10^{-8}$	1.25	40

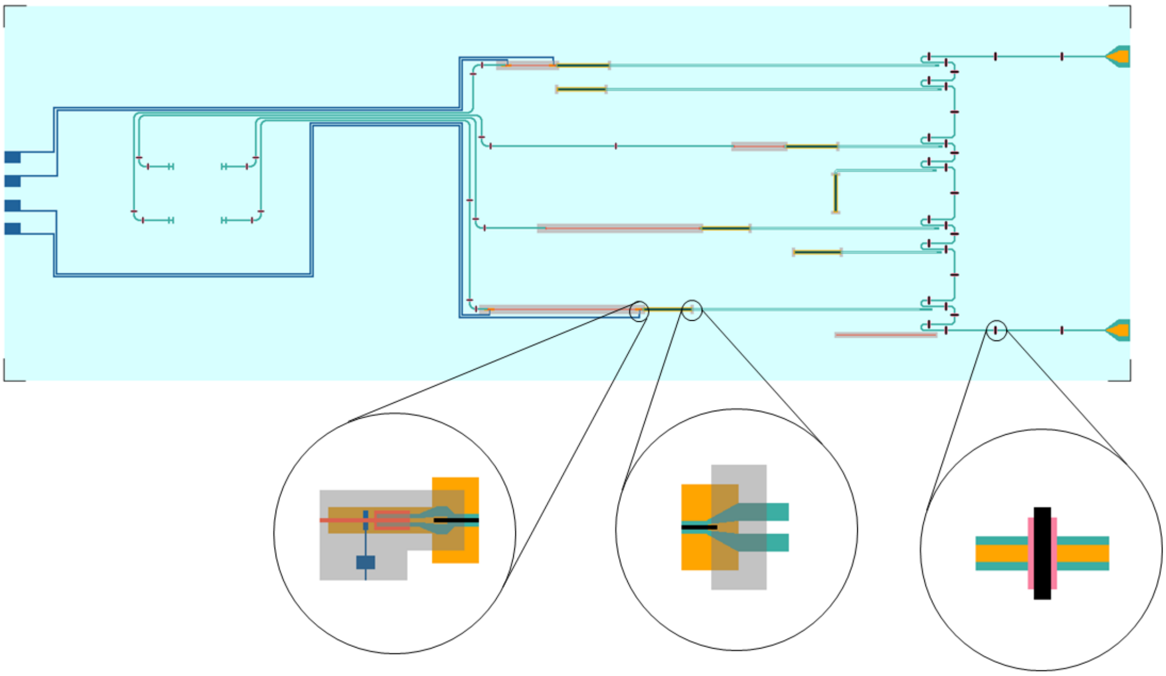

Figure 4-18: Mask layer 8: Al for KID and bridges.

Chapter 5

Conclusions and outlook

In this chapter the conclusions of the work are presented and discussed. The aim of this thesis, as defined in section 1-2, is to provide an on-chip platform to quantify the achievable phase-shifting capabilities at terahertz frequencies through a dc-biased FP, where the resonance peaks are shifted in frequency. To create a design for such a bias system, the theoretical effect of a dc bias current on a superconducting resonator was thoroughly studied. The literature study reveals that such a bias system can be implemented using a low-pass filter. However, since all the studies analyzed work with microwave signals, a different type of low-pass filter needs to be designed for this THz application. For this design there were three requirements:

1. The shift in resonance frequency should be more than the Full Width Half Magnitude (FWHM) bandwidth of the unbiased peaks.
2. The biasing system cannot alter the shape of the peaks and their orignal location (f_0) by more than 10%.
3. The frequency range in which it must be able to scan is 300 - 400 GHz.

In the following sections the design of the low-pass stepped-impedance filter and the sensitivity of the entire system to the dc bias current are discussed. Both the regular and inverted microstrip designs are used for this discussion. Due to time constraints the chip could not be measured before this thesis was written. The conclusions will therefore only be drawn from the simulation results. After this discussion, the feasibility and effectiveness of the implementation of this design for steerable superconducting antennas is explored. Finally, this chapter will conclude with an outlook on future work and other recommendations.

5-1 Stepped-impedance filter

One of the two most significant changes when switching from the regular to the inverted microstrip implementation is the deterioration of the filter transmission. For the stepped-impedance filter sections to approximately behave as inductors and capacitors it is imperative for the electrical phase to be smaller than $\pi/4$. Since the width of the FP is set at 2 μm, there is not a lot of room left to make the inductive section significantly narrower before fabrication limits are reached. Even though the inverted microstrip structure increases the effective permittivity (the ε_r of Si is 11.44) which increases the maximum electrical phase slightly (and decreases the characteristic impedance), the electrical phase of the inductive sections was too large, allowing extraneous resonant behavior to emerge and diminish the rejection. When such a distributed-element filter is designed for a steerable antenna, the characteristic impedances must be carefully chosen.

The location of the filters on the FP with respect to the couplers affects the reactive loading of the FP. From the simulations of the regular microstrip design it can be interpreted that the further the filters are located from the couplers, the smaller the reactive loading becomes. The reactive loading of the filter affects the Q-factors of the peaks. With all filter placements the FWHM becomes slightly larger. This change remains below 10% and is therefore acceptable. From the simulations of both microstrip implementations the conclusion can be drawn that the filters should not be attached too close to the couplers. This is due to two reasons. The first is that the filters couple to couplers, introducing spurious resonances. The second is that the outer edge of the coupler is a current node and that the wider section of the coupler modifies the standing wave pattern by smearing it. Therefore it is an unfavorable position for the connection of the filter.

The simulated value of the locations of the filters do not apply to the actual long resonators since the length of resonator does not change anymore, but the wavelength does. For each mode there will be a different amount of voltage and current nodes and their locations will therefore be different. In the case of this design, where the FP has many modes, the distance between the voltage or current nodes becomes very small and any fabrication misalignment can lead to the filter being at either an enhancing or a diminishing location. Even when the filter is located at an unfavorable position, the rejection is still satisfactory.

Both filter designs meet the third requirement. Simulations show that the minimal rejection in the 300 to 400 GHz band is roughly 45 dB, which is enough to prevent the THz signal from leaking through the dc-biasing network.

5-2 System sensitivity

The second of the two most significant changes between the designs is the improvement in sensitivity to a change in dc current. The increase of $L_k(0)$ is the parameter which has the largest impact on the sensitivity. In this case the $L_k(0)$ is increased by making the superconductor thinner. It could also be increased by choosing a different superconductor with a lower T_c (thus lower Δ) or a larger ρ. For maximal sensitivity, it is necessary that the resonator limits the current, not the low-pass filter. Increasing the value of I_* and therefore I_c has a smaller effect on the sensitivity since it is their ratio what really determines the kinetic inductance tunability.

From the simulations of the inverted microstrip design, a frequency shift of roughly 0.7% is observed. This is more than one FWHM (almost 2.5 times) and the system therefore satisfies the first requirement. This frequency shift is comparable to the phase shift found in [11]. With the conservative estimate of the maximum bias current of the FP, all other studies in which a dc bias current is implemented the measured shift in phase or frequency is larger. It is important to note that this result will improve when the resonator has a higher mode number as the FWHM of the peaks becomes narrower, as will be the case for the implemented designs to be fabricated. Another matter is that in [14] the shift is found to become larger with frequency. This is not seen in simulations because the values of ε_{eff} and others are only simulated for the peak at 350 GHz. The frequency dependence of many variables has not been taken into account. This will probably be seen in the measurements though.

When the measurements will take place it is important to keep in mind that two very large assumptions about the current in the superconductor are made. The first is that the current is uniform over the superconducting strips and the second is that no thermal excitation of quasiparticles is caused by the current. Both of these can decrease the theoretical value of I_c.

5-3 Implementation of steerable antennas

The simulations show that the transmission peaks in the Fabry-Pérot resonator can be tuned by 0.7%. This proof of concept means that it can be applied to the feed lines of antenna to change the phase of the signals in order to steer the beams. This could be implemented as shown in Figure 5-1. With each antenna element receiving the signal at a different phase it is possible to scan, in the set-up in Figure 5-1, from left to right. Due to the superconductivity the current can run through the different lines with negligible conductor loss. The 0.7% obtained for the design of this thesis is quite small, but would still work for scanning. An impression of a broadband beam-steering antenna is shown in Figure 5-2 [9]. Due to the many elements in the antenna array, the inter-slot spacing is already crowded with the feeding network. Since the size of the filters would be so small it is no problem to fit them in. The real problem lies with the addition of the current bias lines. For that, the feeding network would probably need to lie outside the antenna aperture.

In conclusion, creating a steerable antenna with this design is definitely feasible, however the sensitivity should be increased in order to be able to steer a satisfactory amount.

5-4 Outlook

Depending on the measurement results, but also in general, there are several areas in which this design can be developed further. These include different implementations of the feed lines/resonator, different filters and different materials.

Since the Q_i of the inverted microstrip is very low, it is wise to design the system for regular microstrips or CPW lines. The design of the regular microstrip in this thesis can easily be made more sensitive by increasing the $L_k(0)$ of the FP. Looking at the characteristic impedance ratios, this might even be a better design than the inverted microstrip design proposed here. Compared to microstrip resonators, CPW resonators have much a better Q_i. They could therefore be beneficial to use. Especially since the stepped-impedance filter can also be implemented as a CPW.

The design in this thesis works with dc bias currents and can also be used for low ac frequencies ($f \ll f_c$). When dc currents are used, there always needs to be a closed path for the current

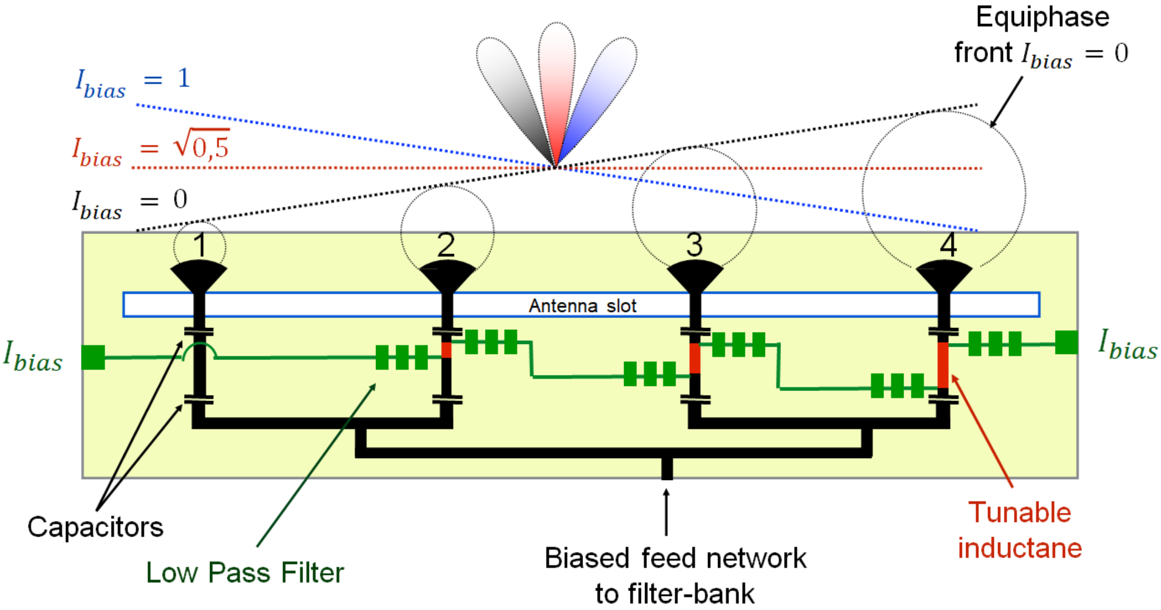

Figure 5-1: Schematic of a steerable-beam antenna with a biased feeding network.

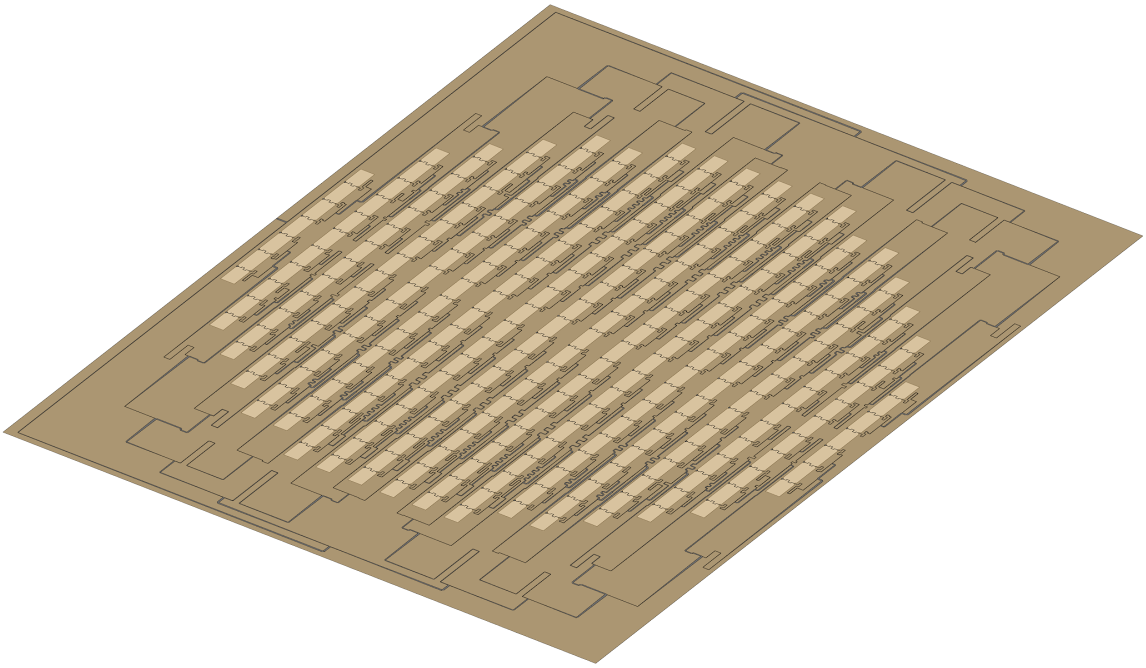

Figure 5-2: Impression of steerable connected array antenna [9].

to enter and leave the resonator. For this, only minimum phase filters are studied since they are the simplest to fabricate. Apart from the stepped-impedance design, open-circuited stub filters can also be implemented for dc currents. Should only a low frequency ac bias current be used it is possible to design coupled resonator filters or hairpin filters. These can be made extremely narrow-band to only allow the ac bias current to pass. This could also be necessary if the measured frequency range of 300 to 400 GHz is increased since then the stepped-impedance filter will become extremely small.

Finally, it is also possible to experiment will different superconductors and dielectrics. Superconductors with larger normal state ρ have larger $L_k(0)$ and will therefore be sensitive without having to use it with a small cross-sectional area. Using dielectrics with low dielectric losses will greatly improve the microstrip resonator behavior and therefore enhance the effect of the current biasing.

Appendix A

Derivation of filter order

The reflection coefficient $S_{11}(j\omega)$ and transmission coefficient $S_{21}(j\omega)$ of a lossless passive two-port network can be expressed in decibels and represent the signal attenuation in the pass-band and stop-band, respectively [48] [64]. These correspond to A_p and A_s in Figure 2-13. Together with the pass-band frequency ω_p and stop-band frequency ω_s they are used to calculate the filter order.

$$A_p = -20\log_{10}|S_{11}(j\omega)| \text{ dB} \qquad 0 < \omega < \omega_p \tag{A-1}$$

$$A_s = -20\log_{10}|S_{21}(j\omega)| \text{ dB} \qquad \omega_p < \omega < \infty. \tag{A-2}$$

A-1 Butterworth filter

To calculate the order N of the Butterworth filter, its transmission coefficient $S_{21}(j\omega)$, from Equation 2-43, must be substituted into Equation A-1 and Equation A-2 which will be rewritten in terms of ω/ω_c. For the calculations for the pass-band, the $S_{11}(j\omega)$ needs to be calculated using $|S_{11}(p)|^2 + |S_{12}(p)|^2 = 1$. The expression for A_p is then

$$A_p = 10\log_{10}\left[1 + \left(\frac{\omega_p}{\omega_c}\right)^{2N}\right] \quad \longrightarrow \quad \left(\frac{\omega_p}{\omega_c}\right)^{2N} = 10^{A_p/10} - 1 \tag{A-3}$$

$$\longrightarrow \quad \frac{\omega_p}{\omega_c} = \left(10^{A_p/10} - 1\right)^{\frac{1}{2N}} \tag{A-4}$$

$$\tag{A-5}$$

The same can be done for the stop-band. The result is

$$\frac{\omega_s}{\omega_c} = \left(10^{A_s/10} - 1\right)^{\frac{1}{2N}}. \tag{A-6}$$

The filter order N can then be found by solving Equation A-3 and Equation A-6 for ω_c and then equating them to each other. The final expression for N is given in Equation A-7, which is rounded up to the next integer.

$$\frac{\omega_p}{\left(10^{A_p/10}-1\right)^{\frac{1}{2N}}} = \frac{\omega_s}{\left(10^{A_s/10}-1\right)^{\frac{1}{2N}}} \longrightarrow \quad \frac{\omega_p}{\omega_s} = \left(\frac{10^{A_p/10}-1}{10^{A_s/10}-1}\right)^{\frac{1}{2N}} \tag{A-7}$$

$$\longrightarrow \quad \left(\frac{\omega_p}{\omega_s}\right)^{2N} = \left(\frac{10^{A_p/10}-1}{10^{A_s/10}-1}\right) \tag{A-8}$$

$$\longrightarrow \quad 2N\log_{10}\left(\frac{\omega_p}{\omega_s}\right) = \log_{10}\left(\frac{10^{A_p/10}-1}{10^{A_s/10}-1}\right) \tag{A-9}$$

$$\longrightarrow \quad N = \left\lceil \frac{1}{2}\frac{\log_{10}\left(\frac{10^{A_p/10}-1}{10^{A_s/10}-1}\right)}{\log_{10}\left(\frac{\omega_p}{\omega_s}\right)} \right\rceil \tag{A-10}$$

A-2 Chebyshev filter

By setting the frequency to the cut-off frequency and using the property of the Chebyshev polynomial that $T_N(1) = 1$, the response of the Chebyshev filter, Equation 2-52, can be written as [64]

$$\left|S_{12}(j\omega)\right|^2 = \frac{1}{1+\varepsilon^2 T_N^2(\frac{\omega}{\omega_c})} = \frac{1}{1+\varepsilon^2}. \tag{A-11}$$

This means that the maximum allowable pass-band attenuation can be written as

$$A_p = 10\log_{10}\left(1+\varepsilon^2\right) \quad \longrightarrow \quad \varepsilon = \sqrt{10^{A_p/10-1}} \tag{A-12}$$

The Chebyshev filter order can then be found by calculating A_s and rounding it up to the next integer. For $\omega > \omega_s$, from Equation 2-53 it is clear that the Chebyshev polynomial starts to play a role and the function for A_s becomes

$$A_s = 10\log_{10}\left(1+\varepsilon^2 T_N^2\left(\frac{\omega_s}{\omega_c}\right)\right) = 10\log_{10}\left(1+\varepsilon^2\cosh^2\left[N\cosh^{-1}\left(\frac{\omega_s}{\omega_c}\right)\right]\right) \tag{A-13}$$

$$\longrightarrow \quad \frac{10^{A_s/10}-1}{\varepsilon^2} = \cosh^2\left[N\cosh^{-1}\left(\frac{\omega_s}{\omega_c}\right)\right] \tag{A-14}$$

$$\longrightarrow \quad \cosh^{-1}\sqrt{\frac{10^{A_s/10}-1}{\varepsilon^2}} = N\cosh^{-1}\left(\frac{\omega_s}{\omega_c}\right) \tag{A-15}$$

$$\longrightarrow \quad N \geq \left\lceil \frac{\cosh^{-1}\sqrt{\frac{10^{A_s/10}-1}{\varepsilon^2}}}{\cosh^{-1}\left(\frac{\omega_s}{\omega_c}\right)} \right\rceil = \left\lceil \frac{\cosh^{-1}\sqrt{\frac{10^{A_s/10}-1}{10^{A_p/10}-1}}}{\cosh^{-1}\left(\frac{\omega_s}{\omega_c}\right)} \right\rceil. \tag{A-16}$$

Appendix B

Transmission line equivalent circuit for stepped-impedance filter

The behavior of a lossless transmission line can be fully described by its length l, characteristic impedance Z_0 and phase constant $\beta = 2\pi/\lambda$. When the electric length of a transmission line is electrically short, i.e. $\beta l << \pi/4$, this line can be approximated with lumped elements in a T- or π-equivalent circuit. For this derivation the T-equivalent circuit is used, which is shown in Figure B-1. To obtain the values of the lumped elements, the transmission line is first written in terms of its ABCD parameters as

$$\begin{bmatrix} A & B \\ C & D \end{bmatrix} = \begin{bmatrix} \cos(\beta l) & jZ_0 \sin(\beta l) \\ jY_0 \sin(\beta l) & \cos(\beta l) \end{bmatrix}. \tag{B-1}$$

The ABCD parameters are then converted to the Z parameters through standard conversions found in [43]. The Z parameters describe the impedances at and between the ports of the network and can be used to obtain the values of the T-equivalent network as described in [43].

$$\begin{bmatrix} Z_{11} & Z_{12} \\ Z_{21} & Z_{22} \end{bmatrix} = \begin{bmatrix} A/C & (AD-BC)/C \\ 1/C & D/C \end{bmatrix} = \begin{bmatrix} -jZ_0 \cot(\beta l) & -jZ_0 \csc(\beta l) \\ -jZ_0 \csc(\beta l) & -jZ_0 \cot(\beta l) \end{bmatrix} \tag{B-2}$$

Since the circuit is symmetric the value of the inductors is the same and can be found by subtracting Z_{12} from Z_{11}, this is calculated in Equation B-3. For this calculation, the half-angle identity $\tan(\theta/2) = \csc(\theta) = \cot(\theta) = \frac{1-\cos(\theta)}{\sin(\theta)}$ is used. The susceptance of the capacitance is described by Z_{12} only and it is calculated in Equation B-4.

$$j\omega L = j\frac{X}{2} = Z_{11} - Z_{12} = Z_0 (\csc(\beta l) - \cot(\beta l)) = Z_0 \tan\left(\frac{\beta l}{2}\right) \tag{B-3}$$

$$j\omega C = jB = \frac{1}{Z_{12}} = -\frac{1}{Z_0 \csc(\beta l)} = -\frac{1}{Z_0}\sin(\beta l) \tag{B-4}$$

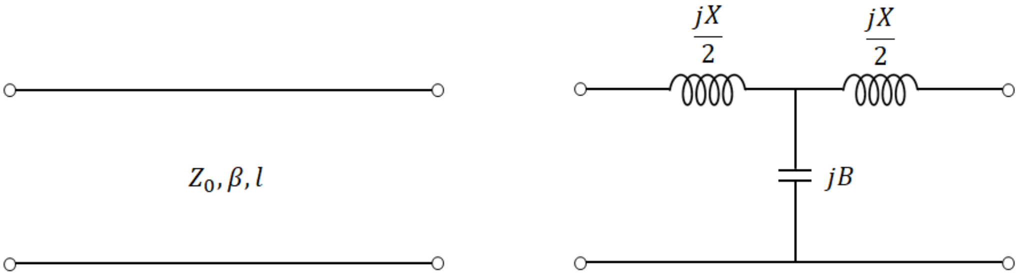

Figure B-1: Transmission line and equivalent T-model.

It is important that the length of the transmission line segment is electrically short, i.e. $\beta l << \pi/4$ so that the argument of the trigonometric functions $\tan()$ and $\sin()$ can be approximated by their arguments. This renders X positive and thus inductive, while it forces B to be negative and thus capacitive. If the electric length of the transmission line segment is shorter than $\pi/4$ there is only one parameter which can largely affect the reactance and susceptance in Equation B-3 and Equation B-4: the characteristic impedance of the line. For very high characteristic impedances Equation B-3 and Equation B-4 can be approximated by

$$X \simeq Z_0 \beta l \tag{B-5}$$
$$B \simeq 0, \tag{B-6}$$

while for very low characteristic impedances the opposite happens and Equation B-3 and Equation B-4 can be approximated by [43]

$$X \simeq 0 \tag{B-7}$$
$$B \simeq Y_0 \beta l. \tag{B-8}$$

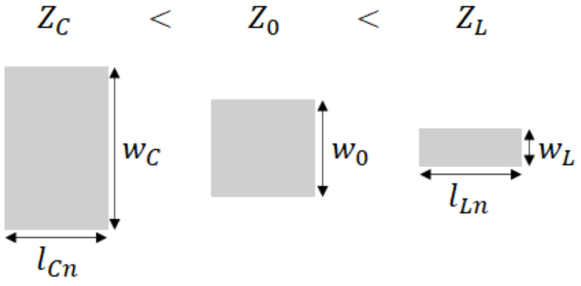

Figure B-2: Distributed elements approach lumped-elements as long as they are electrically small.

When using microstrip transmission lines with a certain dielectric material, and a fixed conductance, the width of the line is the only parameter which can be changed to vary the characteristic impedance. Looking at Figure B-2 this means that, for electrically short lines, a narrow transmission line section can be used to model an inductor and a wide section of transmission line can be used to model a capacitor. The larger the contrast between characteristic impedance of the inductive line section and the capacitive line section, the better the response the filter can have.

Appendix C

Simulations and tables for regular microstrip design

In this appendix extra simulation results and data from chapter 3 are shown. First tables giving the lengths of the Butterworth and Chebyshev filter sections corresponding to the simulations shown in subsection 3-2-2 are shown. These also include the lengths for the inverted microstrip simulations of chapter 4. During the simulations, the value of ε_{eff} used to calculate the electrical phase was retrieved from the Sonnet simulations for the lines at 350 GHz. Second, three plots showing the temporal current distribution over the design of the FP with filters attached are shown. These were also simulated in Sonnet at 350 GHz. In these simulations the signal is applied from port 1. From these simulations it is possible to see the coupling of the signal into the filter and to see how the attachment of the filter affects the standing wave pattern on the FP. It is important to keep in mind with these figures that the currents also have a temporal dependence which, in some cases, makes it look as it the filters are not attached at a voltage or current node but somewhere in between. The port numbers are the same as in Figure 3-15. The last figure gives the transmission of the FP with the filters attached with zero bias current on the left and 2 mA of bias current on the right for three different filter locations.

Table C-1: Filter section lengths in μm for filter requirements: $f_c = 175$ GHz, $f_s = 300$ GHz, ripple of 0.01 dB. Cells with an astrix indicate that the segment electrical phase is larger than $\pi/4$.

Microstrip	Regular		Inverted	
Function	Butterworth	Chebyshev	Butterworth	Chebyshev
L_1	3.5	10	5.0	14.5
C_2	7.25	12.5	3.75	6.25
L_3	16	22	23.5	32.25*
C_4	14.75	15	7.5	7.5
L_5	23.5	23.25	34.25*	34*
C_6	17.5	15	8.75	7.5
L_7	23.5	22	34.25*	32.25*
C_8	14.75	12.5	7.5	6.25
L_9	16	10	23.5	14.5
C_{10}	7.25		3.75	
L_{11}	3.5		5.0	
Total length	147.5	142.25	156.75	155

Table C-2: Filter section lengths in μm for filter requirements: $f_c = 150$ GHz, $f_s = 300$ GHz, ripple of 0.01 dB. Cells with an astrix indicate that the segment electrical phase is larger than $\pi/4$.

Microstrip	Regular		Inverted	
Function	Butterworth	Chebyshev	Butterworth	Chebyshev
L_1	5	11.5	7.25	16.75
C_2	10.25	14.25	5.25	7.25
L_3	22	25.5	32*	37.25*
C_4	19	17	9.5	8.75
L_5	28.5	26.5	42.75*	38.75*
C_6	19	16.5	9.5	8.25
L_7	22	22.25	32*	32.5*
C_8	10.25	9.5	5.25	3.75
L_9	5		7.25	
Total length	141	143	150.75	153.25

Table C-3: Filter section lengths in μm for filter requirements: $f_c = 100$ GHz, $f_s = 300$ GHz, ripple of 0.01 dB. Cells with an astrix indicate that the segment electrical phase is larger than $\pi/4$.

Microstrip	Regular		Inverted	
Function	Butterworth	Chebyshev	Butterworth	Chebyshev
L_1	11	16.75	16.25	24.5
C_2	21.5	20.75	11	10.5
L_3	41.5	36.25	60.5*	53*
C_4	29.5	23.5	15	11.75
L_5	30.25	32	44.25*	46.75*
C_6	8	10.75	4	5.5
Total length	141.75	140	151	152

Table C-4: Filter section lengths in μm for filter requirements: $f_c = 75$ GHz, $f_s = 150$ GHz, ripple of 0.01 dB. Cells with an astrix indicate that the segment electrical phase is larger than $\pi/4$.

Microstrip	Regular		Inverted	
Function	Butterworth	Chebyshev	Butterworth	Chebyshev
L_1	10	23	14.5	33.75
C_2	20.25	28.75	10.25	14.5
L_3	43.75	51	64*	74.5*
C_4	38.25	34.25	19.25	17.25
L_5	57.25	53	83.5*	77.25*
C_6	38.25	33	19.25	16.75
L_7	43.75	44.5	64*	65*
C_8	20.25	15	10.25	7.5
L_9	10		14.5	
Total length	279.75	282.5	299.5	306.5

Table C-5: Filter section lengths in μm for filter requirements: $f_c = 100$ GHz, $f_s = 200$ GHz, ripple of 0.01 dB. Cells with an astrix indicate that the segment electrical phase is larger than $\pi/4$.

Microstrip	Regular		Inverted	
Function	Butterworth	Chebyshev	Butterworth	Chebyshev
L_1	7.5	17.25	10.75	25.25
C_2	15.25	21.5	7.75	11
L_3	32.75	38.25	48*	55.75*
C_4	28.75	25.75	14.5	13
L_5	42.75	39.75	62.5*	58*
C_6	28.75	24.75	14.5	12.5
L_7	32.75	33.25	48*	48.75*
C_8	15.25	11.25	14.5	5.75
L_9	7.5		10.75	
Total length	211.25	211.75	231.25	230

Table C-6: Filter section lengths in μm for filter requirements: $f_c = 175$ GHz, $f_s = 350$ GHz, ripple of 0.01 dB. Cells with an astrix indicate that the segment electrical phase is larger than $\pi/4$.

Microstrip	Regular		Inverted	
Function	Butterworth	Chebyshev	Butterworth	Chebyshev
L_1	4.25	10	6.25	14.5
C_2	8.75	12.25	4.5	6.25
L_3	18.75	21.75	27.5*	32*
C_4	16.5	14.75	8.25	7.5
L_5	24.5	22.75	35.75*	33.25*
C_6	16.5	14	8.25	7.25
L_7	18.75	19	27.5*	27.75*
C_8	8.75	6.5	4.5	3.25
L_9	4.25		6.25	
Total length	121	121	128.75	131.75

Table C-7: Filter section lengths in μm for filter requirements: $f_c = 175$ GHz, $f_s = 300$ GHz, ripple of 0.1 dB. Cells with an astrix indicate that the segment electrical phase is larger than $\pi/4$.

Microstrip	Regular Chebyshev	Inverted Chebyshev
L_1	14.5	21.25
C_2	12.5	6.25
L_3	26	38*
C_4	14	7
L_5	26.5	38.75*
C_6	13.75	7
L_7	23.75	34.75*
C_8	7.75	3.75
Total length	138.75	156.75

Table C-8: Filter section lengths in μm for filter requirements: $f_c = 175$ GHz, $f_s = 300$ GHz, ripple of 1 dB. Cells with an astrix indicate that the segment electrical phase is larger than $\pi/4$.

Microstrip	Regular Chebyshev	Inverted Chebyshev
L_1	26.5	38.75
C_2	9.75	5
L_3	38	55.25*
C_4	10.25	5.25
L_5	38	55.25*
C_6	9.75	5
L_7	26.5	38.75*
Total length	158.75	203.25

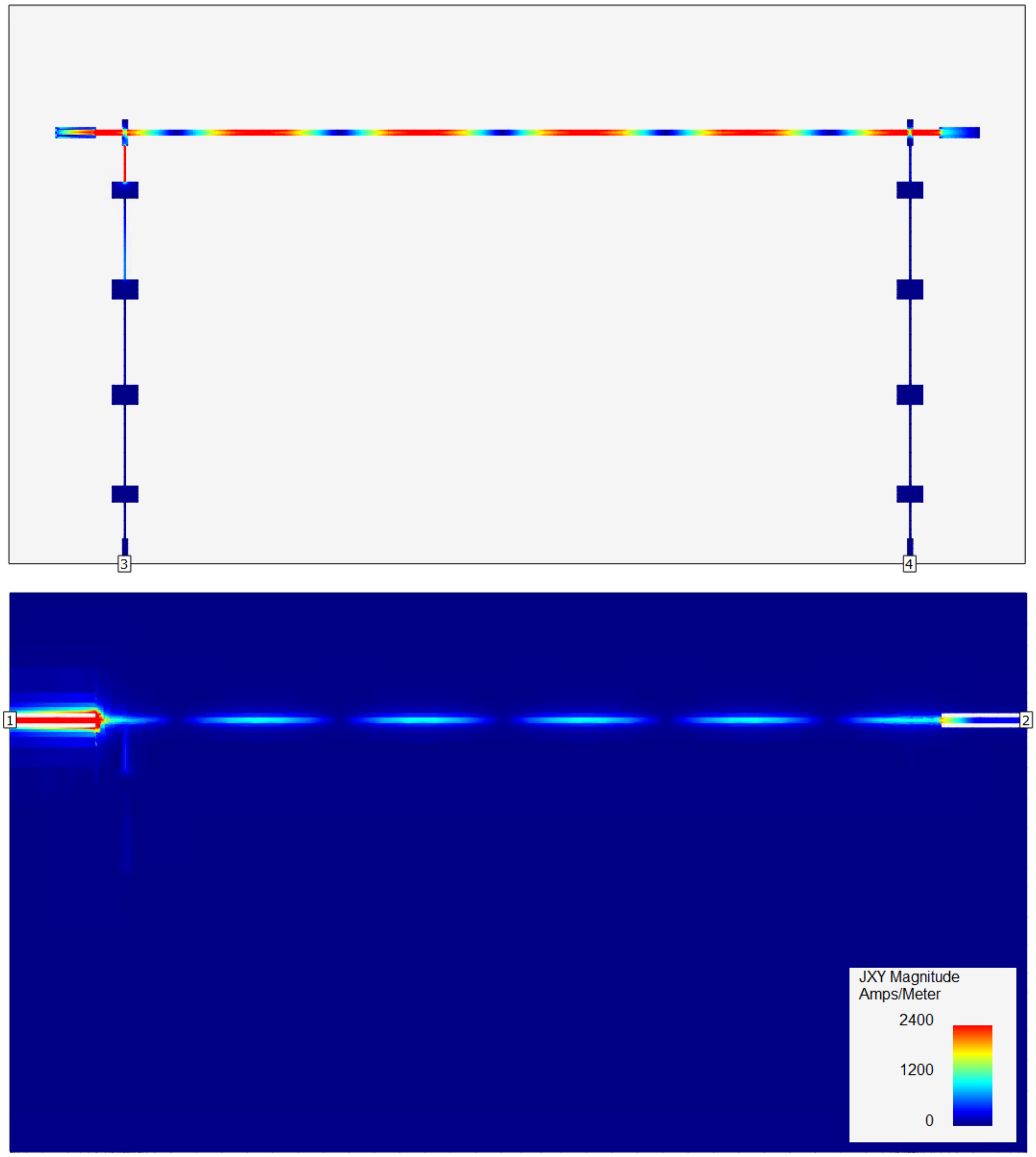

Figure C-1: Current distribution on FP and filters for $n = 6$ and filters at first voltage node, corresponding to Figure 3-16a.

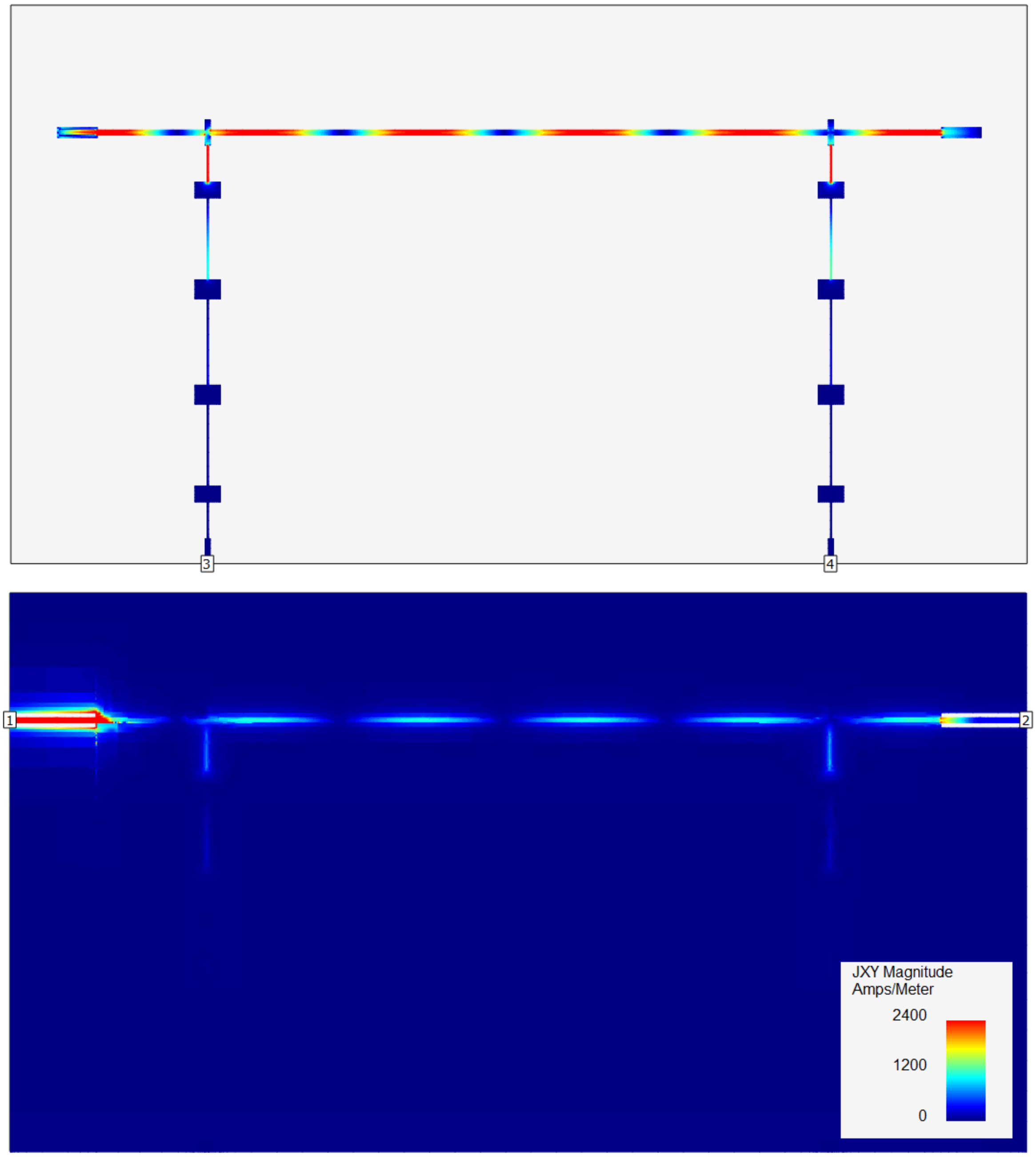

Figure C-2: Current distribution on FP and filters for $n = 6$ and filters at first current node, corresponding to Figure 3-16b.

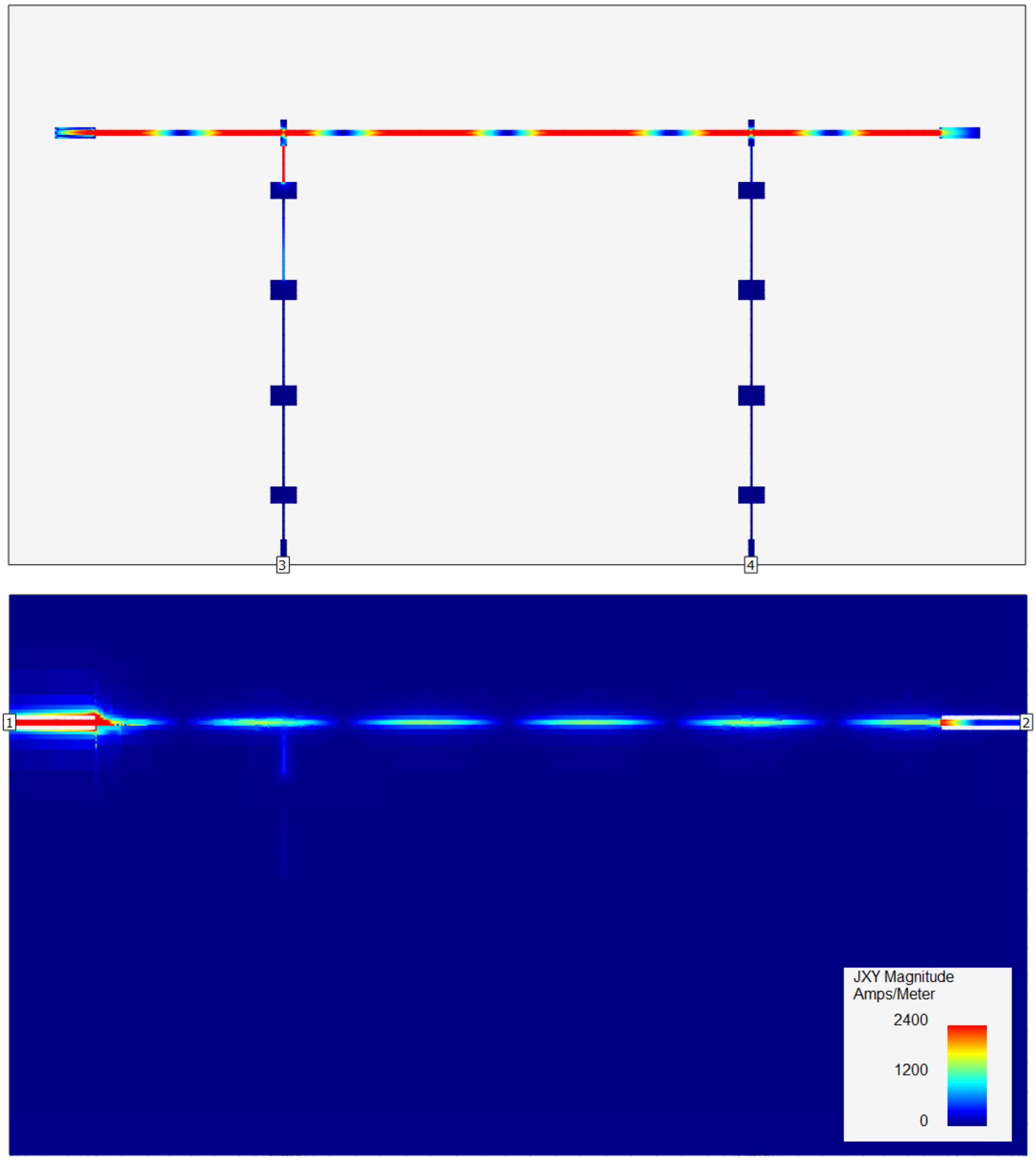

Figure C-3: Current distribution on FP and filters for $n = 6$ and filters at second voltage node, corresponding to Figure 3-16c.

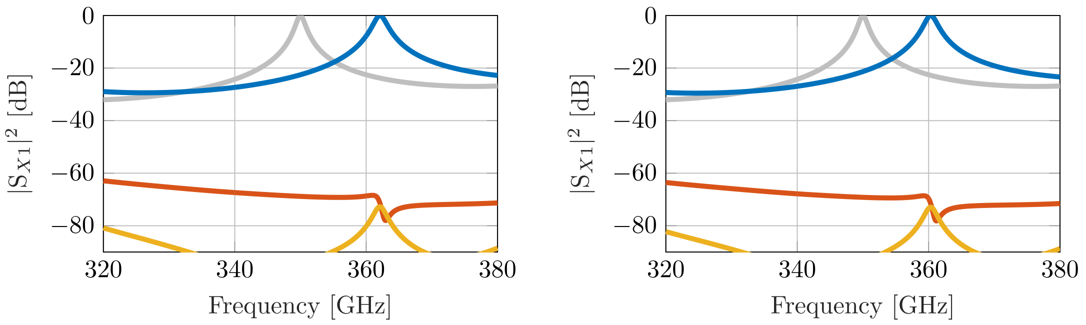

(a) First voltage node.

(b) First voltage node biased at 2 mA.

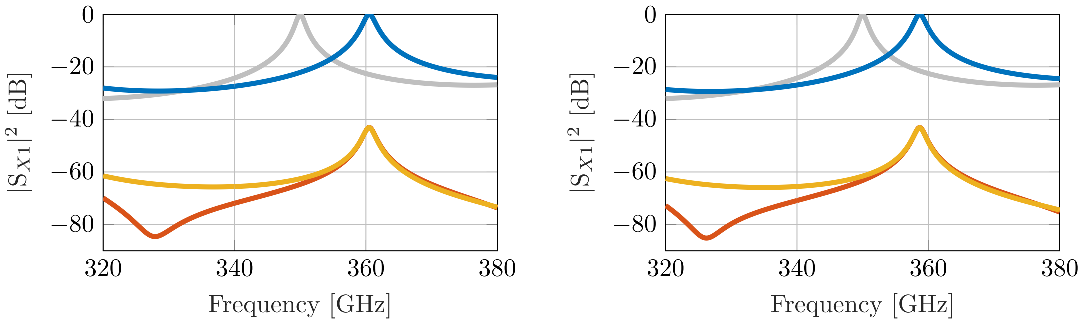

(c) First current node.

(d) First current node biased at 2 mA.

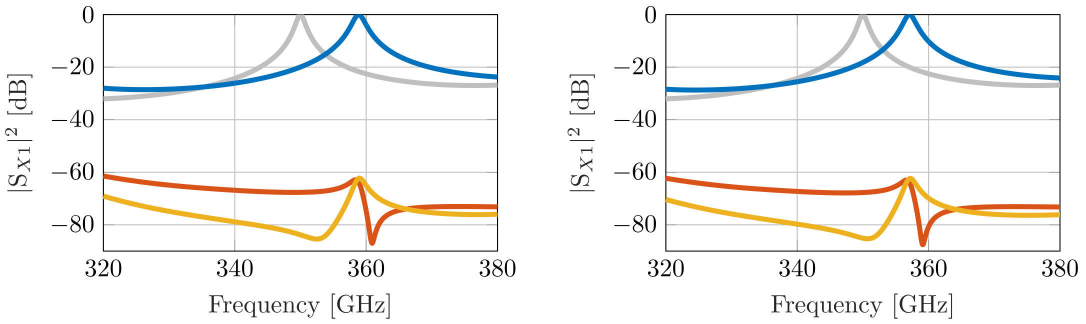

(e) Second voltage node.

(f) Second voltage node biased at 2 mA.

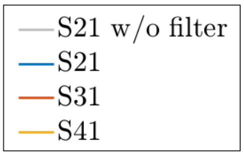

(g) Legend

Figure C-4: The effect of the filter (no bias current) on the transmission of the FP. The grey line in each plot is the S21 for the FP without the filters attached.

Appendix D

Simulations and tables for inverted microstrip design

In this appendix the simulations performed for the inverted microstrip design of chapter 4, which are not treated in the text, are shown. This allows for further comparison between the two designs. First the simulation of the coupler length is shown. After this, the effect of varying f_c and f_s on both the Butterworth and the Chebyshev filters, the effect of the ripple on the Chebyshev filter and the effect of unmatched terminations on the Chebyshev filter are given. The simulation of the current distribution to optimize the location of the attachment of the filter to the FP is shown with the according positions given in the table below. The three plots show the temporal current distribution over the design of the FP with filters attached. These were also simulated in Sonnet at 350 GHz. In these simulations the signal is applied from port 1. From these simulations it is possible to see the coupling of the signal into the filter and to see how the attachment of the filter affects the standing wave pattern on the FP. The port numbers are the same as in Figure 4-2. It is important to keep in mind with these figures that the currents also have a temporal dependence which, in some cases, makes it look as it the filters are not attached at a voltage or current node but somewhere in between. The last figure gives the transmission of the FP with the filters attached with zero bias current on the left and 2 mA of bias current on the right for three different filter locations. The nonlinearity of the change in resonance with respect to a linear change in current in shown after this. The values of the bias current and their corresponding change in L_s for each line are given in Table D-2. Finally, the effect of the 2 mA bias current on the filter is shown.

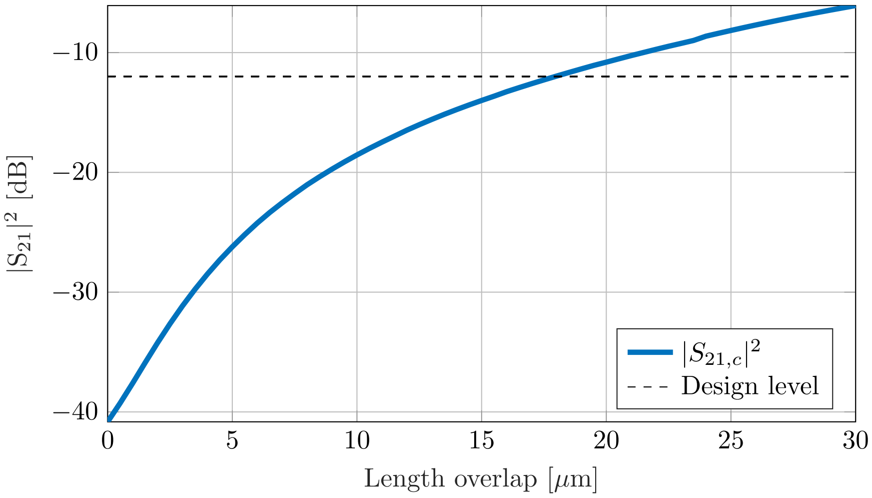

Figure D-1: Simulated coupler overlap length l_{over} versus transmission for inverted microstrip.

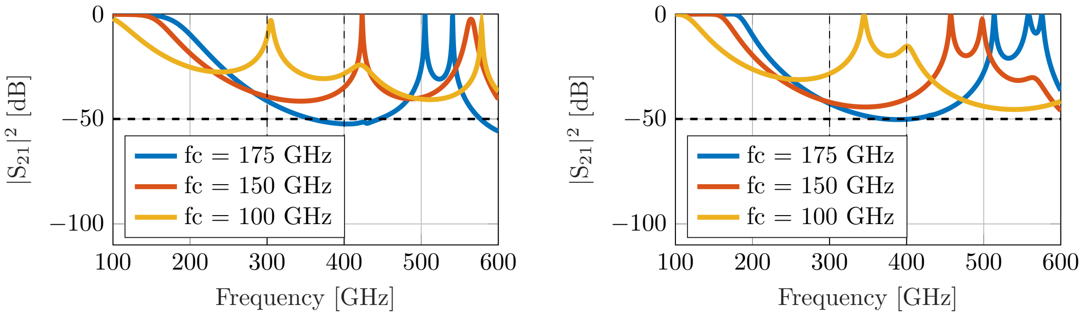

(a) Butterworth **(b)** Chebyshev

Figure D-2: Sonnet simulations Butterworth and Chebyshev filters with $f_s = 300$ GHz, $A_s = 50$ dB and a ripple of 0.01 dB for different f_c.

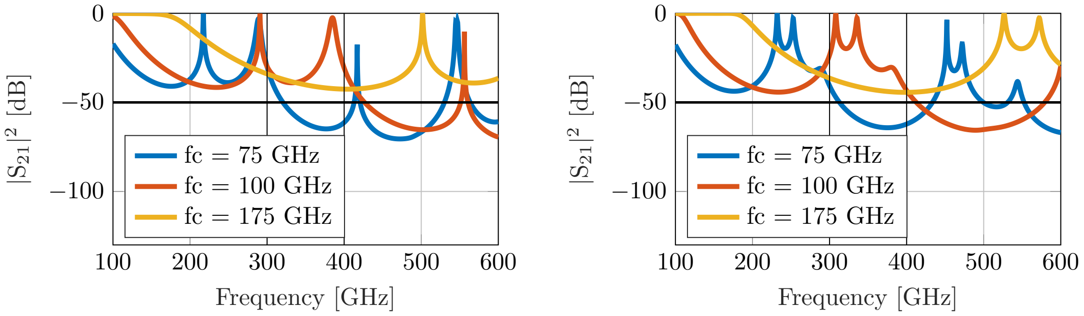

(a) Butterworth **(b)** Chebyshev

Figure D-3: Sonnet simulations Butterworth and Chebyshev filters with $f_c = f_s/2$ GHz, $A_s = 50$ dB and a ripple of 0.01 dB.

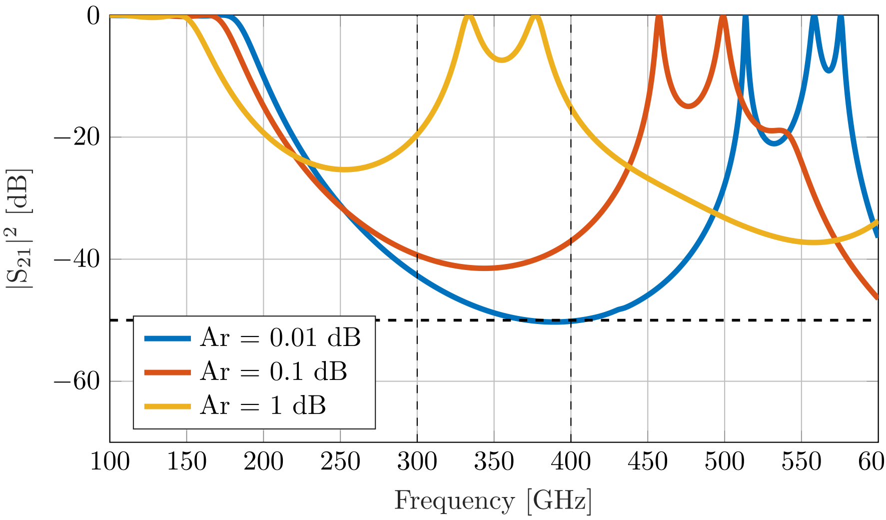

Figure D-4: Effect of ripple on Chebyshev filter transmission. In this case, $f_c = 175$ GHz, $f_s = 300$ GHz and $A_s = 50$ dB.

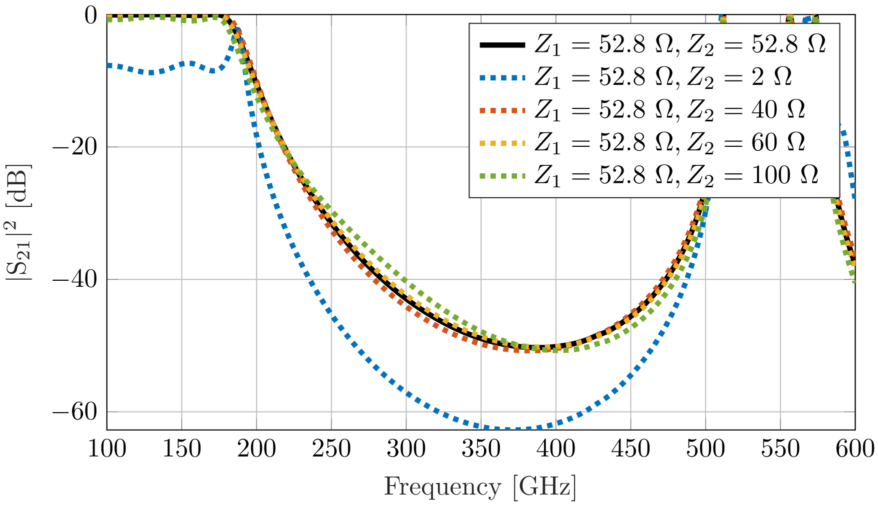

Figure D-5: Effect of changing the load at one side of the filter. The black line represents the filter transfer for the ideal terminations (52.8Ω).

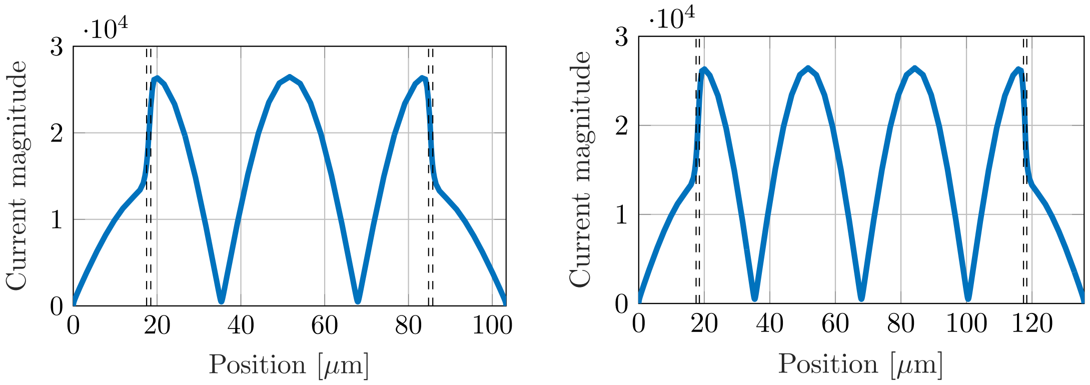

(a) $N = 3$ **(b)** $N = 4$

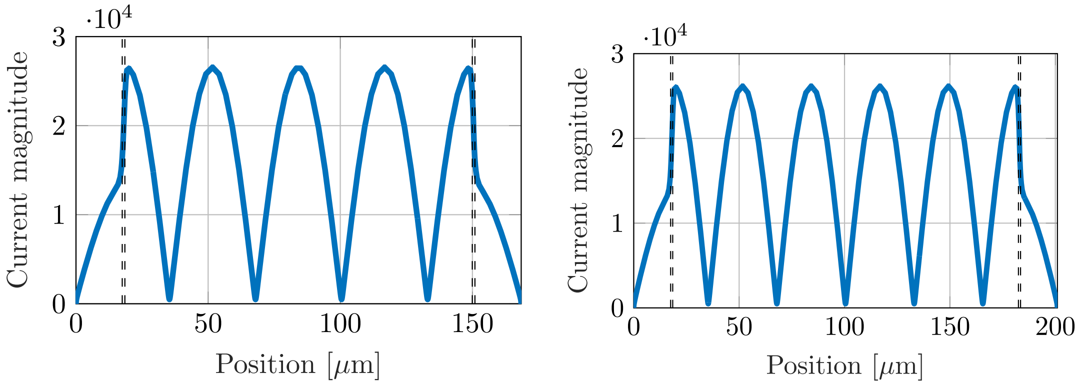

(c) $N = 5$ **(d)** $N = 6$

Figure D-6: Simulation of current distribution on FP for different amount of modes for an inverted microstrip and a thinner FP. This simulation is used to determine the optimal locations for the filters.

Table D-1: Locations of current maxima and minima for the inverse microstrip, measured from the inner side of the coupler. These correspond to the current distribution simulations of Figure D-6

Maxima							
Mode	Length [μm]	Max 1	Max 2	Max 3	Max 4	Max 5	Max 6
2	33.75	1.57	32.18				
3	66.3	1.57	33.15	64.73			
4	98.9	1.57	33.17	65.73	97.33		
5	131.45	1.55	33.15	66.7	98.25	129.86	
6	164	1.57	33.17	65.68	98.32	130.83	162.43
Minima							
Mode	Length [μm]	Min 1	Min 2	Min 3	Min 4	Min 5	
2	33.75	16.88					
3	66.3	16.86	49.44				
4	98.9	16.88	49.45	82.02			
5	131.45	16.85	49.42	81.98	114.55		
6	164	16.86	49.44	82.0	114.57	147.14	

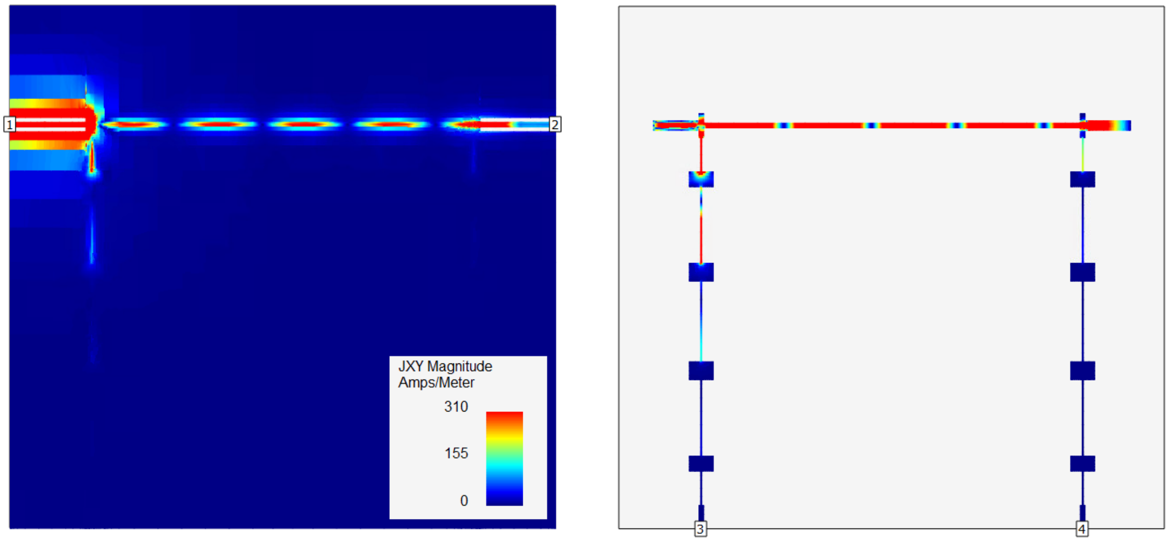

Figure D-7: Current distribution on FP and filters for $n = 6$ and filters at first voltage node, corresponding to Figure 4-3a.

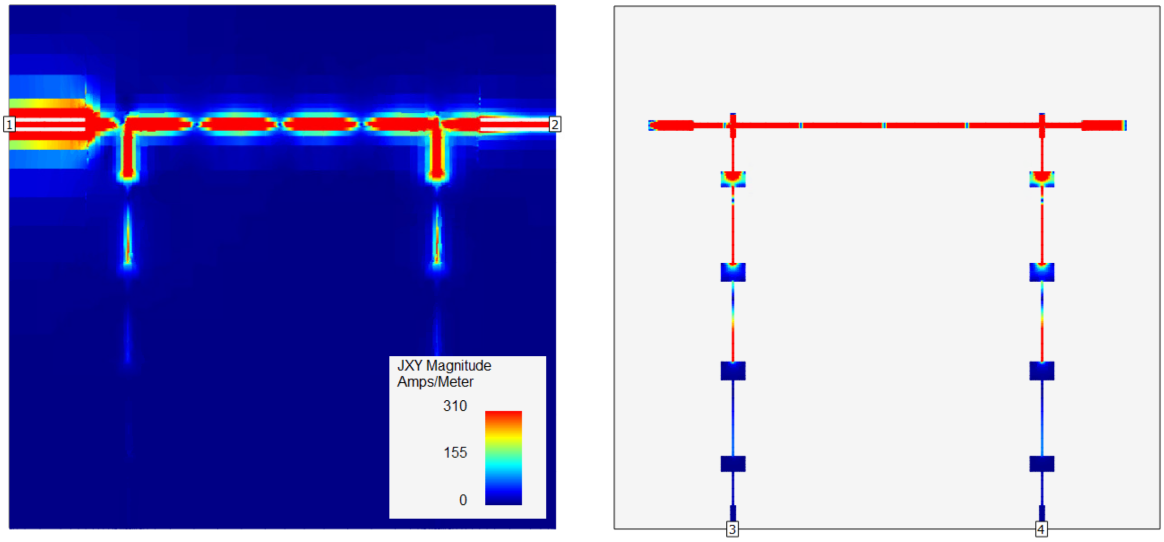

Figure D-8: Current distribution on FP and filters for $n = 6$ and filters at first current node, corresponding to Figure 4-3b.

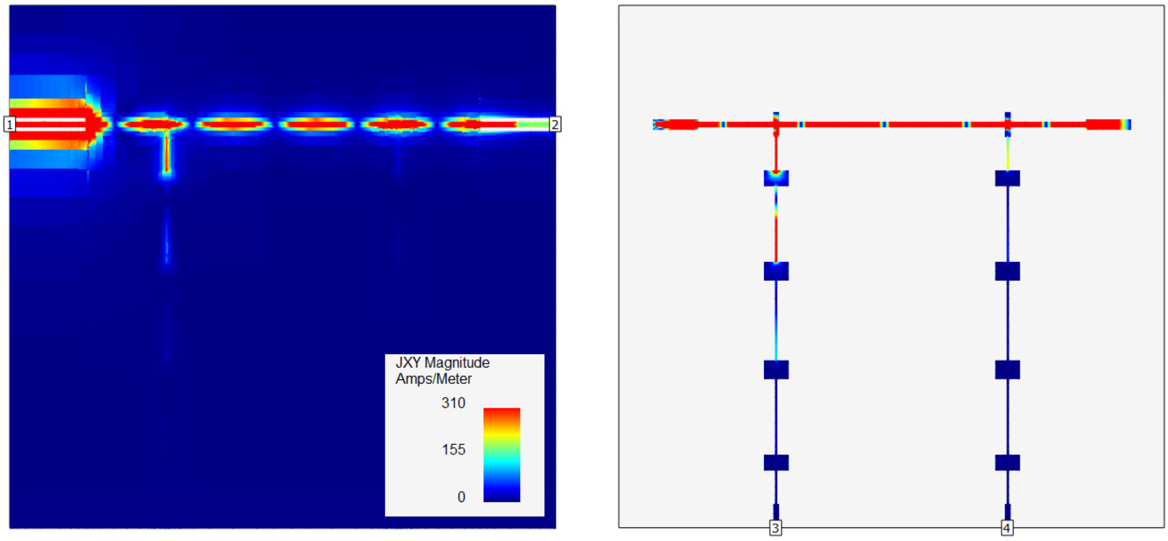

Figure D-9: Current distribution on FP and filters for $n = 6$ and filters at second voltage node, corresponding to Figure 4-3c.

Table D-2: Values of bias current and according values of sheet kinetic inductance for the filter and FP. This change is plotted in Figure D-10 to visualize effect of the biasing on the transmission of the FP with $n = 6$ at 350 GHz.

Bias current [mA]	$L_{s,FP}$ [pH/sq]	$L_{s,LPF}$ [pH/sq]
0	4.0680	1.0090
0.2	4.0687	1.0092
0.4	4.0709	1.0096
0.6	4.0744	1.0105
0.8	4.0794	1.0116
1.0	4.0859	1.0131
1.2	4.0937	1.0148
1.4	4.1030	1.0170
1.6	4.1138	1.0194
1.8	4.1259	1.0221
2.0	4.1395	1.0252

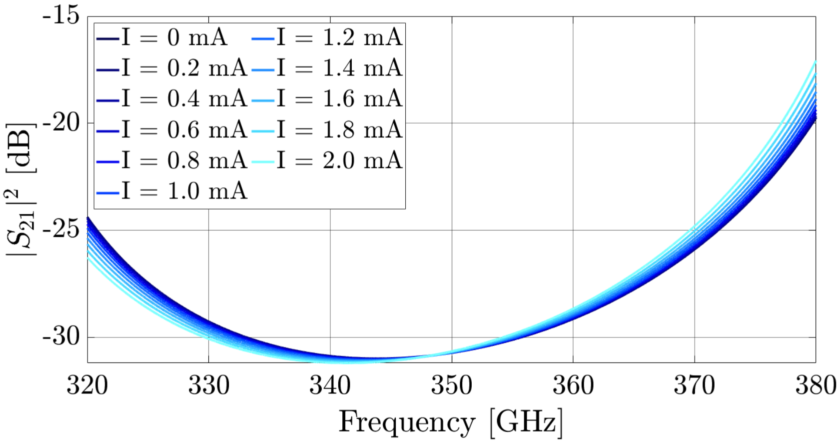

(a) 1st voltage node

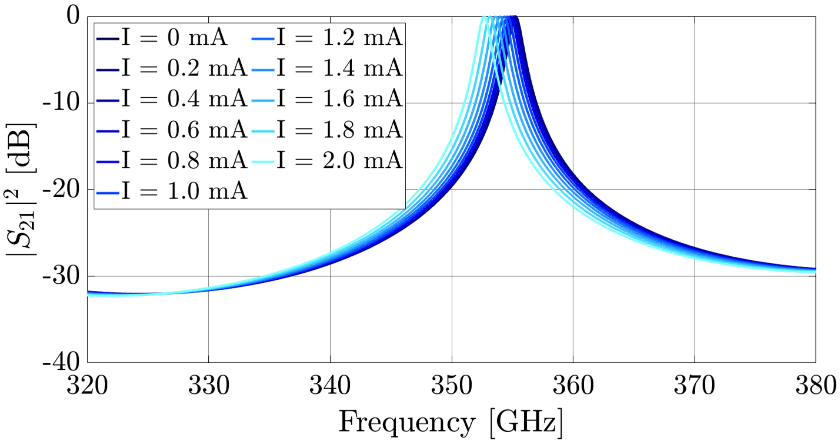

(b) 1st current node

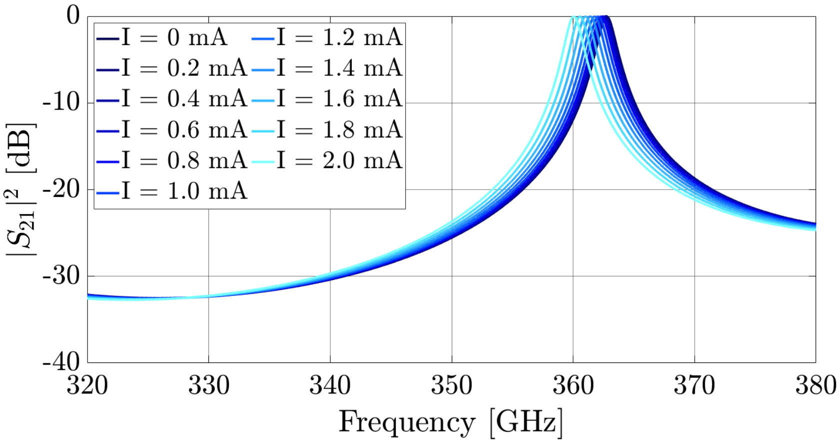

(c) 2nd voltage node

Figure D-10: The effect of a linear change in current on the resonance shift for the filter attached at different locations on the FP. The current and according values of L_s are given in Table D-2.

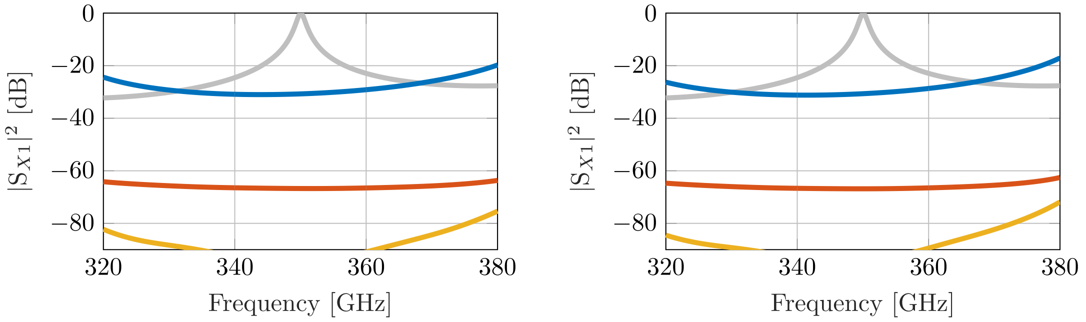

(a) First voltage node. **(b)** First voltage node biased at 2 mA.

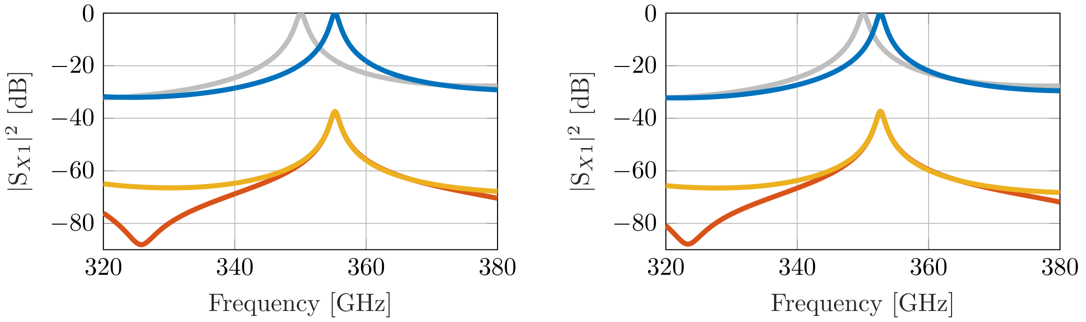

(c) First current node. **(d)** First current node biased at 2 mA.

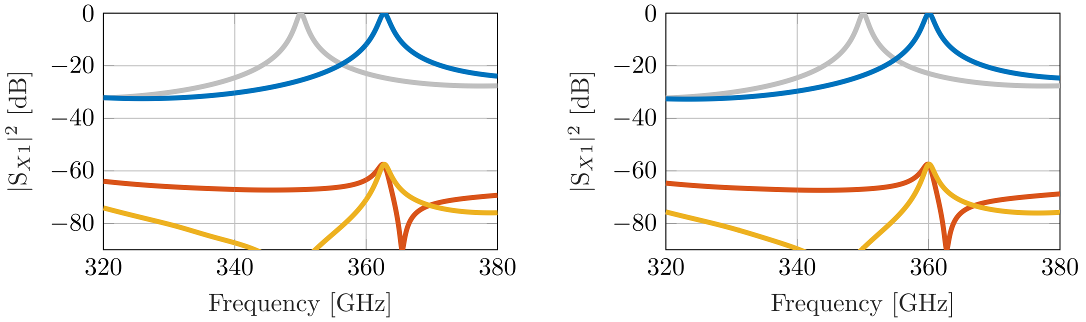

(e) Second voltage node. **(f)** Second voltage node biased at 2 mA.

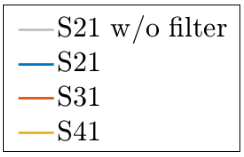

(g) Legend

Figure D-11: The effect of the filter (no bias current) on the transmission of the FP. The grey line in each plot is the S21 for the FP without the filters attached. $S21$ is the transmission of the resonator, $S31$ the transmission between one coupler and the filter nearest to it and $S41$ is the transmission between one coupler and the filter furthest from it.

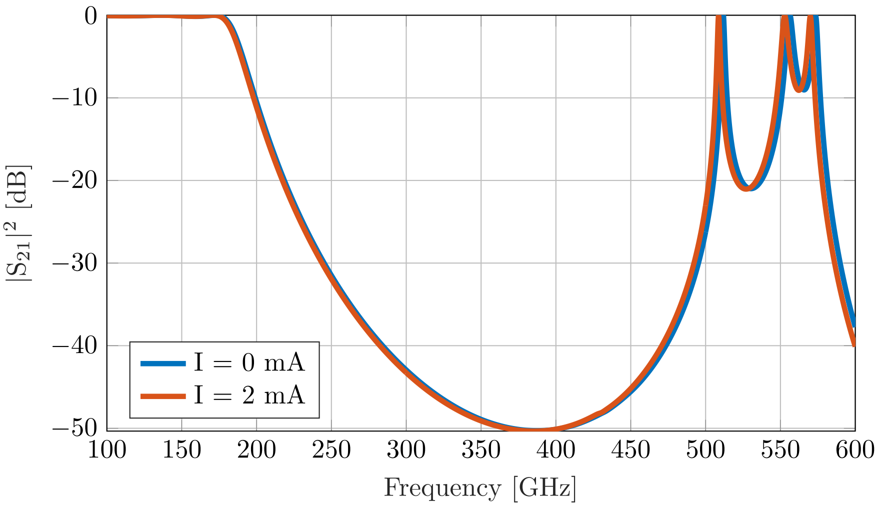

Figure D-12: Effect of bias current on filter. The level of current for the biased filter is 2 mA.

Appendix E

Fabrication details

In this appendix images of the fabrication process are shown to clarify the design discussed in chapter 4.

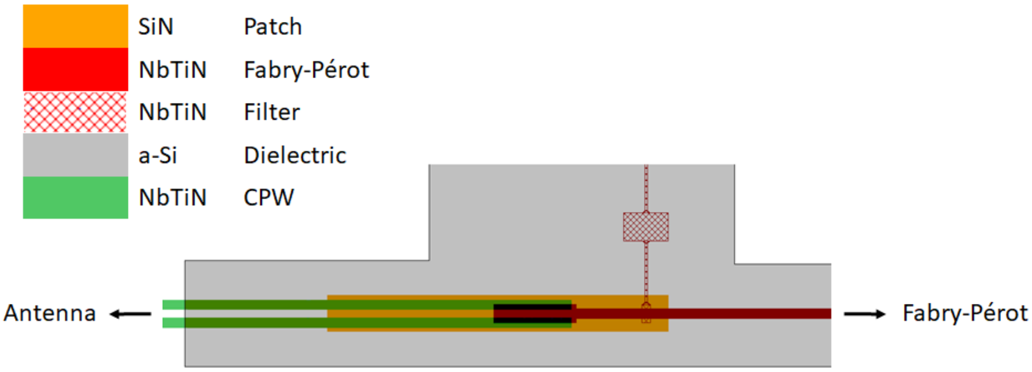

Figure E-1: Schematic of FP coupler with large a-Si patch to avoid trenching.

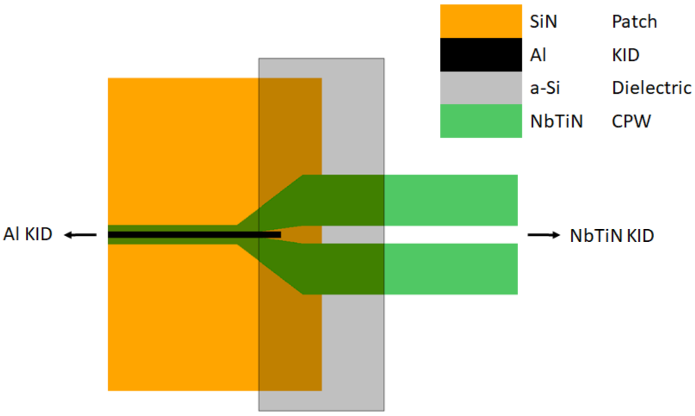

Figure E-2: Schematic of KID Al-NbTiN transition with large a-Si patch to avoid trenching.

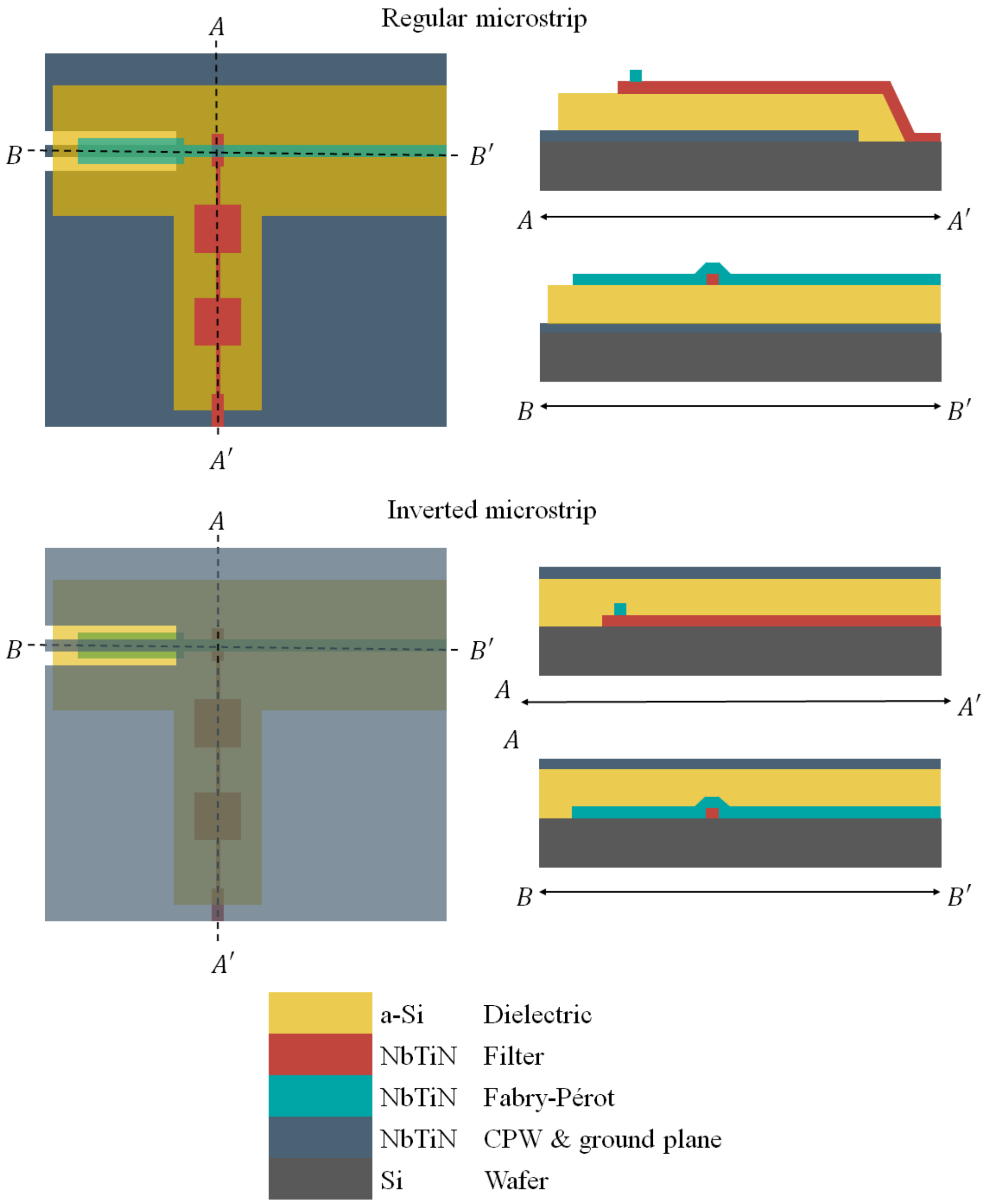

Figure E-3: Layout of regular versus inverted microstrip architecture.

Bibliography

[1] A. Endo, "Lecture 1b: Thz astronomical science," 4 2019.

[2] A. W. Blain, I. Smail, R. Ivison, J. Kneib, and D. T. Frayer, "Submillimeter galaxies," *Physics Reports*, vol. 369, no. 2, pp. 111–176, 2002.

[3] H. Dole, G. Lagache, J. Puget, K. I. Caputi, N. Fernández-Conde, E. Le Floc'h, C. Papovich, P. G. Pérez-González, G. H. Rieke, and M. Blaylock, "The cosmic infrared background resolved by spitzer - contributions of mid-infrared galaxies to the far-infrared background," *A&A*, vol. 451, no. 2, pp. 417–429, 2006.

[4] P. K. Day, H. G. LeDuc, B. A. Mazin, A. Vayonakis, and J. Zmuidzinas, "A broadband superconducting detector suitable for use in large arrays," *Nature*, vol. 425, 2003.

[5] A. Endo, K. Karatsu, A. P. Laguna, B. Mirzaei, R. Huiting, D. Thoen, V. Murugesan, S. J. C. Yates, J. Bueno, N. V. Marrewijk, S. Bosman, O. Yurduseven, N. Llombart, J. Suzuki, M. Naruse, P. J. de Visser, P. P. van der Werf, T. M. Klapwijk, and J. J. A. Baselmans, "Wideband on-chip terahertz spectrometer based on a superconducting filterbank," *Journal of Astronomical Telescopes, Instruments, and Systems*, vol. 5, no. 3, pp. 1 – 12, 2019.

[6] J. Redford, J. Wheeler, K. Karkare, S. Hailey-Dunsheath, C. M. Bradford, E. Shirokoff, P. S. Barry, G. Che, J. Glenn, H. G. Leduc, P. Mauskopf, R. McGeehan, T. Reck, and J. Zmuidzinas, "The design and characterization of a 300 channel, optimized full-band millimeter filterbank for science with SuperSpec," in *Millimeter, Submillimeter, and Far-Infrared Detectors and Instrumentation for Astronomy IX* (J. Zmuidzinas and J.-R. Gao, eds.), vol. 10708, pp. 187 – 194, International Society for Optics and Photonics, SPIE, 2018.

[7] C. N. Thomas, R. Blundell, D. Glowacka, D. J. Goldie, P. Grimes, E. de Lera Acedo, S. Paine, S. Withington, and L. Zeng, "Progress on the cambridge emission line surveyor (camels)," *26th International Symposium on Space Terahertz Technology*, 3 2015.

[8] G. Cataldo, W. T. Hsieh, W.-C. Huang, S. Harvey Moseley, T. R. Stevenson, and E. J. Wollack, “Micro-spec: an ultracompact, high-sensitivity spectrometer for far-infrared and submillimeter astronomy,” *Applied Optics*, vol. 53, 2 2014.

[9] A. Pascual Laguna, D. Cavallo, J. J. A. Baselmans, and N. Llombart, “Focused connected array as a wideband beam-steering feed for quasi-optical systems,” *In 15th European Conference on Antennas and Propagation (EuCAP)*, 3 2021.

[10] K. Kouwenhoven, “Dielectric loss measurements at sub-k temperatures and terahertz frequencies,” 2019.

[11] B. H. Eom, P. K. Day, H. G. LeDuc, and J. Zmuidzinas, “A wideband, low-noise superconducting amplifier with high dynamic range,” *Nature Physics*, vol. 8, 8 2012.

[12] S. Shu, N. Klimovich, B. Eom, A. Beyer, R. Basu Thakur, H. Leduc, and P. Day, “Nonlinearity and wideband parametric amplification in an nbtin microstrip transmission line,” 2021.

[13] R. Basu Thakur, N. Klimovich, P. K. Day, E. Shirokoff, P. D. Mauskopf, F. Faramarzi, and P. S. Barry, “Superconducting on-chip fourier transform spectrometer,” *Journal of Low Temperature Physics*, vol. 200, 9 2020.

[14] A. A. Adamyan, S. E. Kubatkin, and A. V. Danilov, “Tunable superconducting microstrip resonators,” *Applied Physics Letters*, vol. 108, 4 2016.

[15] F. Chen, A. J. Sirois, R. W. Simmonds, and A. J. Rimberg, “Introduction of a dc bias into a high- q superconducting microwave cavity,” *Applied Physics Letters*, vol. 98, 3 2011.

[16] S. X. Li and J. B. Kycia, “Applying a direct current bias to superconducting microwave resonators by using superconducting quarter wavelength band stop filters,” *Applied Physics Letters*, vol. 102, 6 2013.

[17] M. R. Vissers, J. Hubmayr, M. Sandberg, S. Chaudhuri, C. Bockstiegel, and J. Gao, “Frequency-tunable superconducting resonators via nonlinear kinetic inductance,” *Applied Physics Letters*, vol. 107, 8 2015.

[18] S. Zhao, S. Withington, D. J. Goldie, and C. N. Thomas, “Suppressed-gap millimetre wave kinetic inductance detectors using DC-bias current,” *Journal of Physics D: Applied Physics*, vol. 53, p. 345301, 6 2020.

[19] J. E. Healey, T. Lindström, M. S. Colclough, C. M. Muirhead, and A. Y. Tzalenchuk, “Magnetic field tuning of coplanar waveguide resonators,” *Applied Physics Letters*, vol. 93, 2008.

[20] S. E. D. Graaf, A. V. Danilov, A. Adamyan, T. Bauch, and S. E. Kubatkin, “Magnetic field resilient superconducting fractal resonators for coupling to free spins,” *Journal of Applied Physics*, vol. 112, 2012.

[21] M. Xu, X. Han, W. Fu, C. L. Zou, M. H. Devoret, and H. X. Tang, “Frequency-tunable high- q superconducting resonators via wireless control of nonlinear kinetic inductance,” *Applied Physics Letters*, vol. 114, 5 2019.

[22] J. W. Rohlf, *Modern Physics from α to Z^0*. John Wiley, 1 ed., 1994.

[23] L. N. Cooper, “Bound electron pairs in a degenerate fermi gas,” *Phys. Rev.*, vol. 104, pp. 1189–1190, 11 1956.

[24] J. Bardeen, L. N. Cooper, and J. R. Schrieffer, “Theory of superconductivity,” *Phys. Rev.*, vol. 108, pp. 1175–1204, 12 1957.

[25] P. J. D. Visser, “Quasiparticle dynamics in aluminium superconducting microwave resonators.”

[26] R. Barends, “Photon-detecting superconducting resonators.”

[27] A. B. Pippard and W. L. Bragg, “Field variation of the superconducting penetration depth,” *Proceedings of the Royal Society of London. Series A. Mathematical and Physical Sciences*, vol. 203, no. 1073, pp. 210–223, 1950.

[28] F. London, H. London, and F. A. Lindemann, “The electromagnetic equations of the supraconductor,” *Proceedings of the Royal Society of London. Series A - Mathematical and Physical Sciences*, vol. 149, no. 866, pp. 71–88, 1935.

[29] M. Tinkham, *Introduction to Superconductivity.* Dover Publications, 2004.

[30] J. Pearl, “Current distribution in superconducting films carrying quantized fluxoids,” *Applied Physics Letters*, vol. 5, no. 4, pp. 65–66, 1964.

[31] D. C. Mattis and J. Bardeen, “Theory of the anomalous skin effect in normal and superconducting metals,” *Phys. Rev.*, vol. 111, pp. 412–417, 7 1958.

[32] R. L. Kautz, “Picosecond pulses on superconducting striplines,” *Journal of Applied Physics*, vol. 49, no. 1, pp. 308–314, 1978.

[33] A. A. Abrikosov, “The magnetic properties of superconducting alloys,” *Journal of Physics and Chemistry of Solids*, vol. 2, no. 3, pp. 199–208, 1957.

[34] N. B. Kopnin, “Theory of superconductivity,” 12 2006.

[35] J. Bardeen and M. J. Stephen, “Theory of the motion of vortices in superconductors,” *Phys. Rev.*, vol. 140, pp. A1197–A1207, 11 1965.

[36] J. Zmuidzinas, “Superconducting microresonators: Physics and applications,” *Annual Review of Condensed Matter Physics*, vol. 3, pp. 169–214, 2012.

[37] A. Anthore, H. Pothier, and D. Esteve, “Density of states in a superconductor carrying a supercurrent,” *Phys. Rev. Lett.*, vol. 90, p. 127001, 3 2003.

[38] J. Romijn, T. M. Klapwijk, M. J. Renne, and J. E. Mooij, “Critical pair-breaking current in superconducting aluminum strips far below T_c,” *Phys. Rev. B*, vol. 26, pp. 3648–3655, 10 1982.

[39] K. K. Likharev, “The formation of a mixed state in planar semiconductor films,” *Radiophysics and Quantum Electronics*, vol. 14, no. 6, 1971.

[40] K. D. Usadel, "Generalized diffusion equation for superconducting alloys," *Phys. Rev. Lett.*, vol. 25, pp. 507–509, 8 1970.

[41] R. J. Collier, *Transmission Lines : Equivalent Circuits, Electromagnetic Theory, and Photons.* Cambridge University Press, 2012.

[42] B. Buijtendorp, "Microstrip filling fraction calculation," 10 2020.

[43] D. Pozar, *Microwave Engineering.* John Wiley, 4 ed., 2012.

[44] R. M. J. Janssen, J. J. A. Baselmans, A. Endo, L. Ferrari, S. J. C. Yates, A. M. Baryshev, and T. M. Klapwijk, "High optical efficiency and photon noise limited sensitivity of microwave kinetic inductance detectors using phase readout," *Applied Physics Letters*, vol. 103, no. 20, p. 203503, 2013.

[45] J. Gao, J. Zmuidzinas, P. Vayonakis, A. ans Day, B. Mazin, and H. Leduc, "Equivalence of the effects on the complex conductivity of superconductor due to temperature change and external pair breaking," *Journal of Low Temperature Physics*, vol. 151, 2008.

[46] J. J. Baselmans, "Direct detectors."

[47] D. Thoen, V. Murugesan, K. Karatsu, A. P. Laguna, A. Endo, and J. J. A. Baselmans, "Combining uv-and electron-beam lithography for superconducting bandpass filters in mm/sub-mm astronomy," in *Millimeter, Submillimeter, and Far-Infrared Detectors and Instrumentation for Astronomy X* (J. Zmuidzinas and J.-R. Gao, eds.), vol. 11453, International Society for Optics and Photonics, SPIE, 2020.

[48] I. C. Hunter, *Theory and design of microwave filters.* No. number in Electromagnetic waves series, Institution of Electrical Engineers, 2001.

[49] J. Rhodes, *Theory of Electrical Filters.* John Wiley & Sons, 1976.

[50] J. S. Hong, *Microstrip filters for RF/microwave applications.* Wiley, 2 ed., 2011.

[51] S. Hähnle, N. v. Marrewijk, A. Endo, K. Karatsu, D. J. Thoen, V. Murugesan, and J. J. A. Baselmans, "Suppression of radiation loss in high kinetic inductance superconducting co-planar waveguides," *Applied Physics Letters*, vol. 116, no. 18, p. 182601, 2020.

[52] S. Hähnle, K. Kouwenhoven, B. T. Buijtendorp, A. Endo, K. Karatsu, D. J. Thoen, V. Murugesan, and J. J. A. Baselmans, "Superconducting microstrip losses at microwave and sub-mm wavelengths." Submitted to *Phys. Rev. Appl.*

[53] S. Jenei, B. K. J. C. Nauwelaers, and S. Decoutere, "Physics-based closed-form inductance expression for compact modeling of integrated spiral inductors," *IEEE Journal of Solid-State Circuits*, vol. 37, no. 1, pp. 77–80, 2002.

[54] K. K. Center, "Microstrip rectangular inductor (strip bridge, 3-layer substrate)."

[55] S. J. C. Yates, A. M. Baryshev, O. Yurduseven, J. Bueno, K. K. Davis, L. Ferrari, W. Jellema, N. Llombart, V. Murugesan, D. J. Thoen, and J. J. A. Baselmans, "Surface wave control for large arrays of microwave kinetic inductance detectors," *IEEE Transactions on Terahertz Science and Technology*, vol. 7, no. 6, pp. 789–799, 2017.

[56] L. Ferrari, O. Yurduseven, N. Llombart, S. J. C. Yates, J. Bueno, V. Murugesan, D. J. Thoen, A. Endo, A. M. Baryshev, and J. J. A. Baselmans, “Antenna coupled mkid performance verification at 850 ghz for large format astrophysics arrays,” *IEEE Transactions on Terahertz Science and Technology*, vol. 8, no. 1, pp. 127–139, 2018.

[57] D. J. Thoen, B. G. C. Bos, E. A. F. Haalebos, T. M. Klapwijk, J. J. A. Baselmans, and A. Endo, “Superconducting nbtin thin films with highly uniform properties over a ∅ 100 mm wafer,” *IEEE Transactions on Applied Superconductivity*, vol. 27, no. 4, pp. 1–5, 2017.

[58] D. J. Thoen and J. J. A. Baselmands. private communication, 3 2021.

[59] J. R. Clem and K. K. Berggren, “Geometry-dependent critical currents in superconducting nanocircuits,” *Phys. Rev. B*, vol. 84, p. 174510, 11 2011.

[60] H. L. Hortensius, E. F. C. Driessen, T. M. Klapwijk, K. K. Berggren, and J. R. Clem, “Critical-current reduction in thin superconducting wires due to current crowding,” *Applied Physics Letters*, vol. 100, no. 18, p. 182602, 2012.

[61] D. J. Thoen, “Deshima 2.0 lt180 fab review,” 1 2020.

[62] K. Karatsu, “Lt207 elbow sparse chip (chip 7) measurement,” 1 2021.

[63] K. Karatsu, “Lt207 elbow dense chip (chip 5) measurement,” 1 2021.

[64] A. D. Poularikas, *Handbook of formulas and tables for signal processing.* CRC Press, 1 ed., 1999.